UNDERSTANDING SURFACE HOPPING ALGORITHMS AND THEIR APPLICATIONS IN CONDENSED PHASE SYSTEMS

Wenjun Ouyang

A DISSERTATION

in

Chemistry

Presented to the Faculties of the University of Pennsylvania

in

Partial Fullfillment of the Requirements for the

Degree of Doctor of Philosophy

2017

Supervisor of Dissertation

_____

Dr. Joseph E. Subotnik

Professor of Chemistry

Graduate Group Chairperson

_____

Dr. Gary A. Molander

Hirschmann-Makineni Professor of Chemistry

Dissertation Committee

Dr. Andrew M. Rappe, Blanchard Professor of Chemistry

Dr. Marsha I. Lester, Edmund J. Kahn Distinguished Professor

Dr. Michael R. Topp, Professor of Chemistry

DEDICATION

To my parents for their love and support that raises me up.

To my wife without whom I could not survive the difficulties along the way and become the person I am.

ACKNOWLEDGMENT

I would like to thank my advisor Dr. Joseph Subotnik whom it is my greatest fortune and honor to work with. His support and help in both my research and life has been invaluable in these unforgettable five years' experience as an international student. He is knowledgeable and willing to teach and help me with the best of his expertise when I stumbled in my research. He is accommodating and creates a great environment for everyone in the group. His enthusiasm in science has inspired me to learn more and deeper. His critical thinking has motivated me to think differently and comprehensively. Going through five years for the Ph.D. is definitely not easy, but Dr. Subotnik has made it tractable and enjoyable and more meaningful.

I would also like to thank my dissertation committee: Dr. Andrew Rappe, Dr. Marsha Lester and Dr. Michael Topp. It is my great pleasure to be able to have them in my committee and they have provided me with invaluable advice along the way to today. Without them, I could not have been as successful today.

My sincere gratitude goes to the Subotnik's group as well: Dr. Brian Landry, Dr. Ethan Alguire, Dr. Xinle Liu, Dr. Andrew Petit, Dr. Amber Jain, Dr. Greg Medders, Qi Ou, Wenjie Dou, Nicole Bellonzi, Zuxin Jin, and Gaohan Miao. It is my great fortune to be able to work with these very smart and nice people. Their support and kindness has made my five years smooth and wonderful.

ABSTRACT

UNDERSTANDING SURFACE HOPPING ALGORITHMS AND THEIR APPLICATIONS IN CONDENSED PHASE SYSTEMS

Wenjun Ouyang

Dr. Joseph E. Subotnik

While electron transfer plays an important role in a variety of fields, our understanding of electron transfer relies heavily on quantum mechanics. Given the high computational cost of quantum mechanics calculations and the limits of a computer's capability nowadays, the straightforward use of the Schrödinger equation is extremely limited by the dimensionality of the system, which has spurred the advent of many approximate methods. As a mixed quantum-classical approach, fewest-switches surface hopping (FSSH) can treat many nuclei as classical particles while retaining the quantum nature of electrons. However appealing, though, FSSH has some notable drawbacks: FSSH suffers from over-coherence (in addition to its inability to capture presumably rare nuclear quantum effects). Here, in this thesis, we revisit the issue of decoherence from the perspective of entropy, unraveling the nature of the erroneous coherence associated with FSSH trajectories and further justifying the improvements made by the recently proposed augmented-FSSH. Going beyond traditional Tully-style surface hopping technique, we also study new flavors of surface hopping that treat a manifold of electronic states to capture dynamics near metal surfaces. Moreover, we highlight how surface hopping can be used to study electrochemistry and we thoroughly benchmark the surface hopping algorithms against mean-field approaches. This thesis captures 4 years of research which has successfully analyzed the guts of the surface hopping approach for nonadiabatic dynamics both in solution and at a metal surface.

LIST OF CONTENTS

LIST OF ILLUSTRATIONS

CHAPTER 1

Introduction

Electron transfer is a ubiquitous process seen in many applications. For instance, in order to more efficiently harness the solar energy, it is vital for scientists to understand how excited electrons relax within any solar device: if the excited electrons recombine quickly with the holes, we cannot harvest any helpful energy other than heat. Electron transfer also plays a vital role in electrochemistry. The interfacial phenomena in electrochemistry are dominated by the interplay between molecular dynamics, electronic interaction and electron transfer, so understanding electron transfer dynamics is essential for a better understanding of interfacial phenomena.

One straightforward technique to simulate electron transfer is to perform exact quantum dynamics. However tempting, exact quantum dynamics is feasible only for very small systems with low dimensionality because the computational cost increases exponentially. While exact quantum dynamics does not look promising in solving real-life problems, it does serve as a very useful benchmark of other approximate techniques, as we will see in the early chapters of this thesis.

To model realistic systems, one attractive category of approximate techniques is mixed quantum-classical (MQC) methods. In a MQC method, the universe is separated into two parts – one of them is treated quantum mechanically and the other classically – so the computational cost can be reduced dramatically while preserving the desired quantum effects. A typical separation treats electrons quantum mechanically while nuclei classically: the rationale behind this separation is the huge difference in mass between electrons and nuclei, such that nuclear quantum effects are often minuscule while electronic quantum effects are essential in understanding

electron transfer. There are many methods embracing the MQC spirit, including Meyer-Miller-Stock-Thoss (MMST)/Poisson bracket mapping equation (PBME)[1–9], multiple spawning[10–12] and fewest-switches surface hopping (FSSH)[13]. Among the different methods, FSSH is appealing for its simplicity, intuitiveness and high efficiency. Basically, FSSH prescribes that the nuclei are propagated classically on one of all involved potential energy surfaces (active PES) and the electronic wave function is propagated according to the Schrödinger equation under the instantaneous nuclear configuration; the electronic transitions dictated by the change of electronic wave function are modeled by nuclei hoppings between PESs (i.e. changing the active surface). Thus the nuclear dynamics influence the electronic dynamics through the instantaneous nuclear configuration, and the electronic dynamics exert feedback on the nuclear dynamics via induced hops between PESs. In practice, FSSH usually runs in the adiabatic basis.

We will briefly review the basics of FSSH here. We consider a Hamiltonian in a diabatic basis:

$$\mathbf{H} = \mathbf{T}_n + \mathbf{H}_e \tag{1.1}$$

where $\mathbf{T}_n$ is the nuclear kinetic energy operator and $\mathbf{H}_e$ is the electronic Hamiltonian. By diagonalizing $\mathbf{H}_e$, we obtain the electronic Hamiltonian in adiabatic basis:

$$\mathbf{H}_e = \sum_j V_{jj} \left|\Phi_j\right\rangle \left\langle\Phi_j\right| \tag{1.2}$$

where V_{jj} is the adiabatic energy (PES) of state j and $\left|\Phi_j\right\rangle$ is the corresponding adiabat. We further define the derivative coupling as:

$$\mathbf{d}_{ij}(\mathbf{R}) = \left\langle\Phi_i(\mathbf{r};\mathbf{R})\left|\nabla_{\mathbf{R}}\Phi_j(\mathbf{r};\mathbf{R})\right.\right\rangle \tag{1.3}$$

We expand the electronic wave function using the adiabats:

$$|\Psi(\mathbf{r},\mathbf{R},t)\rangle = \sum_j c_j(t)\,|\Phi_j(\mathbf{r};\mathbf{R})\rangle \tag{1.4}$$

Here $c_j(t)$ are the time-dependent expansion coefficients. According to the Schrödinger equation, the equation of motion for the coefficients is:

$$\begin{aligned} i\hbar\dot{c}_i &= \sum_j c_j \left(V_{ij} - i\hbar \left\langle \Phi_i \middle| \dot{\Phi}_j \right\rangle\right) \\ &= \sum_j c_j \left(V_{ij} - i\hbar\dot{\mathbf{R}}\cdot\mathbf{d}_{ij}\right) \end{aligned} \tag{1.5}$$

According to FSSH, we make the ansatz that the equation of motion for the nuclei is simply Newtonian:

$$\frac{dR^\alpha}{dt} = \frac{P^\alpha}{M^\alpha} \tag{1.6}$$

$$\frac{dP^\alpha}{dt} = -\nabla_\alpha V_{\lambda\lambda}(\mathbf{R}) \tag{1.7}$$

Here α labels a classical degree of freedom and λ is the label for active surface.

Now, let us turn our attention to the hopping probability. We first define the electronic density matrix element as:

$$a_{ij} \equiv c_i c_j^* \tag{1.8}$$

With this definition, the population on state i is simply a_{ii} while the time derivative of the population will be:

$$\dot{a}_{ii} = \sum_{i\neq j} b_{ij} = \sum_{i\neq j} \left[2\hbar^{-1}\,\mathrm{Im}(a_{ji}V_{ij}) - 2\,\mathrm{Re}(a_{ji}\dot{\mathbf{R}}\cdot\mathbf{d}_{ij})\right] \tag{1.9}$$

As a sidenote, in the adiabatic basis the first term will be zero as $V_{ij} = 0$ for $i \neq j$. The b_{ij} can be interpreted as the population reduction on state i that enters state j. The hopping probability from active state λ to another state j can be defined as:

$$g_{\lambda j} = \frac{\Delta t b_{j\lambda}}{a_{\lambda\lambda}} \tag{1.10}$$

Δt is the time step in the simulation. Eq. (1.10) was guessed by Tully[13] to be the hopping probability between adiabatic PESs. Thus, to determine if we need to hop to another state, we first set all negative $g_{\lambda j}$ to zero. We then compare a random number ξ (between 0 and 1) to $g_{\lambda j}$ in the following fashion. Assuming $\lambda = 1$, if $\xi < g_{12}$ we attempt to hop to state 2. If $g_{12} < \xi < g_{12} + g_{13}$ we attempt to hop to state 3, etc. Before we actually change the active surface, however, we need to conserve the energy of the trajectory by scaling the momentum (assuming that we hop from state λ to state j):

$$\mathbf{P}^{new} = \mathbf{P} + \Delta P \hat{\mathbf{d}}_{\lambda j}(\mathbf{R}) \tag{1.11}$$

$$\sum_{\alpha} \frac{(P^{\alpha,new})^2}{2M^{\alpha}} + V_{jj}(\mathbf{R}) = \sum_{\alpha} \frac{(P^{\alpha})^2}{2M^{\alpha}} + V_{\lambda\lambda}(\mathbf{R}) \tag{1.12}$$

Here $\hat{\mathbf{d}}_{\lambda j}(\mathbf{R})$ is the normalized derivative coupling vector at configuration $\mathbf{R}$. If $\mathbf{P}^{new}$ is a complex number, the hop is not energetically feasible so the hop is frustrated and the active surface remains unchanged. Otherwise the hop is allowed, the active surface is changed and the momentum is scaled. The premise of rescaling in the direction of the derivative coupling was first suggested and justified by Herman[14–19], and later incorporated by Tully[13].

FSSH is not without its issues or limitations. One significant issue is the over-coherence problem, i.e. lack of decoherence. The decoherence issue also emerges

when one derives FSSH rigorously[20]. Essentially, FSSH never damps the coherence between wavepackets on different PESs, so spurious phenomena appear when two wavepackets move away from each other. The errors associated with over-coherence can be consequential given that dephasing and decoherence phenomena for photo-excited molecules is crucial[21,22]. Previously, many researchers have proposed schemes to add decoherence to the FSSH algorithm[20,23–38]. With this in mind, we will survey the decoherence issue in chapter 2. However, we will focus on a subject which has often been neglected, namely the entropy production of surface hopping algorithm. We find that FSSH cannot conserve the entropy of a closed system, rather the entropy increases when electronic transition occurs. That being said, if we consider only the electronic subsystem, we find FSSH performs better in recovering the exact entropy. Nevertheless, in order to reproduce the exact entropy for the model problems, we show that additional decoherence must be imposed on the FSSH algorithm. In particular, if we invoke a corrected algorithm – augmented-FSSH (A-FSSH)[39,40] – entropic results are greatly improved. Using a frozen Gaussian analysis, we further derive an analytical expression for estimating the error in entropy as predicted by FSSH. This calculation also highlights why, by eliminating the highly oscillatory coherence when the two wavepackets move apart, A-FSSH improves the stability of long time dynamics.

In chapter 3, we will investigate another limitation of FSSH. In this chapter, we focus on the fact that, according to FSSH, electronic states are handled by exact quantum dynamics, i.e. the Schödinger equation. Just as we have learned from the story of exact quantum dynamics above, computational cost increases exponentially if there are a large number of electronic states presented; thus, electron transfer between molecules when a electronic bath is presented is difficult for standard FSSH because of the high computational cost associated with evolving electronic wave functions. Other

than issues of efficiency, frustrated hops in FSSH – which are essential for maintaining detailed balance – can also lead to artifacts with very many electronic states. To go beyond standard FSSH, we note that surface-leaking (SL)[41] was suggested long ago to simulate incoherent relaxation into an electronic bath but lacks the capability of modeling nonadiabatic electronic transitions. The basic idea of surface leaking is that when an excited molecule couples to a electronic bath, the electron can stochastically leak into the continuum. When the electron leaks into the continuum, the nuclei will make a vertical transition to the lower state. Please see Fig. 1.1 for a schematic figure of the surface-leaking algorithm.

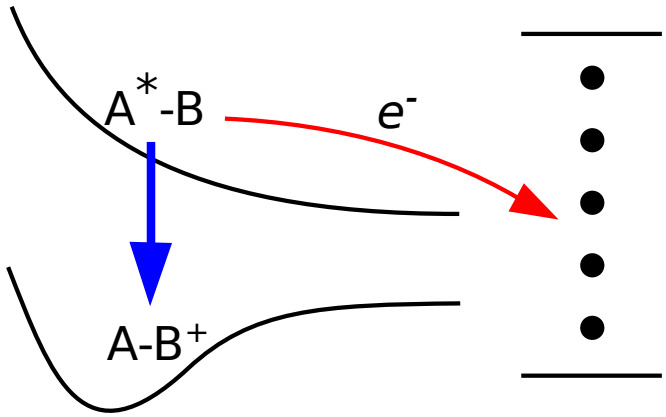

Figure 1.1: Schematic figure of the surface-leaking algorithm. A^* denotes the excited state of atom (or molecule) A and B is another atom (or molecule) in its ground state. The upper state is coupled to the continuum of states on the right hand side. After the electron leaks into the continuum, the nuclei will make a vertical transition to the lower state.

By incorporating surface-leaking into FSSH, in chapter 3 we propose a new algorithm SL-FSSH that successfully captures the lifetime of the discrete states within the wide band limit as well as nonadiabatic transitions between discrete states with reasonable accuracy. SL-FSSH is far more efficient than standard FSSH for treating an electronic continuum because the latter requires an discretization of the continuum, whereas the former invokes an implicit treatment. That being said, when bench-

marking SL-FSSH, we will find only partial success when going beyond the wide band approximation. In particular the narrow band limit is captured but the transition between wide and narrow band is incorrectly predicted. Further study is required to capture the electronic relaxation beyond the wide band limit.

Now, the SL technique just discussed (chapter 3) is limited to gas phase phenomena. In chapters 4-5, we will study new SH-like techniques for treating molecules near metal surfaces. While many researchers in electrochemistry focus on the statistical mechanics of interfacial phenomena, the dynamics of electron transfer between a metal surface and a molecule nearby can be modeled by a surface hopping (SH) approach known as a Classical Master Equation (CME)[42]. For such a system, FSSH is not feasible because of the intractable computational complexity associated with the large number of states used to model the metal surface. Note here, Shenvi *et al.*[43–45] have discretized the continuum of states modeling the metal and run independent-electron surface hopping (IESH) on the discretized states. While IESH is more efficient than FSSH, one still has to deal with a large number of states. By contrast, by adopting an implicit treatment of the continuum of electronic states, the CME does not need to propagate the wave function as in Eq. (1.5) and the computational complexity is reduced dramatically. Basically, the probability of electron transfer is dictated by both the energy difference associated with the change of charge state and the Fermi level of the metal surface.

To describe a CME mathematically, we define the Hamiltonian in the context of

Anderson-Holstein model:

$$H = H_s + H_b + H_c, \tag{1.13a}$$

$$H_s = E(x)d^\dagger d + V_0(x) + \frac{p^2}{2m}, \tag{1.13b}$$

$$H_b = \sum_k \left(\epsilon_k - \mu\right) c_k^\dagger c_k, \tag{1.13c}$$

$$H_c = \sum_k W_k \left(c_k^\dagger d + d^\dagger c_k\right), \tag{1.13d}$$

d and $d^\dagger$ are the annihilation and creation operator for electronic impurity level. c_k and $c_k^\dagger$ are the annihilation and creation operator for electronic bath states. μ is the Fermi level of the electronic bath. If $V_0(x)$ is the diabatic PES for the unoccupied state, we define the diabatic PES for the occupied state to be:

$$V_1(x) \equiv V_0(x) + E(x). \tag{1.14}$$

The simplest classical master equation can be written as:

$$\begin{aligned}
\frac{\partial P_0(x,p,t)}{\partial t} =& \frac{\partial V_0(x,p)}{\partial x}\frac{\partial P_0(x,p,t)}{\partial p} - \frac{p}{m}\frac{\partial P_0(x,p,t)}{\partial x} \\
&- \frac{\Gamma}{\hbar} f\left(E(x)\right) P_0(x,p,t) \\
&+ \frac{\Gamma}{\hbar}\left(1 - f\left(E(x)\right)\right) P_1(x,p,t), \qquad (1.15a) \\
\frac{\partial P_1(x,p,t)}{\partial t} =& \frac{\partial V_1(x,p)}{\partial x}\frac{\partial P_1(x,p,t)}{\partial p} - \frac{p}{m}\frac{\partial P_1(x,p,t)}{\partial x} \\
&+ \frac{\Gamma}{\hbar} f\left(E(x)\right) P_0(x,p,t) \\
&- \frac{\Gamma}{\hbar}\left(1 - f\left(E(x)\right)\right) P_1(x,p,t). \qquad (1.15b)
\end{aligned}$$

Here P_i is the population density on state i, $f(\epsilon) \equiv 1/(1 + e^{\beta(\epsilon-\mu)})$ is the Fermi function with $\beta \equiv 1/(k_b T)$. $\Gamma/\hbar$ is the hybridization function denoting the electronic

coupling between molecule and metal surface. The first two terms in each equation capture the classical propagation of the population P_i along surface V_i while the second two terms dictate the population hopping between two states. In Fig. 1.2, we plot V_0 and V_1 for the simplest case: two displaced harmonic oscillators.

In chapter 4, using a very simple molecular dynamics force field combined with Eq. (1.15), we will simulate the electronic transport through an ionic solution assuming weak electronic coupling between metal and molecule. Beyond showing steady state currents, we will compare nonequilibrium results with those from linear response theory to demonstrate nonequilibrium effects. These comparisons between nonequilibrium and equilibrium simulations expand our understanding about how the voltage and coupling strength move the system away from equilibrium. Furthermore, we build a kinetic model to reveal the competition between two major processes involved: mass transport of charge carriers and electron transfer at the electrode surface. The competition is often ignored in simple linear response theories and, by employing the kinetic model and applying the nonequilibrium velocity profile, we are able to converge linear response results to our nonequilibrium simulation results. In the future, a more challenging task will be to consider interfacial reactions as well. One easy means to do so would be to change the force field so as to simulate the trapping of charge carriers on the electrode surface. However, a more realistic model really requires a much more sophisticated treatment of electron structure and electron transfer. We leave this task to the next generation of students.

Finally in chapter 5, we study electron transfer in both the strong and weak electronic coupling regimes. We will survey and benchmark two different approaches, namely electronic friction (EF)[46] and surface hopping (SH/CME)[47], using a generalized Anderson-Holstein (AH) model to understand the limitations of each approach. We note that there is actually a limited literature for studying barrier crossings in the

presence of a manifold of electronic states at high temperature using MQC dynamics. Most research into the AH model has focused on low temperature physics[48–59].

Now, unlike SH/CME dynamics, EF models nuclear dynamics using a potential of mean force (PMF, Eq. (1.16)) and employs an extra electronic friction (Eq. (1.17)) to model the coupling of nuclear motion to the manifold of electronic states. The PMF ($U(x)$) and electronic friction (γ_e) are defined as

$$U(x) = V_0(x) - \frac{1}{\beta}\log\left(1 + e^{-\beta E(x)}\right). \tag{1.16}$$

$$\gamma_e = \frac{\hbar\beta}{\Gamma} f(E(x))(1 - f(E(x)))\left(\frac{dE(x)}{dx}\right)^2. \tag{1.17}$$

See Fig. 1.2 for a comparison between diabatic PESs and PMF, and the electronic friction with small and large electronic coupling. Here, as above, we take the simplest case where V_0 and V_1 are chosen as dispalced harmonic oscillators. The CME (Eq. (1.15)) and the EF (Eqs. (1.16)-(1.17)) offer two very different perspectives on nonadiabatic dynamics. The former should be valid with weak molecule-metal coupling, the latter with strong molecule-metal coupling. Notice that, according to EF dynamics (Eq. (1.17) and Fig. 1.2), the friction is strongest when the two diabats cross, such that the electron is constantly hopping back and forth between molecule and metal.

Surprisingly, in chapter 5, using a shifted harmonic model problem, we find that EF agrees with the Marcus's theory even in the nonadiabatic limit. Furthermore, we find a connection between the Kramer's theory in the overdamped limit and the Marcus's theory, which justifies the correctness of EF dynamics in the nonadiabatic limit. This hidden connection is perhaps the most exciting result of the present thesis. That being said, however, we also note that, when excited state dynamics becomes important, EF fails to account for the additional electron transfer channel resulting

from excited dynamics.

Finally, among all the algorithms studied in this thesis, we find a newly proposed broadened CME (BCME)[60,61] performs very well in all the cases and we anticipate BCME should perform well when describing more realistic systems. According to the BCME, one effectively runs simulation with SH dynamics on two broadened diabatic surfaces. See Fig. 5.1(a) in chapter 5.

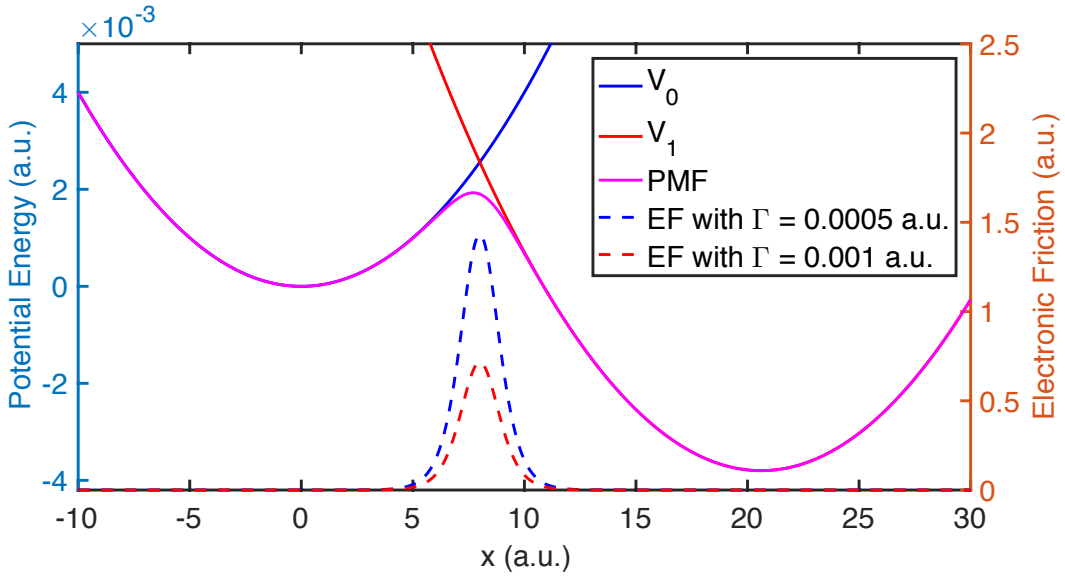

Figure 1.2: Diabatic PESs (V_0 and V_1), PMF (Eq. (1.16)) and electronic friction (Eq. (1.17)) with small ($\Gamma = 0.0005$ a.u.) and large ($\Gamma = 0.001$ a.u.) electronic coupling.

In the end, this thesis summarizes 4 years of research analyzing how to model nonadiabatic dynamics both in solution and at a metal surface. Several interesting results are presented in chapters 2-5. Looking forward, the most interesting question is how well the BCME performs in a more realistic condensed phase system. Beyond electron transfer, modeling chemical reactions at metal surfaces in real time is essential but challenging at present. This should be the next big challenge going forward.

CHAPTER 2

Estimating the Entropy and Quantifying the Impurity of a Swarm of Surface-Hopping Trajectories: A New Perspective on Decoherence

This chapter is adapted from The Journal of Chemical Physics, Volume 140, Issue 20, Page 204102, 2014.

2.1 Introduction

If the universe is governed by the laws of quantum mechanics and began originally in a pure state (with zero total entropy), then the universe must always remain in a pure state thereafter (with zero total entropy). If the universe (with N particles) is governed by the laws of classical mechanics with density $\rho(\vec{R}, \vec{P}, 0)$ in phase space at time 0, then the total time-dependent entropy

$$S_{cl}(t) = \iint \rho(\vec{R}, \vec{P}) \log(\rho(\vec{R}, \vec{P}) h^{3N}) dR^{3N} dP^{3N} \tag{2.1}$$

will be conserved throughout time, $\partial S_{cl}/\partial t = 0$. Now both of these predictions do not match up with the second law of thermodynamics. Starting with Boltzmann's celebrated H-theorem[62,63] there has been a great deal of literature explaining how the "effective" entropy of the entire universe tends to grow, provided that one defines the "effective" entropy as the sum of the entropy of many individual subsystems (each entangled with their surroundings). These entropic statements hold both for quantum and classical mechanics. For example, in the case of Boltzmann's H-theorem describing a dilute gas, the "effective" entropy (S_H) that tends to grow in time (until equilibrium is reached) is the entropic integral of the reduced, one-particle distribution

function:

$$f(R,P) = N \int \cdots \int \rho(R, R_2, \ldots R_{3N}, P, P_2, \ldots P_{3N}) dR_2 \ldots dR_{3N} dP_2 \ldots dP_{3N} \quad (2.2)$$

$$S_H(t) = \iint f(R,P) \log(f(R,P)h) dR dP \quad (2.3)$$

Because the notion of quantum entropy is different from the notion of classical entropy, the question of entropy evolution inevitably arises for mixed quantum-classical simulations. In particular, for Tully's fewest switches surface hopping (FSSH) algorithm (which is used extensively nowadays to simulate the dynamics of electronic relaxation[38,64–70]), one expects interesting questions about entropy to manifest themselves for the FSSH algorithm. After all, by treating quantum electrons separately from classical nuclei, nuclear-electronic coherence and decoherence can become fuzzy and counting states (and measuring entropy) may be nontrivial.

To our knowledge, to date there has been no standard definition for the total entropy of a FSSH calculation, much less a discussion about the role of entropy in FSSH nonadiabatic dynamics. While many researchers (including the authors) in the past have focused on "decoherence" corrections to the FSSH algorithm that aim to fix up the algorithm[20,23–38] , the total entropy of a FSSH calculation has not been quantified previously nor have the origins of irreversibility in FSSH dynamics been fully explored (though the question of detailed balance has been studied[71,72]). Given the importance of dephasing and decoherence phenomena[21,22] for photo-excited molecules (with a system of electrons and a bath of nuclei), we believe a thorough analysis of surface-hopping entropy is prudent, and the goal of the present paper is to provide such an analysis in detail.

To achieve this goal, we will draw heavily from a set of recent articles[20,73] that provide a rigorous framework for deriving approximately the FSSH algorithm starting

from the Martens-Kapral mixed quantum classical Liouville equation (QCLE)[74–83]. In particular, according to Refs. 20,73, there is a simple prescription for approximating the partial Wigner transform of the full nuclear-electronic density matrix starting from a swarm of FSSH trajectories. From such a prescription, we will calculate the impurity of an FSSH calulation (i.e. one minus the purity) which can serve as an approximate "FSSH entropy" for systems that are nearly pure.

Finally, armed with a tool to calculate impurity, we will show that total impurity is not conserved for a closed quantum system propagated by FSSH dynamics. In other words, even though a pure quantum state in a closed system should remain pure forever, the impurity of a FSSH calculation increases, as if there is always some external friction that mixes pure states and moves the system toward equilibrium. We will examine why impurity increases and how decoherence emerges in the context of partially Wigner transformed wavepackets. Inevitably, our analysis will reach back to the approximations invoked in Ref. 20. Specifically, according to Ref. 20, FSSH dynamics will approximate true QCLE dynamics provided that (i) wavepacket separation is not followed by wavepacket recoherence and (ii) the equation of motion (EOM) for the off-diagonal electronic density matrix element is modified from the original time-dependent electronic Schrödinger equation. Formally, modifying the off-diagonal EOM requires a swarm of interacting (rather than independent) FSSH trajectories, but we have argued that approximations for independent trajectories are possible (e.g., A-FSSH[39,40]). Modification of the off-diagonal EOM is necessary to force the electronic coherences between surfaces 1 and 2 to move along the average surface – with a force $(F_1+F_2)/2$ – as the QCLE stipulates. (This notion of an average surface has also been discussed by many other authors[84–87].) As we will show, the two approximations discussed here have consequences for the impurity (and entropy) of a FSSH calculation.

An outline of this article is as follows. In Section 2.2, we review the different definitions of impurity for a Wigner wavepacket moving on one electronic surface. In Section 2.3, we make a straightforward definition of impurity for a Wigner wavepacket moving along multiple electronic energy surfaces, and in Sections 2.3.1, 2.3.2, we verify that this new definition of impurity is conserved by both the Schrödinger equation and the QCLE for a partially Wigner transformed density matrix. In Section 2.3.3, we define the impurity for a FSSH calculation. In Section 2.4, we present results for two model Hamiltonians together demonstrating that surface hopping methods do not conserve the total impurity of the universe. Finally in Section 2.5, we rationalize this increase in impurity by studying the case of two frozen Gaussians, where an apparently mixed (i.e. not pure) density matrix arises when one ignores off-diagonal elements of the partial Wigner density matrix that oscillate rapidly in phase space. In this sense, decoherence emerges as the result of a stationary phase approximation. For a seasoned practitioner of surface hopping, who may not be surprised to learn that FSSH dynamics do not conserve the total impurity of the universe, note that this article presents a new analytic formulat for estimating FSSH impurity (in Section 2.5.2).

Our notation will be as follows. For indices, i, j, k label adiabatic electronic states; M, L, K label joint nuclear-electronic states; α is a general nuclear coordinate; μ and η are indices for a grid point in phase space. For physical quantities, $\boldsymbol{\rho}$ refers to the full nuclear-electronic density matrix; Φ denotes an adiabatic electronic wavefunction; Ψ is a joint nuclear-electronic wavefunction; A_{ij} is the partially Wigner transformed density matrix calculated from surface hopping data; and A_{ij}^W is the exact partially Wigner transformed density matrix.

2.2 Background: The Entropy of a Wigner Wavepacket on One Electronic Surface

While there are many ways to calculate the quantum entropy[88], the only approach that satisfies all of the Shannon constraints[89] is the von Neumann entropy:

$$S = -\operatorname{Tr}(\boldsymbol{\rho} \ln \boldsymbol{\rho}) \tag{2.4}$$

where $\boldsymbol{\rho}$ is the quantum density matrix. Unfortunately, in practice, calculating the logarithm in Eq. (2.4) requires diagonalization of the density matrix, which is not realistic in general for systems with many nuclear degrees of freedom.

For this article, we would like to calculate an approximate entropy of a general Wigner wavepacket in phase space, which is a subject with a long history[88]. For one electronic surface, the Wigner transform is defined by

$$A^W(\vec{R}, \vec{P}, t) = \frac{1}{2\pi\hbar} \int d\vec{X} e^{i\vec{P}\cdot\vec{X}/\hbar} \left\langle \vec{R} - \frac{\vec{X}}{2} \middle| \boldsymbol{\rho}(t) \middle| \vec{R} + \frac{\vec{X}}{2} \right\rangle \tag{2.5}$$

As is well known, $A^W(\vec{R}, \vec{P}, t)$ can take on negative values and thus, however tempting, one cannot simply apply Eq. (2.1) by substituting $\rho_{cl}(\vec{R}, \vec{P}) = A^W(\vec{R}, \vec{P})$. Of course, one could transform to the Husimi distribution, but then the equation of motion becomes significantly more complicated. As a practical matter, for a Wigner wavepacket, we require a tractable and easy means to evaluate entropy.

Beyond the von Neumann entropy, a feasible way to estimate the entropy has been proposed as one minus the purity (impurity)[88,90,91]:

$$S(t) = 1 - (2\pi\hbar)^D \int d\vec{R} d\vec{P} \left(A^W(\vec{R}, \vec{P}, t) \right)^2 \tag{2.6}$$

where D is the number of degrees of freedom. Eq. (2.6) has a number of appealing properties:

- The impurity is conserved in time according to the time-dependent Schrödinger equation.
- The impurity is 0 for pure states.
- The impurity is positive for mixed states.

Below, we will generalize Eq. (2.6) to the case of many electronic states, and thus evaluate the impurity of a FSSH calculation. Note that, formally, the defintion of impurity in Eq. (2.6) is a valid approximation of the von Neumann entropy Eq. (2.4) only when the universe is close to pure, so that one can expand the density matrix $\boldsymbol{\rho} = 1 - \boldsymbol{z}$ in powers of $\boldsymbol{z}$.

2.3 The Impurity of a Partial Wigner Wavepacket on Multiple Electronic Surfaces

For a physical problem with multiple PESs, the partially Wigner transformed density matrix is[81,82]

$$A_{ij}^{W}(\vec{R},\vec{P},t) \equiv \left(\frac{1}{2\pi\hbar}\right)^{3N} \int d\vec{X} e^{i\vec{P}\cdot\vec{X}/\hbar} \left\langle \Phi_i(\vec{R}); \vec{R} - \frac{\vec{X}}{2} \right| \boldsymbol{\rho}(t) \left| \Phi_j(\vec{R}); \vec{R} + \frac{\vec{X}}{2} \right\rangle \quad (2.7)$$

where $\left\{ \left| \Phi_i(\vec{R}) \right\rangle \right\}$ are the basis of adiabatic electronic wavefunctions at nuclear position $\vec{R}$ and N is the number of nuclei. In this case, the natural extension of Eq. (2.6)

is to calculate the impurity as:

$$\begin{aligned} S(t) &\equiv 1 - (2\pi\hbar)^{3N} \int d\vec{R} \int d\vec{P}\, \mathrm{Tr}\left(\mathbf{A}^W(\vec{R},\vec{P},t)^2\right) \\ &= 1 - (2\pi\hbar)^{3N} \sum_{i,j} \int d\vec{R} \int d\vec{P} A^W_{ij}(\vec{R},\vec{P},t) \cdot A^W_{ji}(\vec{R},\vec{P},t) \end{aligned} \tag{2.8}$$

2.3.1 Exact Dynamics from the Schrödinger Equation

To prove that Eq. (2.8) is a meaningful definition of impurity for a system with several accessible electronic states, we must first prove that, according to this definition, impurity is conserved in time when a closed system is propagated by the Schrödinger equation. To prove this fact, one starts from a density matrix

$$\boldsymbol{\rho} = \sum_{K=1}^{N_K} b_K \left|\Psi_K(t)\right\rangle \left\langle\Psi_K(t)\right| \tag{2.9}$$

In principle, $\boldsymbol{\rho}$ can represent a pure state ($N_K = 1$) or a mixed state ($N_K > 1$). The set $\{|\Psi_K(t)\rangle\}$ here denote a basis of orthonormal, fully coupled nuclear-electronic wavefunctions. By substituting Eq. (2.9) into Eq. (2.7) and using the identity $\int d\vec{P} e^{i\vec{P}\cdot\vec{X}} =$

$(2\pi)^{3N}\delta(\vec{X})$, one can calculate the impurity in Eq. (2.8):

$$\begin{aligned}
S(t) &= 1-(2\pi\hbar)^{-3N}\sum_{M,L} b_M b_L \int d\vec{P}\int d\vec{R}\sum_{i,j}\int d\vec{X}\int d\vec{Y} e^{i\vec{P}\cdot(\vec{X}+\vec{Y})/\hbar} \\
&\quad \times \left\langle \Phi_i(\vec{R});\vec{R}-\frac{\vec{X}}{2}\right| \Psi_M(t)\Big\rangle \Big\langle \Psi_M(t)\left|\Phi_j(\vec{R});\vec{R}+\frac{\vec{X}}{2}\right\rangle \\
&\quad \times \left\langle \Phi_j(\vec{R});\vec{R}-\frac{\vec{Y}}{2}\right| \Psi_L(t)\Big\rangle \Big\langle \Psi_L(t)\left|\Phi_i(\vec{R});\vec{R}+\frac{\vec{Y}}{2}\right\rangle \\
&= 1-\sum_{M,L} b_M b_L \int d\vec{R}\sum_{i,j}\int d\vec{X}\int d\vec{Y}\,\delta(\vec{X}+\vec{Y}) \\
&\quad \times \left\langle \Phi_i(\vec{R});\vec{R}-\frac{\vec{X}}{2}\right| \Psi_M(t)\Big\rangle \Big\langle \Psi_M(t)\left|\Phi_j(\vec{R});\vec{R}+\frac{\vec{X}}{2}\right\rangle \\
&\quad \times \left\langle \Phi_j(\vec{R});\vec{R}-\frac{\vec{Y}}{2}\right| \Psi_L(t)\Big\rangle \Big\langle \Psi_L(t)\left|\Phi_i(\vec{R});\vec{R}+\frac{\vec{Y}}{2}\right\rangle \\
&= 1-\sum_{M,L} b_M b_L \int d\vec{R}\int d\vec{X} \\
&\quad \times \left(\sum_i \left\langle \Phi_i(\vec{R});\vec{R}-\frac{\vec{X}}{2}\right| \Psi_M(t)\Big\rangle \Big\langle \Psi_L(t)\left|\Phi_i(\vec{R});\vec{R}-\frac{\vec{X}}{2}\right\rangle\right) \\
&\quad \times \left(\sum_j \left\langle \Phi_j(\vec{R});\vec{R}+\frac{\vec{X}}{2}\right| \Psi_L(t)\Big\rangle \Big\langle \Psi_M(t)\left|\Phi_j(\vec{R});\vec{R}+\frac{\vec{X}}{2}\right\rangle\right) \qquad (2.10)
\end{aligned}$$

Now, using the fact that the set of adiabatic electronic eigenstates $\left\{\left|\Phi_i(\vec{R})\right\rangle\right\}$ is complete, so that an electronic trace is invariant to the nuclear position associated with the adiabats,

$$\begin{aligned}
S(t) &= 1-\sum_{M,L} b_M b_L \int d\vec{R}\int d\vec{X}\,\mathrm{Tr}_e\left[\left\langle \vec{R}-\frac{\vec{X}}{2}\right| \Psi_M(t)\Big\rangle \Big\langle \Psi_L(t)\left|\vec{R}-\frac{\vec{X}}{2}\right\rangle\right] \\
&\quad \times \mathrm{Tr}_e\left[\left\langle \vec{R}+\frac{\vec{X}}{2}\right| \Psi_L(t)\Big\rangle \Big\langle \Psi_M(t)\left|\vec{R}+\frac{\vec{X}}{2}\right\rangle\right] \qquad (2.11)
\end{aligned}$$

where Tr_e signifies a trace over electronic states. Now, switching variables to

$$\vec{\omega}_1 = \vec{R} + \frac{\vec{X}}{2}, \quad \vec{\omega}_2 = \vec{R} - \frac{\vec{X}}{2}, \quad \int d\vec{R} \int d\vec{X} \rightarrow \int d\vec{\omega}_2 \int d\vec{\omega}_1 \tag{2.12}$$

we find that the expression for impurity reduces to:

$$\begin{aligned} S(t) &= 1 - \sum_{M,L} b_M b_L \, \mathrm{Tr}_e \, \mathrm{Tr}_n \left[\, |\Psi_M(t)\rangle \, \langle \Psi_L(t)| \, \right] \mathrm{Tr}_e \, \mathrm{Tr}_n \left[\, |\Psi_L(t)\rangle \, \langle \Psi_M(t)| \, \right] \\ &= 1 - \sum_{M,L} b_M b_L \, |\langle \Psi_M(t) | \Psi_L(t) \rangle|^2 \\ &= 1 - \sum_{M} b_M^2 \end{aligned} \tag{2.13}$$

where Tr_n is the trace over nuclei. Thus, in the end, the impurity according to Eq. (2.8) is clearly time independent and satisfies our intrinsic notation of impurity: it is zero for pure states and positive for mixed states. Note that, in Eq. (2.13), $S(t)$ is in fact identical to the fully quantum mechanical impurity, $S(t) = 1 - \mathrm{Tr}(\boldsymbol{\rho}^2)$. This agreement between the semiclassical and quantum mechanical impurities arises only because the impurity in Eq. (2.8) is second order in the density matrix. More generally, we are unaware of a simple semiclassical formula to estimate even $\mathrm{Tr}(\boldsymbol{\rho}^4)$ (much less $\mathrm{Tr}(\boldsymbol{\rho} \ln \boldsymbol{\rho})$) starting from the Wigner representation.

2.3.2 The Quantum-Classical Liouville Equation (QCLE)

Having proved that the impurity in Eq. (2.8) is conserved according to exact quantum dynamics, we can show that the impurity of Eq. (2.8) is also conserved in time exactly by the QCLE. To prove this statement, note that the time derivative of the impurity

is

$$\begin{aligned}\frac{\partial S}{\partial t} &= -(2\pi\hbar)^{3N}\sum_{i,j}\int d\vec{R}\int d\vec{P}\left\{\frac{\partial}{\partial t}A_{ij}^{W}(\vec{R},\vec{P},t)\cdot A_{ji}^{W}(\vec{R},\vec{P},t)\right. \\ &\qquad \left. + A_{ij}^{W}(\vec{R},\vec{P},t)\cdot\frac{\partial}{\partial t}A_{ji}^{W}(\vec{R},\vec{P},t)\right\} \\ &= -(2\pi\hbar)^{3N}\sum_{i,j}2\int d\vec{R}\int d\vec{P}\,\mathrm{Re}\left(\frac{\partial}{\partial t}A_{ij}^{W}(\vec{R},\vec{P},t)\cdot A_{ji}^{W}(\vec{R},\vec{P},t)\right) \quad (2.14)\end{aligned}$$

According to the QCLE, the partially Wigner transformed density matrix evolves according to

$$\begin{aligned}\frac{\partial}{\partial t}A_{ij}^{W}(\vec{R},\vec{P},t) &= \frac{-i}{\hbar}\sum_{k}\left(V_{ik}A_{kj}^{W}-A_{ik}^{W}V_{kj}\right)-\sum_{k,\alpha}\frac{P^{\alpha}}{M^{\alpha}}\left(d_{ik}^{\alpha}A_{kj}^{W}-A_{ik}^{W}d_{kj}^{\alpha}\right) \\ &\quad -\sum_{\alpha}\frac{P^{\alpha}}{M^{\alpha}}\frac{\partial A_{ij}^{W}}{\partial R^{\alpha}}-\frac{1}{2}\sum_{k,\alpha}\left(F_{ik}^{\alpha}\frac{\partial A_{kj}^{W}}{\partial P^{\alpha}}+\frac{\partial A_{ik}^{W}}{\partial P^{\alpha}}F_{kj}^{\alpha}\right) \quad (2.15)\end{aligned}$$

When we substitute Eq. (2.15) into Eq. (2.14), we find that

$$\begin{aligned}\frac{\partial S}{\partial t} &= (2\pi\hbar)^{3N}\int_{-\infty}^{\infty}d\vec{R}\int_{-\infty}^{\infty}d\vec{P}\,\mathrm{Re}\left[\frac{2i}{\hbar}\sum_{i,j,k}\left(V_{ik}A_{kj}^{W}A_{ji}^{W}-A_{ik}^{W}V_{kj}A_{ji}^{W}\right)\right. \\ &\quad +\sum_{i,j,k,\alpha}\frac{2P^{\alpha}}{M^{\alpha}}\left(d_{ik}^{\alpha}A_{kj}^{W}A_{ji}^{W}-A_{ik}^{W}d_{kj}^{\alpha}A_{ji}^{W}\right)+\sum_{i,j,\alpha}\frac{2P^{\alpha}}{M^{\alpha}}\frac{\partial A_{ij}^{W}}{\partial R^{\alpha}}A_{ji}^{W} \\ &\quad \left.+\sum_{i,j,k,\alpha}\left(F_{ik}^{\alpha}\frac{\partial A_{kj}^{W}}{\partial P^{\alpha}}A_{ji}^{W}+\frac{\partial A_{ik}^{W}}{\partial P^{\alpha}}F_{kj}^{\alpha}A_{ji}^{W}\right)\right] \\ &= (2\pi\hbar)^{3N}\int_{-\infty}^{\infty}d\vec{R}\int_{-\infty}^{\infty}d\vec{P}\,\mathrm{Re}\left[\frac{2i}{\hbar}\sum_{i,j}\left(\left(V_{ii}-V_{jj}\right)\left|A_{ij}^{W}\right|^{2}\right)\right. \\ &\quad +\sum_{\alpha}\frac{2P^{\alpha}}{M^{\alpha}}\left(\sum_{i,j,k}d_{ik}^{\alpha}A_{kj}^{W}A_{ji}^{W}-\sum_{i,j,k}A_{ik}^{W}d_{kj}^{\alpha}A_{ji}^{W}\right)+\sum_{i,j,\alpha}\frac{2P^{\alpha}}{M^{\alpha}}\frac{\partial A_{ij}^{W}}{\partial R^{\alpha}}A_{ji}^{W} \\ &\quad \left.+\sum_{\alpha}\left(\sum_{i,j,k}F_{ik}^{\alpha}\frac{\partial A_{kj}^{W}}{\partial P^{\alpha}}A_{ji}^{W}+\sum_{i,j,k}\frac{\partial A_{ik}^{W}}{\partial P^{\alpha}}F_{kj}^{\alpha}A_{ji}^{W}\right)\right] \quad (2.16)\end{aligned}$$

The first two terms are clearly zero (because there is no real part). Now for the third and sixth term, by changing the summation index $\{i,j,k\} \to \{k,i,j\}$, one finds

$$\begin{aligned}
\frac{\partial S}{\partial t} &= (2\pi\hbar)^{3N} \int_{-\infty}^{\infty} d\vec{R} \int_{-\infty}^{\infty} d\vec{P}\, \mathrm{Re}\left[\sum_{\alpha} \frac{2P^{\alpha}}{M^{\alpha}} \left(\sum_{k,i,j} d^{\alpha}_{kj} A^{W}_{ji} A^{W}_{ik} - \sum_{i,j,k} A^{W}_{ik} d^{\alpha}_{kj} A^{W}_{ji} \right) \right. \\
&\quad \left. + \sum_{i,j,\alpha} \frac{2P^{\alpha}}{M^{\alpha}} \frac{\partial A^{W}_{ij}}{\partial R^{\alpha}} A^{W}_{ji} + \sum_{\alpha} \left(\sum_{k,i,j} F^{\alpha}_{kj} \frac{\partial A^{W}_{ji}}{\partial P^{\alpha}} A^{W}_{ik} + \sum_{i,j,k} \frac{\partial A^{W}_{ik}}{\partial P^{\alpha}} F^{\alpha}_{kj} A^{W}_{ji} \right) \right] \\
&= (2\pi\hbar)^{3N} \sum_{i,j,k,\alpha} \int_{-\infty}^{\infty} d\vec{R} \int_{-\infty}^{\infty} d\vec{P} \left[\frac{\partial}{\partial R^{\alpha}} \left(\frac{P^{\alpha}}{M^{\alpha}} A^{W}_{ij} A^{W}_{ji} \right) + \frac{\partial}{\partial P^{\alpha}} \left(A^{W}_{ik} F^{\alpha}_{kj} A^{W}_{ji} \right) \right] \\
&= 0 \qquad (2.17)
\end{aligned}$$

In the last equality, we assume that the density matrix decays to zero sufficiently fast (as it must for any closed system). Thus, the impurity of a partially transformed Wigner wavepacket is conserved in time according to the QCLE. This exact conservation of impurity is somewhat not obvious since the QCLE itself is an approximation of the quantum Liouville equation. In the future, it might prove interesting to explore the time evolution of the true von Neumann entropy defined in Eq. (2.4) (rather than the impurity) according to the QCLE; such an investigation would necessarily be more complicated than the present article.

2.3.3 FSSH Algorithm and the Calculation of Impurity

Let us now describe how to evaluate Eq. (2.8) with data computed from a surface hopping simulation. Without loss of generality, we will restrict ourselves to a system with two electronic states and one spatial dimension. For a typical surface hopping calculation, one is given a swarm of N_s trajectories, each trajectory carrying an active surface variable $\lambda = 1, 2$ (specifying nuclear motion) and a set of electronic amplitudes (c_1, c_2). The partial Wigner transform with elements $A_{11}(R,P,t)$, $A_{22}(R,P,t)$ and

$A_{12}(R,P,t)$ are constructed as follows[73]:

$$A_{ii}(R,P,t) = \frac{1}{N_s}\sum_l \delta(R - R^l(t))\delta(P - P^l(t))\delta_{i,\lambda^l(t)} \tag{2.18}$$

$$A_{ij}(R,P,t) = \frac{1}{N_s}\sum_l \delta(R - R^l(t))\delta(P - P^l(t))\sigma^l_{ij} \tag{2.19}$$

Here, l is the label for each trajectory and σ_{ij} is defined as $c_i c_j^*$. Note that Eq. (2.19) is not unique (according to Ref. 73) but, in our experience, it has been the most numerically stable. Finally, we can calculate the impurity with Eq. (2.8) as:

$$S(t) = 1 - 2\pi\hbar \int dR \int dP (A_{11}(R,P,t)^2 + 2\left|A_{12}(R,P,t)\right|^2 + A_{22}(R,P,t)^2) \tag{2.20}$$

In practice, special care must be taken when evaluating the impurity above because the sum must be evaluated on a finite grid in phase space, with the grid sizes ΔR and ΔP. Let $[R_{min}, R_{min} + \Delta R, \ldots, R_{max} - \Delta R, R_{max}]$ be a grid in position-space, and $[P_{min}, P_{min} + \Delta P, \ldots, P_{max} - \Delta P, P_{max}]$ be a grid in momentum-space. Then, we evaluate the partial Wigner transform at a grid point (R_μ, P_η) by

$$A_{ii}(R_\mu, P_\eta, t) = \frac{1}{N_s}\sum_l \Theta\left(\frac{\Delta R}{2} - \left|R^l(t) - R_\mu\right|\right)\Theta\left(\frac{\Delta P}{2} - \left|P^l(t) - P_\eta\right|\right) \tag{2.21}$$

$$A_{ij}(R_\mu, P_\eta, t) = \frac{1}{N_s}\sum_l \Theta\left(\frac{\Delta R}{2} - \left|R^l(t) - R_\mu\right|\right)\Theta\left(\frac{\Delta P}{2} - \left|P^l(t) - P_\eta\right|\right)\sigma^l_{ij} \tag{2.22}$$

where $\Theta(x)$ is the Heaviside step function. The impurity is then

$$S(t) = 1 - 2\pi\hbar \sum_{\mu,\eta} \left(A_{11}(R_\mu, P_\eta, t)^2 + 2\left|A_{12}(R_\mu, P_\eta, t)\right|^2 + A_{22}(R_\mu, P_\eta, t)^2\right)\Delta R \Delta P \tag{2.23}$$

Unfortunately, this procedure can be sensitive to the choice of grid size. On the

one hand, if ΔR and ΔP are too large, the entire wavepacket can be averaged into one big bin so one does not recover the continuous integral in Eq. (2.20). On the other hand, if ΔR and ΔP are too small and we do not have enough trajectories, some bins will contain zero data points because of incomplete sampling, and our final distribution will appear scattered and distorted. We have done our best to converge our results to the correct impurity, using 40,000 trajectories.

2.4 Results

To test our approach above, we investigate two standard one-dimensional problems from Tully's original paper[13], the simple avoided crossing and the problem of extended coupling. The adiabatic PESs of the two problems are shown in Fig. 2.1. We study two different variations of surface hopping: 1. Tully's original fewest-switches surface hopping (FSSH) and 2. our group's decoherence-improved augmented fewest switches surface hopping (A-FSSH) algorithm[39,40]. The A-FSSH algorithm was designed to build collapsing events on top of FSSH dynamics in order to better simulate wavepacket separation and decoherence from the perspective of the electronic subsystem following the pioneering work of Prezhdo[26], Rossky[24,25,32,33], Hammes-Schiffer[28], Truhlar[29–31,34–36] and Schwartz[92,93]. In other words, A-FSSH was designed to better estimate the reduced electronic density matrix

$$\boldsymbol{\sigma}_e(t) = \iint d\vec{R} d\vec{P} \mathbf{A}(\vec{R}, \vec{P}, t) = \begin{pmatrix} \sigma_{11}(t) & \sigma_{12}(t) \\ \sigma_{21}(t) & \sigma_{22}(t) \end{pmatrix} \tag{2.24}$$

with corresponding electronic impurity

$$S_e(t) = 1 - \mathrm{Tr}_e \left(\boldsymbol{\sigma}_e^2(t) \right) \tag{2.25}$$

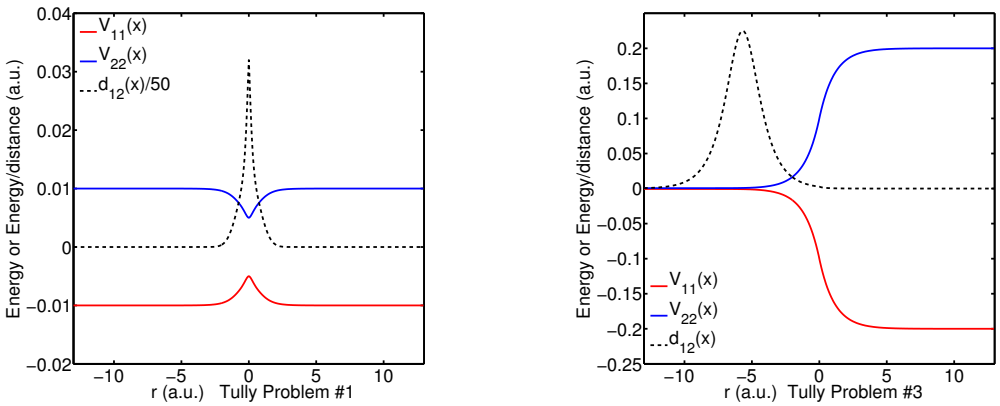

Figure 2.1: The adiabatic PESs for the two standard one-dimensional problems in Tully's original paper[13].

assuming that nuclear wavepackets on different surfaces separate irreversibly.

At time zero, we prepare a Gaussian wavepacket far to the left ($x = -15$ a.u.) of the scattering region, starting off on the lower adiabatic PES with width $\sigma = 1$ and a momentum of positive 20 a.u.. The particle mass is 2000 a.u.. We transform to the Wigner representation in phase space to initialize a swarm of surface hopping trajectories. At a set of different times, we take snapshots of the swarm of trajectories, digest the corresponding trajectory information into the phase-space grids discussed above, and then compute the impurity. For reasons of intuition, we also plot the partial Wigner distribution in phase space for two separate times: (i) right after a wavepacket is spawned and the wavepackets are still close to the coupling region, and (ii) at long times, when the wavepackets are already far removed from the coupling region.

2.4.1 Tully Problem #1: Avoided Crossing

For Tully Problem #1, the electronic Hamiltonian in a diabatic basis is[13]:

$$\begin{aligned} V_{11}(x) &= A[1-\exp(-Bx)], x>0 \\ V_{11}(x) &= -A[1-\exp(Bx)], x<0 \\ V_{22}(x) &= -V_{11}(x) \\ V_{12}(x) &= V_{21}(x) = C\exp(-Dx^2) \end{aligned} \tag{2.26}$$

where $A = 0.01, B = 1.6, C = 0.005$, and $D = 1.0$, all in atomic units. See Fig. 2.1 for a picture.

For this problem, the dynamics are simple: a wavepacket enters the coupling region on the lower adiabat and spawns a new wavefunction on the upper adiabat. Eventually, two wavepackets emerge from the coupling region – both propagating forward (in the positive x direction).

In Figs. 2.2-2.5, we plot the elements of the partially Wigner transformed density matrix for surface hopping calculations versus exact quantum dynamics. Here, we use FSSH surface hopping dynamics; note that A-FSSH and FSSH are almost identical here. The data are plotted at short and long times after the crossing event.

From the data, we see that the FSSH and exact results for the populations A_{11}^W and A_{22}^W agree quite well at all times. However, the FSSH algorithm only partially recovers the correct form for A_{12}^W. Whereas exact quantum dynamics predicts only two peaks (one positive, the other negative) for the coherence, FSSH predicts multiple peaks that are correlated with the diagonal peaks. The agreement gets worse for long times. According to exact quantum dynamics, there are also small oscillations in phase for the off-diagonal matrix elements that are absent for FSSH dynamics. These

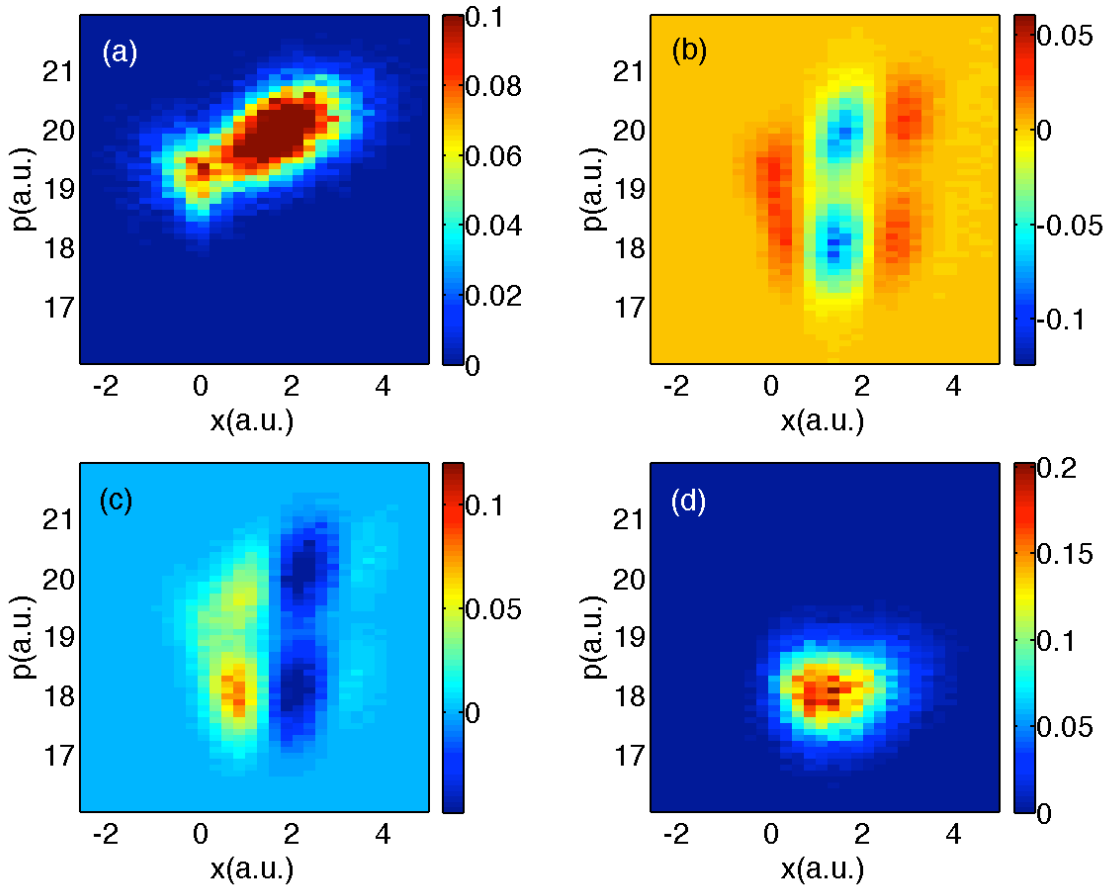

Figure 2.2: FSSH data for Tully #1. The densities are plotted in phase space at time 1590 a.u., (a) top-left A_{11}; (b) top-right Re(A_{12}); (c) bottom-left Im(A_{12}); and (d) bottom-right A_{22}.

observations will be explained in detail.

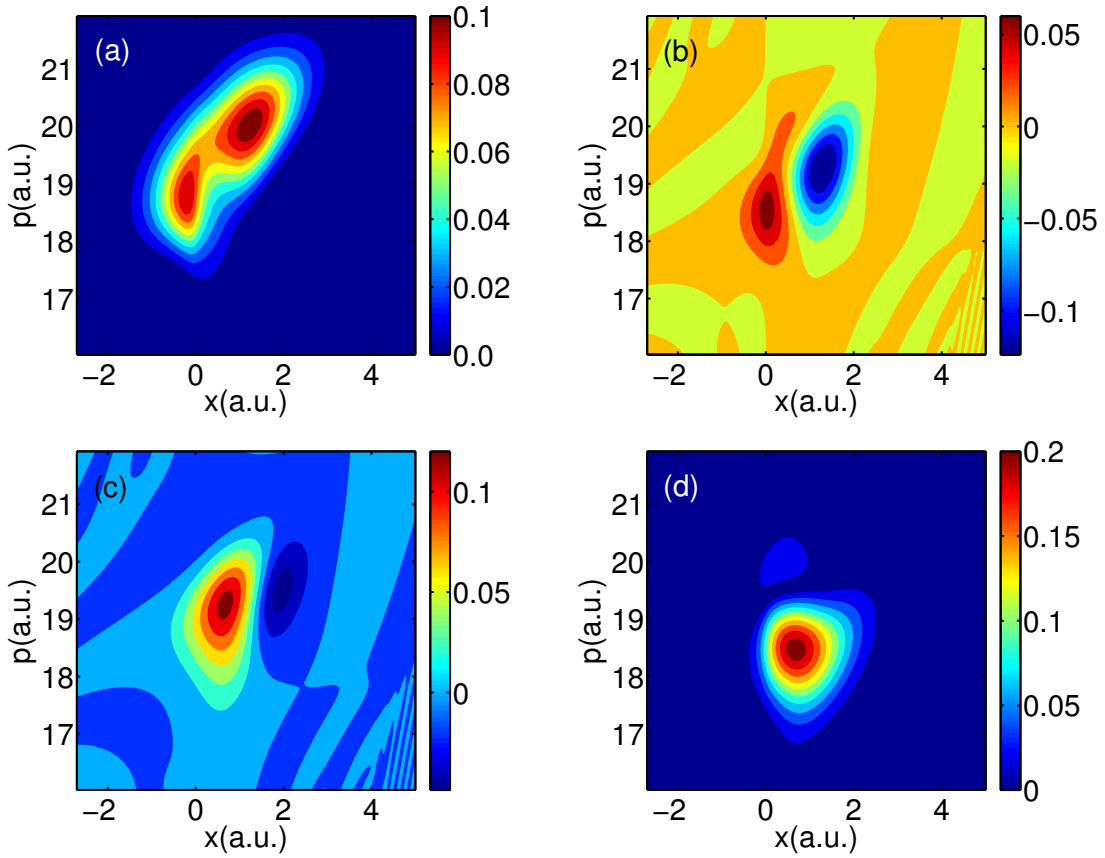

Figure 2.3: Exact quantum dynamics for Tully #1: Time is 1590 a.u.. Same notation as in Fig. 2.2. Note that FSSH data and exact data agree qualitatively for populations but not for coherences.

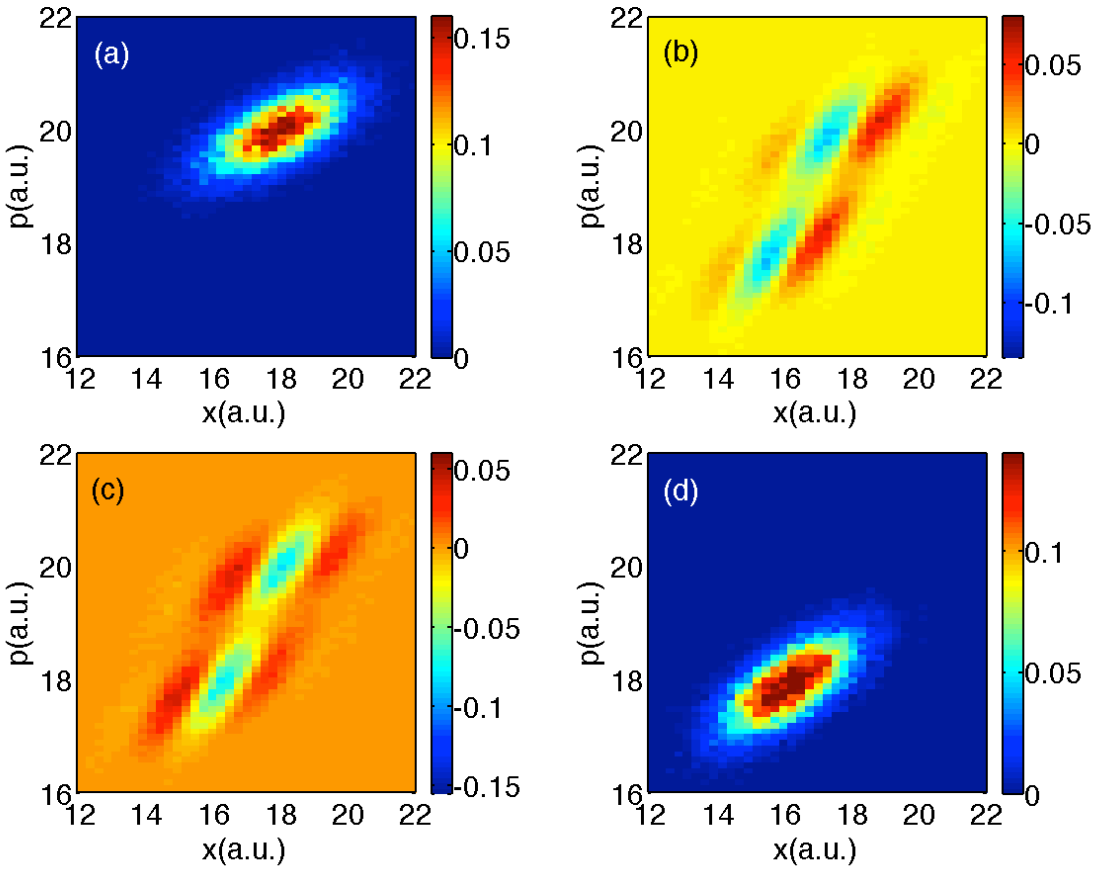

Figure 2.4: FSSH data for Tully #1: Time is 3300 a.u.. Same notation as in Fig. 2.2.

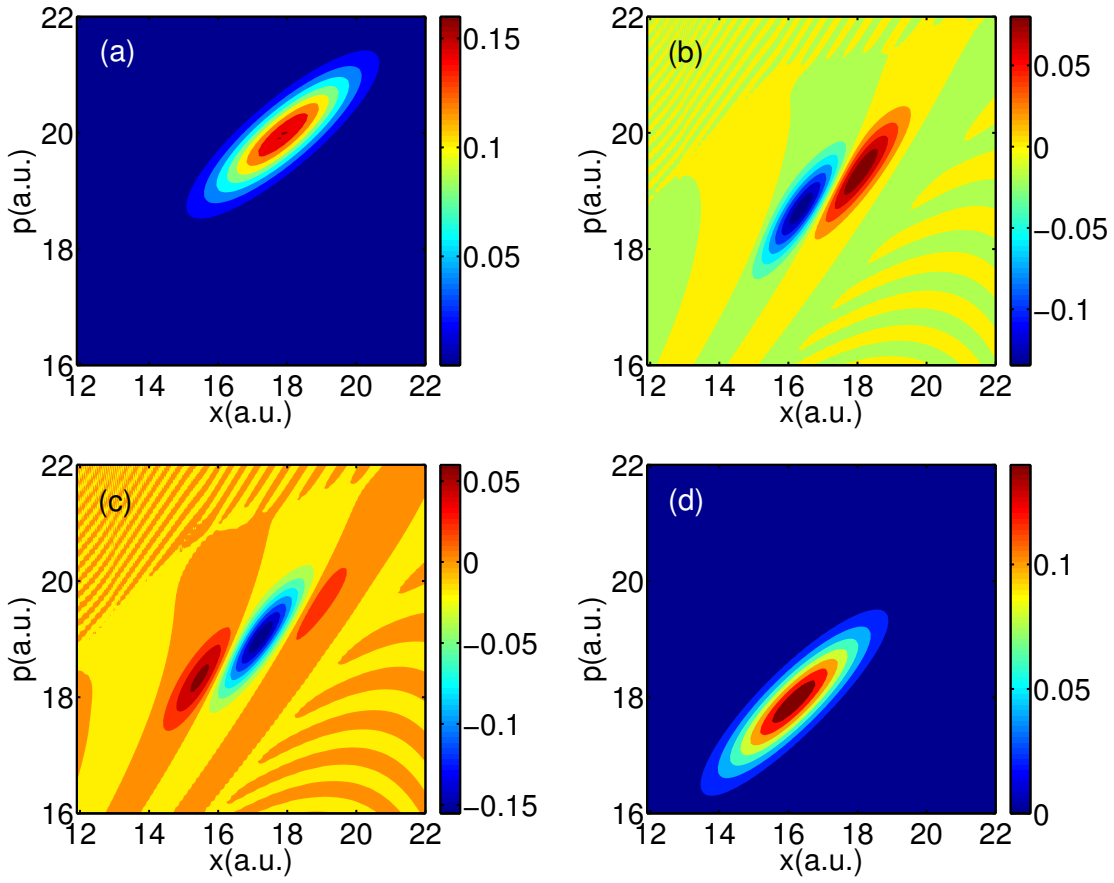

Figure 2.5: Exact quantum dynamics for Tully #1: Time is 3300 a.u.. Same notation as in Fig. 2.2. Note that FSSH data and exact data agree qualitatively for populations but not for coherences.

2.4.2 Tully Problem #3: Extended Couplings

For Tully problem #3, the electronic Hamiltonian in a diabatic basis is[13]:

$$\begin{aligned} V_{11}(x) &= -A \\ V_{22}(x) &= A \\ V_{12}(x) &= B\exp(Cx), x < 0 \\ V_{12}(x) &= B[2 - \exp(-Cx)], x > 0 \end{aligned} \tag{2.27}$$

where $A = 0.0006, B = 0.1$ and $C = 0.9$, all in atomic units. See Fig. 2.1 for a picture.

For this model Hamiltonian, the dynamics are more complicated than the previous problem. Here, one wavepacket begins far to the left on the lower adiabat and, moving to the right, a second wavepacket is spawned on the upper adiabat. Afterwards, the two wavepackets continue moving right and leave the coupling region. At time 1650 a.u., the wavepacket on the lower adiabat is moving quickly to the right and eventually it will transmit with nearly 100% probability. At the same time, the wavepacket on the upper adiabat has slowed down and is in the process of turning around; this wavepacket will reflect with nearly 100% probability. Later on, before time $t = 3300$ a.u., the reflecting wavepacket on the upper adiabat will spawn another wavepacket on the lower adiabat, and both of these wavepackets will then move together to the left asymptotically.

In Figs. 2.6-2.8, we plot results for A-FSSH, FSSH and exact quantum dynamics at time 1650 a.u., not long after the spawning event. Note that the population data from FSSH and A-FSSH track the exact quantum dynamics data nearly quantitatively. However, at the same time, we see that the off-diagonal matrix elements could not be more different. In particular, according to exact quantum dynamics, the A_{12}^W

coherence matrix element is centered midway between the A^W_{11} and A^W_{22} population matrix elements. By contrast, FSSH predicts that the coherences should be centered on the population peak positions (just as for Tully problem #1). At the same time, because of a collapsing event triggered by wavepacket separation, A-FSSH predicts almost exactly zero coherence.

Finally, for long times (t = 3300 a.u.), we plot all data in Figs. 2.9-2.11. Focusing first on populations, exact quantum dynamics reveals a small peak in between the two centers of populations around $(x, p) \approx (5, 5)$; this feature is absent from the surface hopping data and will be explained in Section 2.5.1. Otherwise, the surface hopping data looks qualitatively correct.

With regards to the coherences in Figs. 2.9-2.11, exact quantum dynamics predicts that the off-diagonal matrix element is incredibly small except for a small peak midway between the two population centers at $(x, p) \approx (5, 5)$ and phase oscillations are observed around that peak. Neither A-FSSH nor FSSH find such a peak nor such oscillations; these features will also be explained below.

Interestingly, notice that, if one looks at A_{12} in Fig. 2.9 around the transmitting peak at $(x, p) = (30, 45)$, the FSSH decoherence problem is barely visible. In fact, the FSSH coherence density appears almost as small as the A-FSSH coherence density, even though we know that, for this specific problem, the FSSH methodology breaks down[26,92]; unlike A-FSSH, the FSSH algorithm fails to account for the bifurcation between transmitting and reflecting wavefunctions. To explain this surprising feature, recall that, for these figures, we are averaging over finite chunks of phase space; as we have explained in Ref. 94, Tully problem #3 is pathological because, by chance, averaging removes FSSH's decoherence problems. To prove that the FSSH coherences are actually large and that the data scale in Fig. 2.9 is small only by a fortuitous

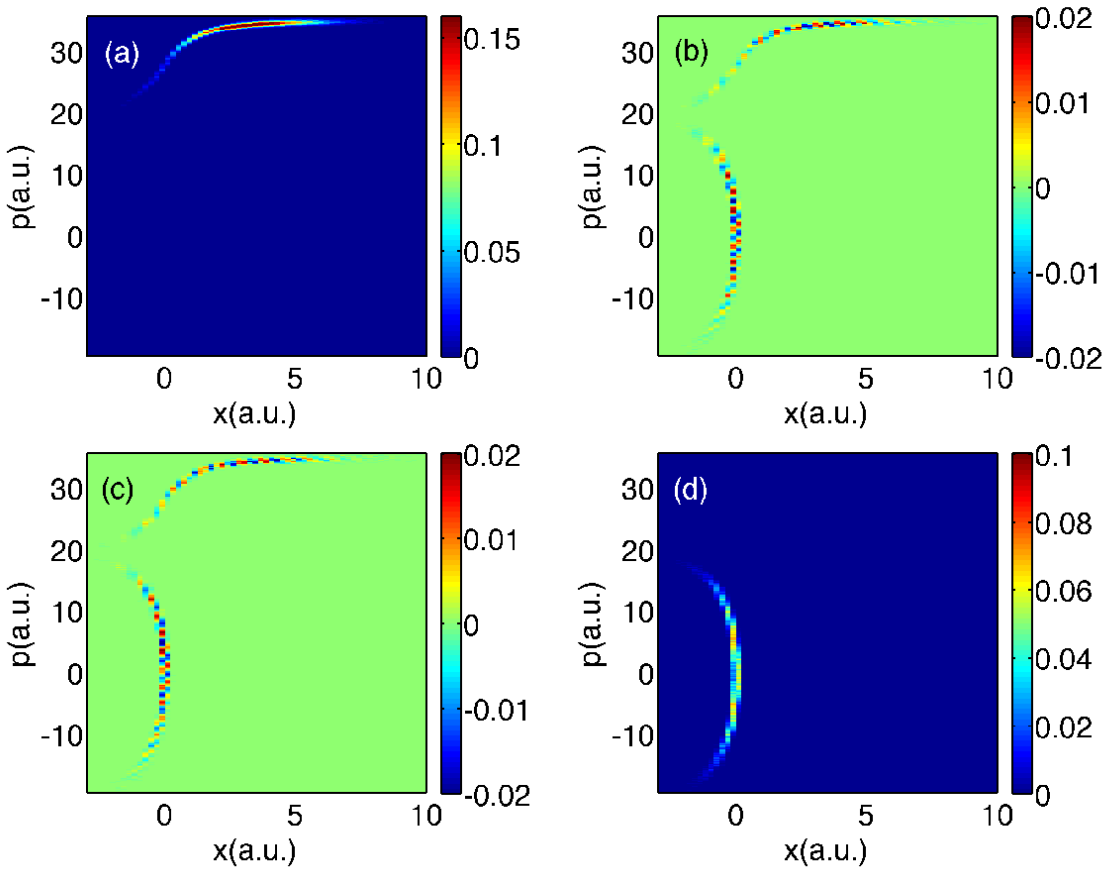

Figure 2.6: FSSH data for Tully #3: Time is 1650 a.u.. Same notation as in Fig. 2.2.

cancellation of sign, in Fig. 2.12 we plot the function:

$$A_{12}^{norm}(R,P,t) \equiv \frac{1}{N_s}\sum_l \delta(R-R^l(t))\delta(P-P^l(t))\left|\sigma_{ij}^l\right| \tag{2.28}$$

From Fig. 2.12, it is clear that each FSSH trajectory carries an electronic density matrix with a large off-diagonal component, and the FSSH algorithm does well only because averaging over a phase space volume allows for a fortuitous sign cancellation[94].

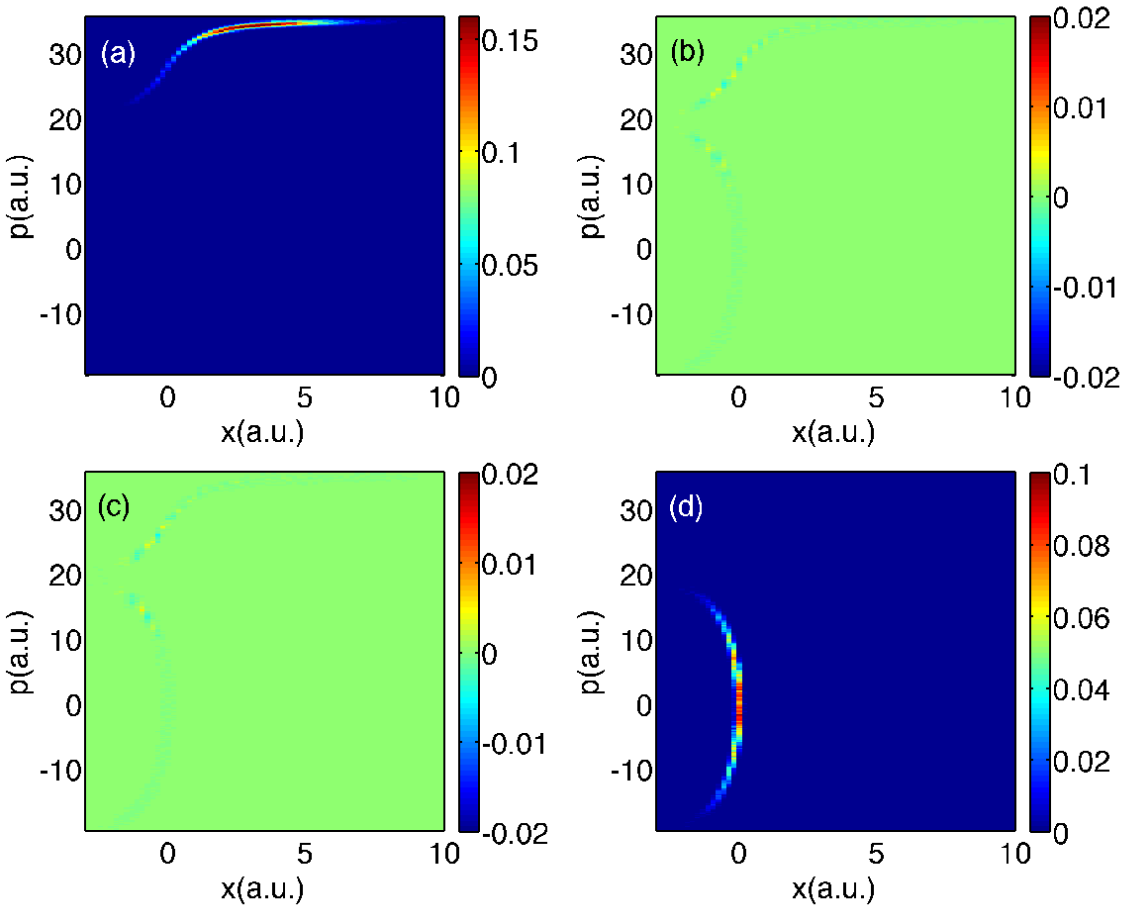

Figure 2.7: A-FSSH data for Tully #3: Time is 1650 a.u.. Same notation as in Fig. 2.2.

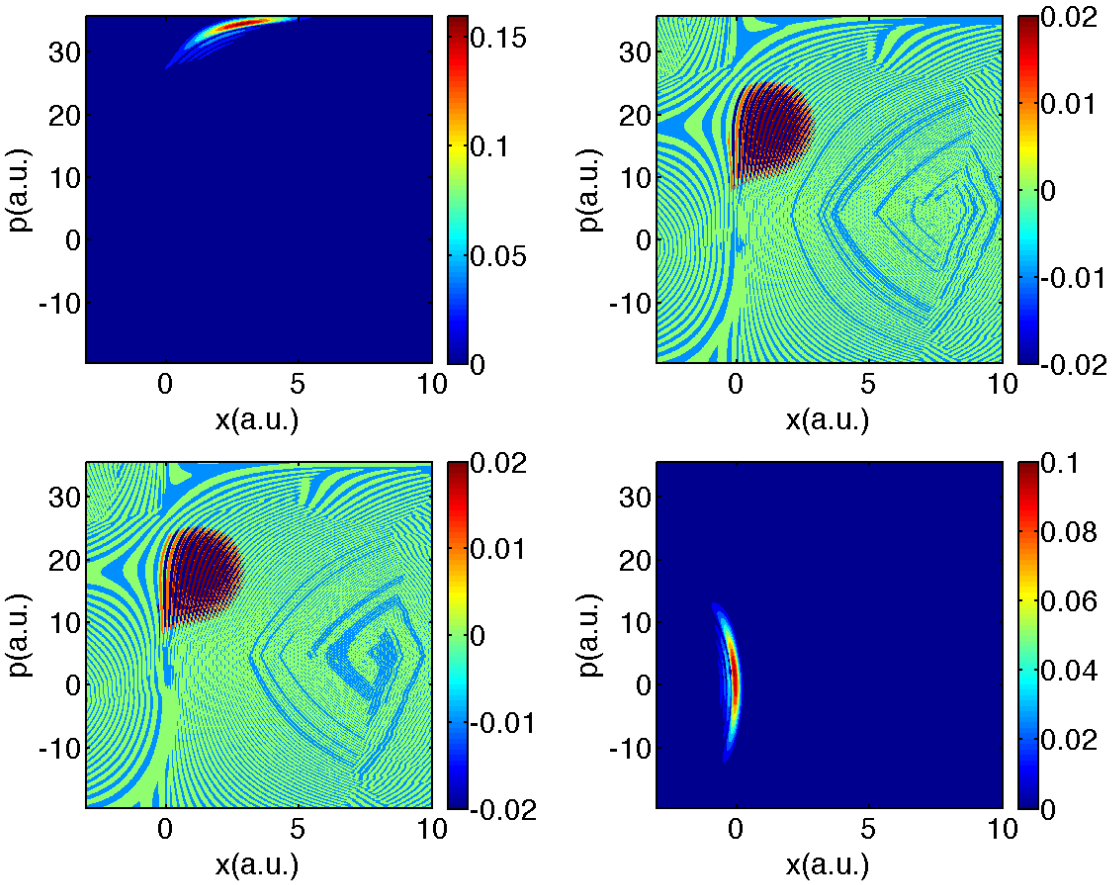

Figure 2.8: Exact quantum dynamics data for Tully #3: Time is 1650 a.u.. Same notation as in Fig. 2.2.

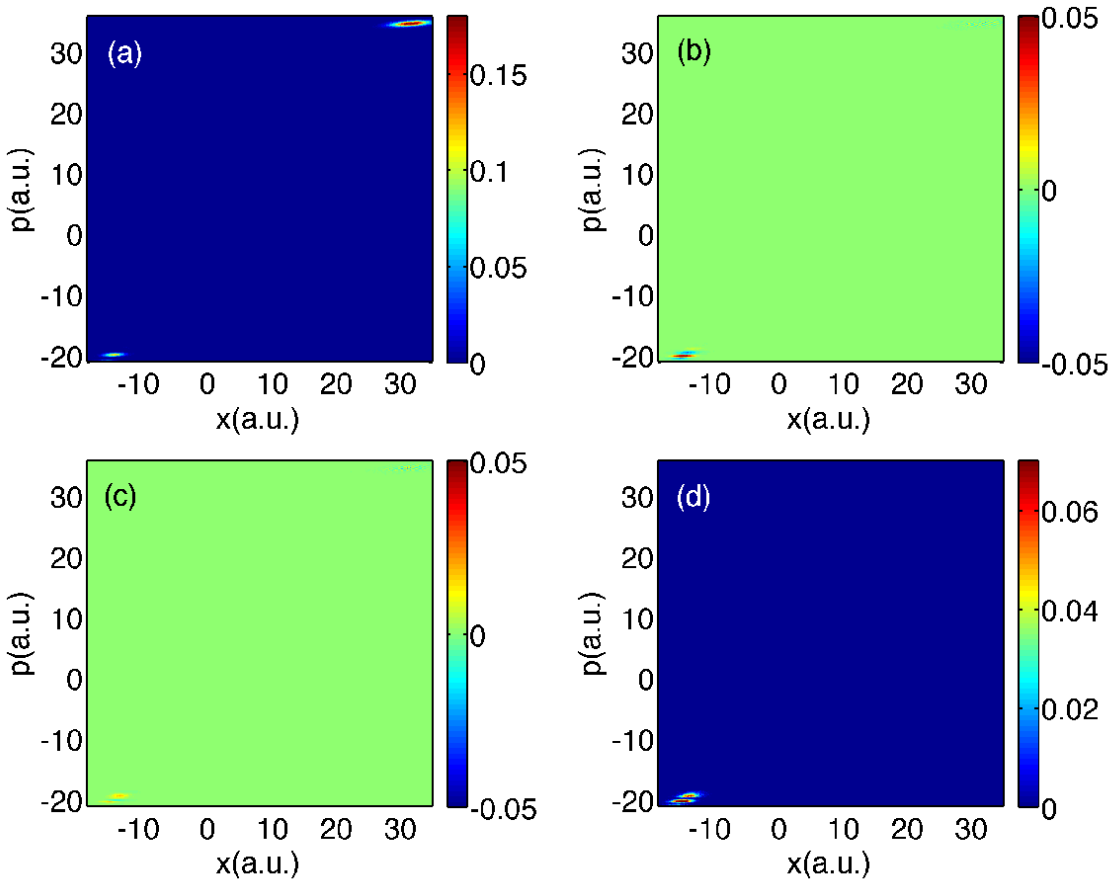

Figure 2.9: FSSH data for Tully #3: Time is 3300 a.u.. Same notation as in Fig. 2.2.

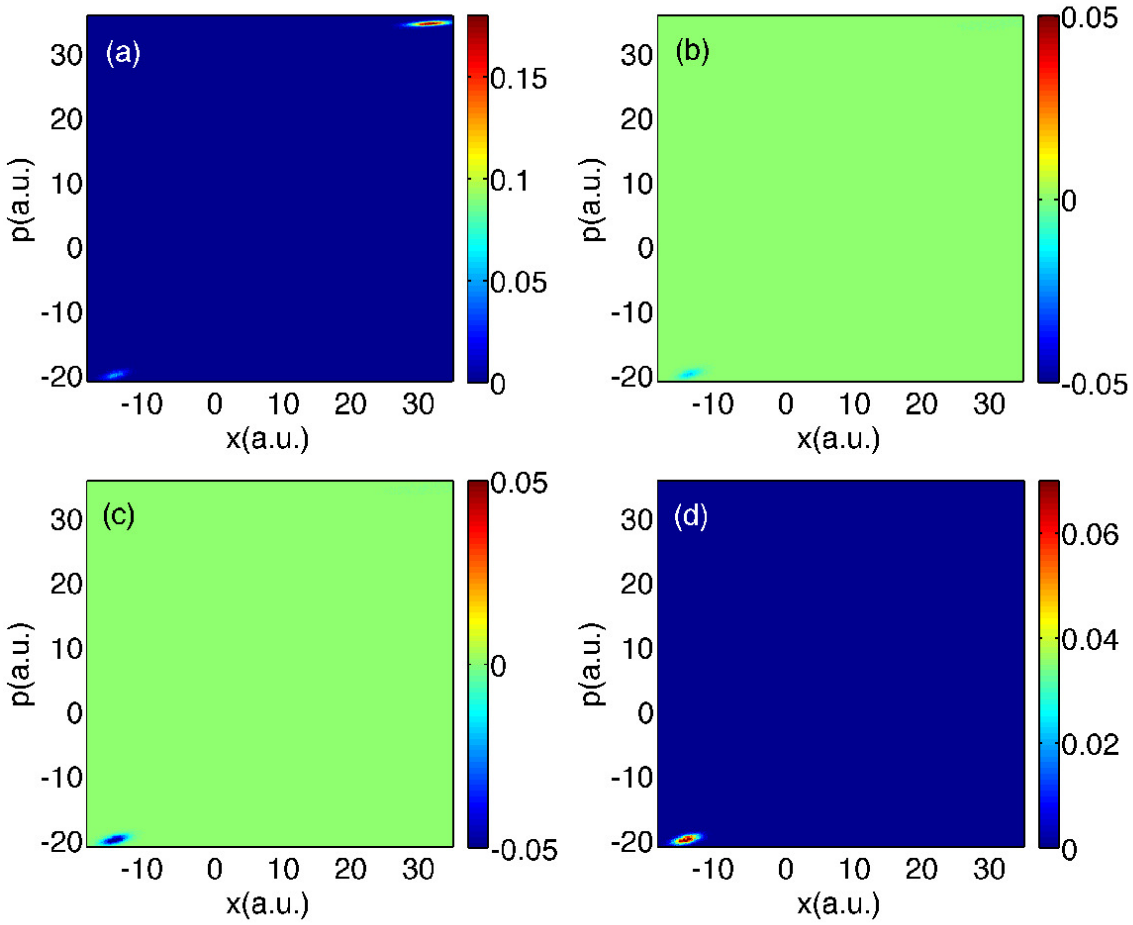

Figure 2.10: A-FSSH data for Tully #3: Time is 3300 a.u.. Same notation as in Fig. 2.2.

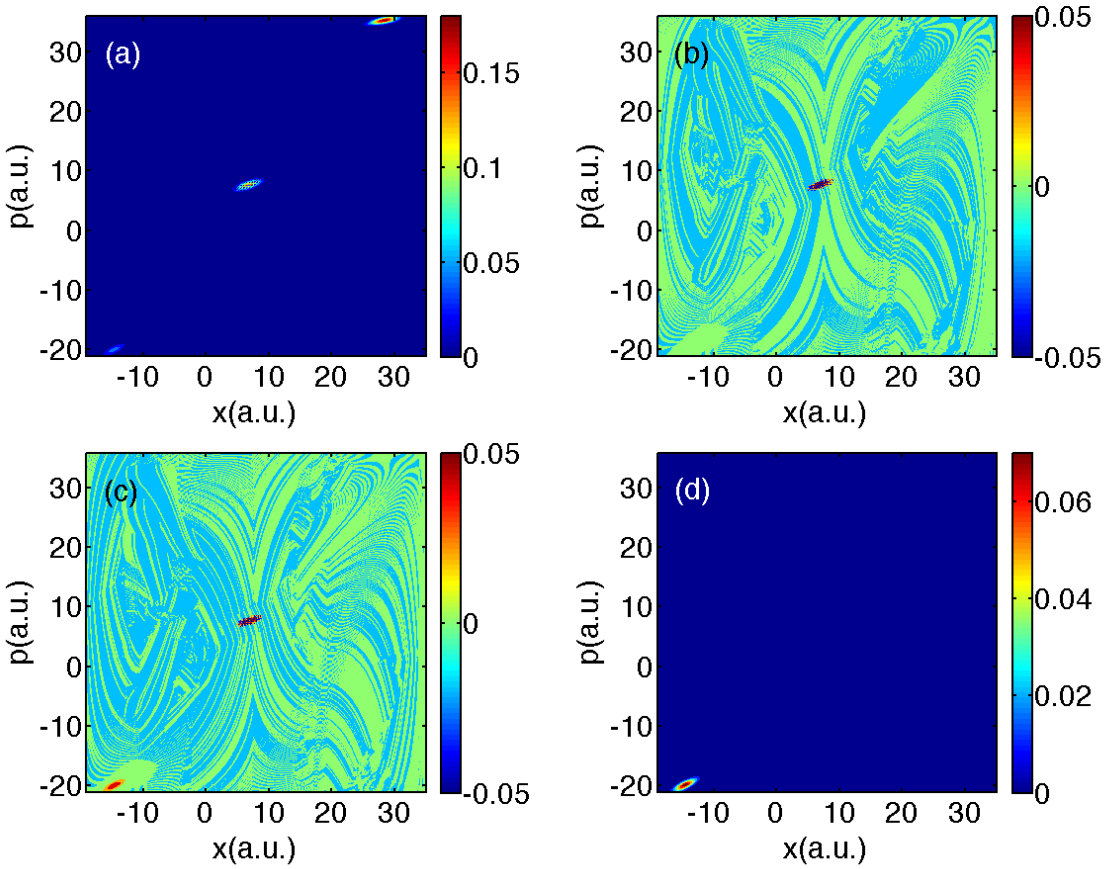

Figure 2.11: Exact quantum dynamics data for Tully #3: Time is 3300 a.u.. Same notation as in Fig. 2.2.

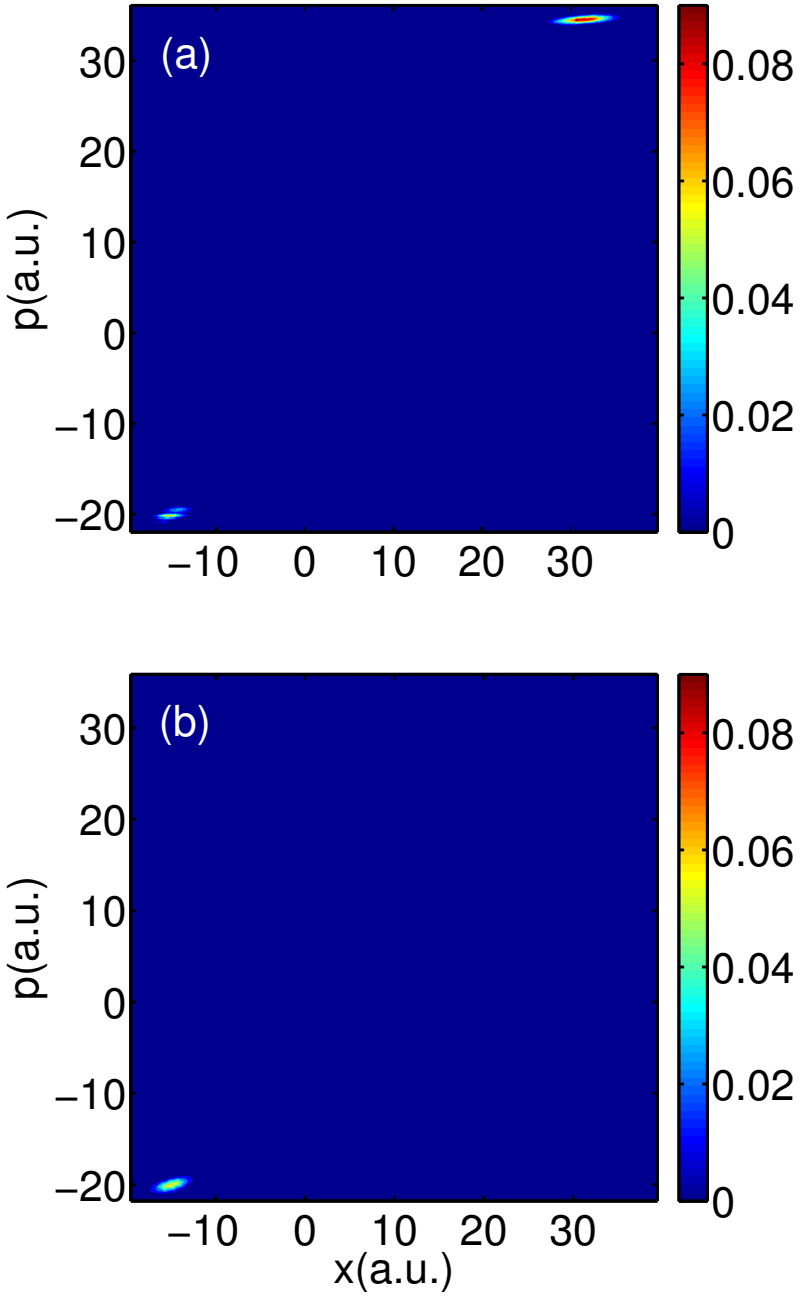

Figure 2.12: FSSH and A-FSSH data for Tully #3. Here, we evaluated the absolute value of the coherence, i.e. Eq. (2.28) and time is 3300 a.u.. (a) FSSH and (b) A-FSSH.

2.4.3 Impurity

Having analyzed the capacity of surface hopping methods to recover the partial Wigner transform densities in phase space, in Fig. 2.13 we plot the total impurity ($S(t)$, Eq. (2.20)) as function of time both for FSSH and A-FSSH trajectories. Here, ΔR and ΔP are chosen by insisting that the total impurity be zero at time zero, and we have checked that our data are changed only slightly by altering the grid sizes.

According to Fig. 2.13, we find that the total impurity grows in time for both FSSH and A-FSSH as soon as particles start hopping in between surfaces. As we will show in Section 2.5.2, one can evaluate this growth in total impurity analytically for simple problems (e.g., for Tully #1). From the data in Sections 2.4.1 and 2.4.2, it is clear that this growth in total impurity can be attributed to the off-diagonal errors of FSSH.

Interestingly, according to Fig. 2.13, even though A-FSSH incorporates decoherence, FSSH and A-FSSH yield very similar total impurities. This coincidence can be explained by the simple fact that neither algorithm captures the exact coherence and neither can correctly recover recoherences. The premise of the A-FSSH algorithm is that, since recoherences cannot be captured correctly by any Tully-style surface hopping algorithm, one should damp the electronic coherences after wavepackets separate so that long time dynamics (without recoherences) will be stable and accurate[95]. In other words, A-FSSH was designed to recover the correct impurity of the electronic subsystem (which is entangled with the nuclei).

To prove that A-FSSH delivers on this promise, we plot the elements of reduced electronic density matrix and electronic impurity ($S_e(t)$, Eq. (2.25)) in Figs. 2.14-2.15. From the figures, we observe that A-FSSH recovers qualitatively the exact reduced electronic density matrix for Tully problem #1 and quantitatively the exact reduced

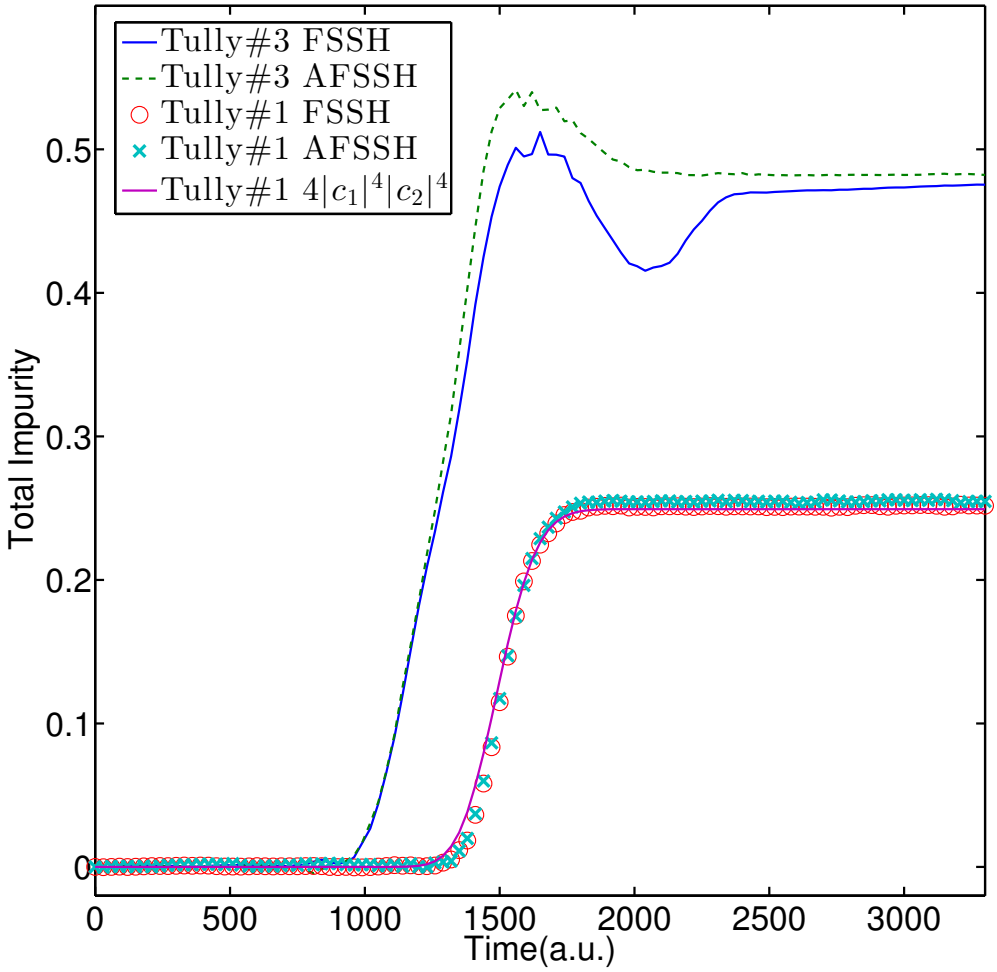

Figure 2.13: The total impurity S(t) from Eq. (2.20) for the FSSH and A-FSSH algorithms for Tully problems #1 and #3. We also plot Eq. (2.42), an approximate analytical result for frozen Gaussians. The total impurity of the exact quantum system is zero for all time.

electronic density matrix for Tully problem #3. Moreover, in both cases, A-FSSH exactly reproduces the impurity of the electronic subsystem (which grows in time as would be expected). Note that FSSH recovers neither the correct reduced electronic density matrix nor the electronic impurity for Tully problem #3.

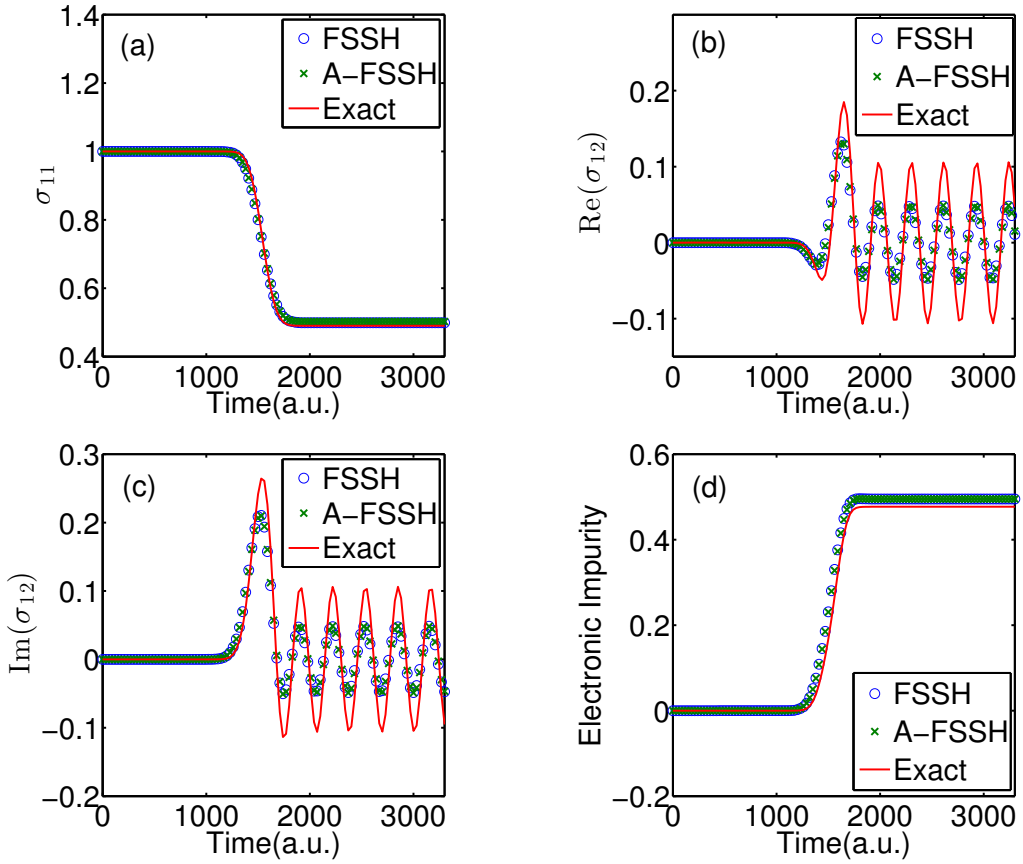

Figure 2.14: The reduced electronic density matrix for Tully problem #1 according to exact quantum dynamics, FSSH, and A-FSSH. (a) σ_{11}; (b) $\mathrm{Re}(\sigma_{12})$; (c) $\mathrm{Im}(\sigma_{12})$; (d) the electronic impurity $S_e(t)$ (Eq. (2.25)). (a), (b), (c) are expressed in the diabatic basis. Note that the electronic impurity increases, and both FSSH and A-FSSH recover the correct electronic impurity.

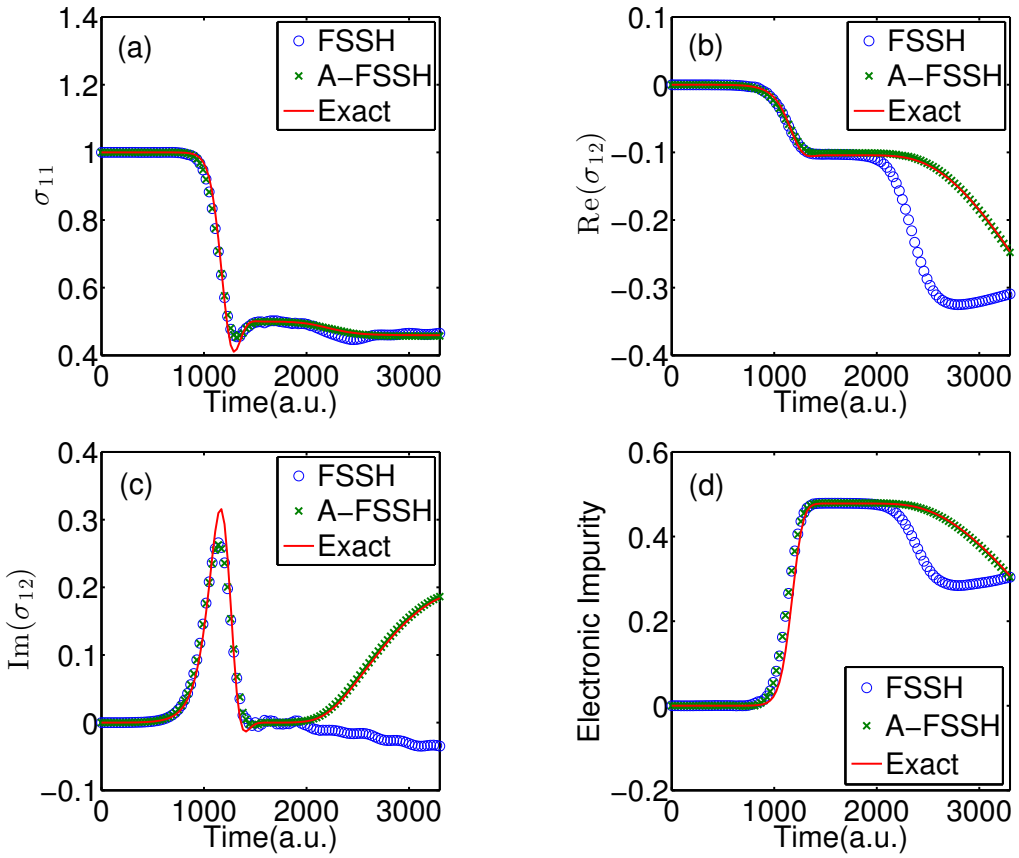

Figure 2.15: The reduced electronic density matrix for Tully problem #3 according to exact quantum dynamics, FSSH, and A-FSSH. (a) σ_{11}; (b) $\mathrm{Re}(\sigma_{12})$; (c) $\mathrm{Im}(\sigma_{12})$; (d) the electronic impurity $S_e(t)$ (Eq. (2.25)). (a), (b), (c) are expressed in the diabatic basis. Note that only A-FSSH recovers the correct electronic impurity.

2.5 Discussion: Frozen Gaussian Dynamics in a Partially Transformed Wigner Phase Space

2.5.1 Exact Quantum Dynamics Predicts Nonlocal Coherences and Phase Oscillations

The data in Sections 2.4.1 and 2.4.2 highlighted the fact the surface hopping dynamics can recover the populations well (compared to the exact partial Wigner transform), but off-diagonal coherences are not as accurate. These results should not be very surprising to a reader familiar with Ref. 20, where it was shown that (*i*) the on-diagonal equations of motion for FSSH are almost exactly the same as the corresponding QCLE equations of motion; but (*ii*) the off-diagonal equations of motion for FSSH need a severe correction to approximate the corresponding QCLE equations of motion. And formally, these corrections require interacting (rather than independent) trajectories. In the present manuscript, we have seen that the FSSH errors in off-diagonal coherence lead effectively to a growth in total impurity over time.

To better interpret our data from Sections 2.4.1 and 2.4.2, we will now find it useful to investigate wavepacket bifurcation in phase space from the perspective of frozen Gaussian nonadiabatic dynamics. With a frozen Gaussian ansatz, the total nuclear-electronic wavefunction has the following form[20]:

$$\Psi(\vec{r},\vec{R},t) = c_1 g(\vec{R};\vec{R}_1(t),\vec{P}_1(t))\Phi_1(\vec{r};\vec{R}) + c_2 g(\vec{R};\vec{R}_2(t),\vec{P}_2(t))\Phi_2(\vec{r};\vec{R}) \tag{2.29}$$

where g represents a nuclear Gaussian wavepacket

$$\begin{aligned} g(\vec{R};\vec{R}_s(t),\vec{P}_s(t)) \;\equiv\; & \prod_\alpha \left(\frac{1}{\pi a_{R^\alpha}^2}\right)^{1/4} \exp\left(\frac{-(R^\alpha - R_s^\alpha(t))^2}{2a_{R^\alpha}^2}\right) \\ & \times \exp\left(\frac{i}{\hbar} P_s^\alpha(t)(R^\alpha - R_s^\alpha(t))\right) \end{aligned} \tag{2.30}$$

According to Eq. (2.7), the partial Wigner transform for a frozen Gaussian is (for $i = 1, 2$)

$$A_{11}^W(\vec{R}, \vec{P}) = \frac{|c_1|^2}{(\pi\hbar)^{3N}} \prod_\alpha \exp\left(\frac{-(R^\alpha - R_1^\alpha)^2}{a_{R^\alpha}^2}\right) \exp\left(\frac{-(P^\alpha - P_1^\alpha)^2 a_{R^\alpha}^2}{\hbar^2}\right) \tag{2.31}$$

$$A_{22}^W(\vec{R}, \vec{P}) = \frac{|c_2|^2}{(\pi\hbar)^{3N}} \prod_\alpha \exp\left(\frac{-(R^\alpha - R_2^\alpha)^2}{a_{R^\alpha}^2}\right) \exp\left(\frac{-(P^\alpha - P_2^\alpha)^2 a_{R^\alpha}^2}{\hbar^2}\right) \tag{2.32}$$

$$\begin{aligned} A_{12}^W(\vec{R}, \vec{P}) \;=\; & \frac{c_1 c_2^*}{(\pi\hbar)^{3N}} \prod_\alpha \exp\left(\frac{-(R^\alpha - \frac{1}{2}(R_1^\alpha + R_2^\alpha))^2}{a_{R^\alpha}^2}\right) \\ & \times \exp\left(\frac{-(P^\alpha - \frac{1}{2}(P_1^\alpha + P_2^\alpha))^2 a_{R^\alpha}^2}{\hbar^2}\right) \exp\left(\frac{i(R_2^\alpha - R_1^\alpha)P^\alpha}{\hbar}\right) \\ & \times \exp\left(\frac{i(P_1^\alpha - P_2^\alpha)R^\alpha}{\hbar}\right) \exp\left(\frac{i(P_2^\alpha - P_1^\alpha)(R_2^\alpha + R_1^\alpha)}{2\hbar}\right) \end{aligned} \tag{2.33}$$

By integrating the squares of Eqs. (2.31)-(2.32) and plugging into Eq. (2.20), it is straightforward to prove (as it must be) that the impurity of a frozen Gaussian ansatz is always zero, $S = 0$.

Two key observations emerge from Eqs. (2.31)-(2.33):

1. According to exact quantum dynamics, the off-diagonal coherence matrix element A_{12}^W should pick up a phase that oscillates very quickly throughout phase space, proportional to $(\vec{R}_1 - \vec{R}_2)$ and $(\vec{P}_1 - \vec{P}_2)$.

2. According to exact quantum dynamics, the off-diagonal coherence density in phase space is not centered at the same location as the on-diagonal population densities. In particular, the off-diagonal coherence density matrix is centered at $\big((\vec{R}_1 + \vec{R}_2)/2, (\vec{P}_1 + \vec{P}_2)/2\big)$.

These two observations (nonlocal coherences and phase oscillations) explain the qualitative features we saw for exact quantum dynamics data in Figs. 2.3, 2.5, 2.8 and

2.11. The nonlocality of the A_{12}^W density in phase space is also completely consistent with the QCLE which postulates that, to first order in $\hbar$, A_{12}^W coherences should be propagated with forces $(\vec{F}_1 + \vec{F}_2)/2$ [while the populations A_{11}^W (A_{22}^W) are propagated, of course, along $\vec{F}_1$ ($\vec{F}_2$)].

As a sidenote, we mention that, even for a wavefunction with two frozen Gaussians on *the same* electronic surface A_{11}^W – the first wavepacket centered at $(\vec{R}_1^{(a)}, \vec{P}_1^{(a)})$ and the second wavepacket centered at $(\vec{R}_1^{(b)}, \vec{P}_1^{(b)})$ – one still finds a nonlocal peak in the Wigner transform centered at $(\vec{R}_1^{(a)} + \vec{R}_1^{(b)})/2$ and $(\vec{P}_1^{(a)} + \vec{P}_1^{(b)})/2$. These nonlocal peaks are a well-known feature of Wigner transforms[96], and this explains the peak in the middle of Fig. 2.11(a).

Overall, partially Wigner transformed density matrices can produce complicated, nonlocal phase space densities.

2.5.2 FSSH Predicts Local Coherences: An Analytical Measure of FSSH Impurity

Let us now consider frozen Gaussian dynamics from the perspective of the FSSH and A-FSSH algorithms, and calculate our definition of impurity. To simplify the notation, we define $f_1(\vec{R}, \vec{P})$ and $f_2(\vec{R}, \vec{P})$ as the normalized nuclear densities in phase space for adiabats 1 and 2 (for $i = 1, 2$):

$$f_i(\vec{R}, \vec{P}) = \frac{1}{(\pi\hbar)^{3N}} \prod_\alpha \exp\left(\frac{-(R^\alpha - R_i^\alpha)^2}{a_{R^\alpha}^2}\right) \exp\left(\frac{-(P^\alpha - P_i^\alpha)^2 a_{R^\alpha}^2}{\hbar^2}\right), \tag{2.34}$$

For the FSSH algorithm, the diagonal elements of the partially Wigner transformed density matrix are then (for $i = 1, 2$)

$$A_{ii}(\vec{R}, \vec{P}) = |c_i|^2 \, f_i(\vec{R}, \vec{P}) \tag{2.35}$$

and it is easy to show that (for $i = 1, 2$)

$$\int_{-\infty}^{\infty} d\vec{R} \int_{-\infty}^{\infty} d\vec{P} f_i(\vec{R}, \vec{P}) = 1 \tag{2.36a}$$

$$\int_{-\infty}^{\infty} d\vec{R} \int_{-\infty}^{\infty} d\vec{P} f_i(\vec{R}, \vec{P})^2 = \frac{1}{(2\pi\hbar)^{3N}} \tag{2.36b}$$

Hence, one can calculate that (for $i = 1, 2$)

$$\int d\vec{R} \int d\vec{P} A_{ii}(\vec{R}, \vec{P})^2 = \frac{1}{(2\pi\hbar)^{3N}} |c_i|^4 = \int_{-\infty}^{\infty} d\vec{R} \int_{-\infty}^{\infty} d\vec{P} A_{ii}^W(\vec{R}, \vec{P})^2 \tag{2.37}$$

In order to measure the impurity of a FSSH or A-FSSH calculation, we must also compute

$$\int d\vec{R} \int d\vec{P} \left| A_{12}(\vec{R}, \vec{P}) \right|^2 \tag{2.38}$$

Now, as discussed in Ref. 73, there are several possible definitions for the off-diagonal matrix element within the FSSH algorithm and these definitions will not agree exactly using FSSH-like independent trajectories. Nevertheless, that being said, we will focus here on the definition in Eq. (2.19) for A_{12}, which we have found to be the most numerically stable formula available[73]. (For the other possible definitions of the off-diagonal matrix element discussed in Ref. 73, one must divide by a diagonal matrix element σ_{ii}; thus, in cases where σ_{ii} gets small, one can potentially find a divergence of A_{12}.)

For a FSSH calculation with a frozen Gaussian ansatz, assuming each trajectory has consistent electronic amplitudes (c_1, c_2), we will find (according to Eq. (2.19)) that

$$A_{12} = c_1 c_2^* (|c_1|^2 f_1 + |c_2|^2 f_2) \tag{2.39}$$

Notice that, according to Eq. (2.39), A_{12} has two peaks (one around the population

on adiabat 1, one around the population on adiabat 2). This observation of two peaks agrees with our numerical results in Figs. 2.2, 2.4, 2.6 and 2.9, but this finding is in direct disagreement with the exact quantum answer. According to exact quantum dynamics, Eq. (2.33), A_{12}^W has only one peak centered in between the wavepackets on surfaces 1 and 2.

The disagreement between exact and FSSH-like methods for measuring coherences is a general failure of surface hopping: *Because the entire premise behind surface hopping is to build up both population and coherence phase space densities by following dynamics moving along adiabats, FSSH-like methods will never be able to fully capture nonlocal off-diagonal coherence densities centered far away from population densities.*

Finally, to estimate the resulting FSSH impurity, we compute the integral of the square of the FSSH coherence as

$$\begin{aligned}\int d\vec{R} \int d\vec{P} |A_{12}(\vec{R},\vec{P})|^2 &= \int d\vec{R} \int d\vec{P} \, |c_1|^2 \, |c_2|^2 \\ &\quad \times \left(|c_1|^4 \, f_1^2 + |c_2|^4 \, f_2^2 + 2 \, |c_1|^2 \, |c_2|^2 \, f_1 f_2 \right) \\ &= \frac{|c_1|^2 \, |c_2|^2}{(2\pi\hbar)^{3N}} \left(|c_1|^4 + |c_2|^4 \right) \\ &\quad + 2 \, |c_1|^4 \, |c_2|^4 \int d\vec{R} \int d\vec{P} f_1 f_2 \end{aligned} \tag{2.40}$$

which does not agree with

$$\int_{-\infty}^{\infty} d\vec{R} \int_{-\infty}^{\infty} d\vec{P} \left| A_{12}^W(\vec{R},\vec{P}) \right|^2 = \frac{1}{(2\pi\hbar)^{3N}} \, |c_1|^2 \, |c_2|^2 \tag{2.41}$$

If one assumes that the A_{11} and A_{22} densities are centered far away from each other and not overlapping, then the last term vanishes in Eq. (2.40). Substituting

Eqs. (2.37) and (2.40) into Eq. (2.20), we find

$$\begin{aligned} S &= 1 - \left[|c_1|^4 + |c_2|^4 + 2\,|c_1|^2\,|c_2|^2\,(|c_1|^4 + |c_2|^4) \right] \\ &= 1 - \left(|c_1|^4 + |c_2|^4 \right) \left(1 + 2\,|c_1|^2\,|c_2|^2 \right) \\ &= 1 - \left(\left(|c_1|^2 + |c_2|^2 \right)^2 - 2\,|c_1|^2\,|c_2|^2 \right) \left(1 + 2\,|c_1|^2\,|c_2|^2 \right) \\ &= 1 - \left(1 - 2\,|c_1|^2\,|c_2|^2 \right) \left(1 + 2\,|c_1|^2\,|c_2|^2 \right) \\ &= 4\,|c_1|^4\,|c_2|^4 \end{aligned} \tag{2.42}$$

Eq. (2.42) gives us an analytical result for evaluating the total impurity of a surface-hopping calculation provided the wavefunction can be approximated as a sum of simple frozen Gaussians. The total impurity of a FSSH calculation becomes positive as soon as there is population on more than one adiabatic electronic surface.

In practice, to evaluate Eq. (2.42), the simplest approach is to calculate $4\,|c_1|^4\,|c_2|^4$ for each trajectory and then average the result over all FSSH trajectories. According to Fig. 2.13, we find that Eq. (2.42) does agree with the numerically calculated impurity for Tully #1 (which can indeed be viewed as a simple model problem with two frozen Gaussians). Tully #3 is a more complicated model Hamiltonian – with more than two frozen Gaussians – and Eq. (2.42) cannot be applied naively.

2.5.3 The Efficiency of FSSH Comes at the Expense of Ignoring Recoherences and Not Conserving Impurity

Our discussion above of the frozen Gaussian model leads to a new understanding of the simultaneous limitations and strengths underlying all FSSH-like algorithms. On the one hand, these surface-hopping methods cannot treat correctly electronic coherences that are nonlocal in phase space and, therefore, these methods cannot correctly describe recoherences. Furthermore, the inability to capture recoherences

leads to an increasing value of total impurity for all FSSH-like calculations, whereas in truth total impurity must be conserved according to the exact dynamics of any closed system; impurity can grow only for an open quantum system. These are the failures of the surface hopping algorithm.

On the other hand, FSSH and A-FSSH are powerful tools for efficiently propagating nonadiabatic quantum dynamics in practice, and these methods can be derived approximately from the QCLE (assuming no recoherences). Furthermore, when measuring most expectation values, FSSH-like methods usually yield accurate observables because: (*i*) recoherences become increasingly uncommon for bigger and bigger systems at room temperature; (*ii*) when wavepackets are close together on different surfaces, surface hopping can capture the correct off-diagonal coherences; and (*iii*) when wavepackets move far apart on different surfaces, the correct off-diagonal matrix element picks up a rapidly oscillating phase that will integrate to zero in the stationary phase limit (Eq. (2.33)). Thus, even if FSSH-like methods cannot recover an electronic coherence that is stored nonlocally, for many expectation values, this failure will not be important. In practice, A-FSSH represents an improvement over FSSH dynamics by simply eliminating the spurious and incorrect FSSH coherences that arise when wavepackets bifurcate on different surfaces. In Figs. 2.14-2.15, we have shown that (unlike for FSSH) A-FSSH recovers the correct reduced electronic density matrix and electronic impurity (that grows in time).

The curious reader must surely ask him or herself whether another nonadiabatic dynamics algorithm exists that (*i*) offers the efficiency of the FSSH algorithm (which is easily simulated by standard Monte Carlo sampling) and also (*ii*) conserves the total impurity of the simulation exactly (by correctly describing all electronic coherences). Currently, many talented research groups are attacking this very problem in a myriad

of different ways[10–12,97–99].[1] Only time will tell if such an optimal method arises–and if not, what is the optimal compromise we should make when choosing an approximate nonadiabatic dynamics method?

2.6 Conclusions

In this paper, we have given a simple prescription (based on purity) for evaluating the total impurity of a system described by a partially Wigner transformed density matrix. We demonstrated that, according to our definition, exact quantum dynamics and the QCLE conserve the total impurity of a closed system in time, but that FSSH and FSSH-like methods do not conserve total impurity (For simple cases, we derived an analytic expression for the total impurity). We attributed this failure of surface-hopping methods to the inability of FSSH-like methods to recover the correct, nonlocal off-diagonal density matrix in phase space (or capture wavepacket recoherences). We noted, however, that in the limit of large separations between wavepackets on different surfaces, electronic coherences oscillate very quickly in phase space and should not contribute meaningfully to expectation values. Thus, we have argued that surface-hopping dynamics can make accurate predictions of observables in spite of the method's failure to conserve the total impurity of a closed system. Moreover, for the electronic subsystem, A-FSSH is able to deliver a reasonably accurate reduced density matrix and a very accurate electronic impurity (that grows in time correctly). Future work in nonadiabatic dynamics will no doubt explore how important total impurity conservation is when studying large (but closed) quantum systems designed to represent the condensed phase. After all, usually in chemistry we are interested in the impurity and dynamics of subsystems.

[1] Note that multiple spawning[10,11] has a wavefunction for the universe and thus conserves the universe's total impurity.

2.7 Acknowledgments

This material is based upon work supported by the (U.S.) Air Force Office of Scientific Research (USAFOSR) PECASE award under AFOSR Grant No. FA9550-13-1-0157. J.E.S. acknowledges an Alfred P. Sloan Research Fellowship and a David and Lucille Packard Fellowship. J.E.S. thanks Elaine Chandler for encouraging us to work on this problem, and Jeff Cina, Jeff Saven, David Chandler, and Seogjoo Jang for stimulating conversations.

CHAPTER 3

Surface Hopping with a Manifold of Electronic States I: Incorporating Surface-Leaking to Capture Lifetimes

This chapter is adapted from The Journal of Chemical Physics, Volume 142, Issue 8, Page 084109, 2015.

3.1 Introduction

Electronic dynamics usually come in two flavors. First, some electron relaxation events do not involve much coherence and can best be described probabilistically. In such cases, electrons are ejected into a continuum. Examples of such processes include chemi-ionization[41,100–104] and Auger recombination. Among chemi-ionization processes, Penning ionization has attracted much attention because of the large cross section in collisional reactions involving metastable atoms and molecules. As a result Penning ionization is an significant process in characterizing thermal plasma, electrical discharges and the production of laser system, as well as in atmospheric chemistry[104]. For Auger recombination, Interatomic Coulombic Decay (ICD) is a hot topic nowadays in the literature, because the process can be highly efficient when the excited ion has many neighbors and ICD leads to many examples of fragmentation[105–109]. The simplest approach for modeling these processes is to use straightforward classical probability theory[41,100,110].

While the processes above have a bath of electronic states which leads to a certain amount of electronic friction and a lack of coherence, a second class of non-adiabatic processes involves only a minimal number of electronic states. These non-adiabatic

problems in chemistry include most forms of photoexcited dynamics at low energies in solution, including electron transfer and electronic energy transfer[111–118], spin relaxation[119–122], intersystem-crossing[123–127], etc. These coherent dynamics are important for understanding organic enzymes, molecular photocatalysis and organic photoexcitations. In practice, modeling this second class of relaxation events requires different tools from the first class. Nuclei must move coherently for a reasonably long period of time. In practice, a few methods exist for modeling such dynamics including Meyer-Miller-Stock-Thoss (MMST)/Poisson bracket mapping equation (PBME)[1–9], multiple spawning[10–12] and fewest-switches surface hopping (FSSH)[13]. Given our group's recent experience with FSSH, we will focus on FSSH.

Now, many processes in nature involve both short time electronic coherent and long time incoherent probabilistic electronic dynamics. However, even though both areas have been studied extensively for a long time both experimentally and theoretically, there are few efficient theoretical approach to address both problems above where competition between coherent non-adiabatic processes and incoherent relaxation processes becomes predominate and interesting. The goal of the present article is to study a surface-leaking FSSH (SL-FSSH) algorithm that combines Preston's surface-leaking[41] with Tully's FSSH algorithm[13], benchmark the performance of SL-FSSH in system-bath model problems against quantum scattering calculation, and investigate dynamics beyond the wide band approximation to characterize the limitations of our algorithm. In a companion paper, we will discuss and benchmark a very similar surface hopping approach in the context of a many body physics problem (the Anderson-Holstein model)[42].

An outline of this article is as follows. In Section 3.2, we review briefly Tully's FSSH algorithm and Preston's surface-leaking (SL) algorithm, and then outline the SL-FSSH algorithm. In Section 3.3, we compare exact and SL-FSSH results for three

model problems with different sets of parameters. In Section 3.4 we investigate the sources of error in the SL-FSSH calculation, and we discuss the wide band approximation and its breakdown. Section 3.5 concludes this paper.

3.2 Surface-Leaking FSSH

3.2.1 Tully's Fewest-Switches Surface Hopping

For modeling photoexcited molecular dynamics in solution, the most common prescription is Tully's fewest-switches surface hopping (FSSH) algorithm[13]. A representative Hamiltonian in a diabatic basis can be written as:

$$\mathbf{H} = \mathbf{T}_n + \mathbf{H}_e \tag{3.1}$$

where $\mathbf{T}_n$ is the nuclear kinetic energy operator and the electronic Hamiltonian $\mathbf{H}_e$ can be written as:

$$\mathbf{H}_e = \sum_i E_i(\mathbf{R}) \left|\Xi_i\right\rangle \left\langle\Xi_i\right| + \sum_{i \neq j} \mathcal{V}_{ij}(\mathbf{R}) \left(\left|\Xi_i\right\rangle \left\langle\Xi_j\right| + \left|\Xi_j\right\rangle \left\langle\Xi_i\right|\right) \tag{3.2}$$

where $\left|\Xi_i\right\rangle$ is the i^{th} electronic diabat, E_i is the energy of diabatic state i and $\mathcal{V}_{ij}$ is the diabatic coupling between states i and j. The premise of FSSH is that electrons are treated quantum mechanically while nuclei are classical, while all calculations are performed exclusively in an adiabatic basis:

$$\mathbf{H}_e = \sum_j V_{jj} \left|\Phi_j\right\rangle \left\langle\Phi_j\right| \tag{3.3}$$

where V_{jj} is the adiabatic energy of state j and $\left|\Phi_j\right\rangle$ is the corresponding adiabat. In detail, while the electrons move in the instantaneous electric field caused by the

nuclei, the nuclei move along one single potential energy surface (PES) at a time and hop (once in a while) between different PESs to account for electronic relaxation. Preston and Tully first suggested that hops should be made post-facto[128], whereby one can decide if he/she has gone through a crossing. According to Tully's later FSSH model[13], there is a continuous hopping probability at every time step – which depends on both the derivative coupling between adiabatic electronic states and the history of each trajectory. In particular, according to the FSSH algorithm, for each trajectory we must propagate the positions ($\mathbf{R}$) and momenta ($\mathbf{P}$) of each nuclear degree of freedom according to Newton's equations, and the corresponding electronic quantum amplitudes (c_i) for each adiabatic electronic state i according to time-dependent Schrödinger equation. The hopping can then be extracted from the evolution of this trajectory.

While the FSSH algorithm has several known problems modeling photoexcited systems with a few electronic states (including decoherence[20,23–40,129]), another obstacle posed by the FSSH algorithm is its insistence on an adiabatic basis and the difficulty running FSSH dynamics for systems with large numbers of degrees of freedom. In such a limit, one problem is that the cost of the algorithm increases at least quadratically with the number of electronic states (n_{tot})[130] because one is forced to compute the derivative couplings between all n_{tot} electronic states to propagate the Schrödinger equation. In the limit of a molecular system near a metal surface, the number of electronically adiabatic states becomes very large and standard FSSH becomes impossible. Another practical problem for FSSH is the conundrum of "trivial crossings,"[116] where two or more noninteracting states cross, leading to a spiky derivative coupling in time domain and severely limiting the simulation time step. There has been a lot of recent research[116,131–133] seeking to address this problem. In recent year, Tretiak[116] has studied energy transfer in extended organic chromophores

by applying FSSH to simulation with a large manifold of electronic states. For such simulations, he has consistently found that the "trivial crossing" problem cannot be ignored in practice.

To our knowledge, there has been only a few literature in the field that attempts to heuristically amend FSSH dynamics to include manifold of many electronic states (without using brute force). Li *et al* have proposed a scheme for mixing FSSH dynamics on the ground states with mean-field Ehrenfest dynamics to treat a manifold of excited states.[134] In a set of very interesting papers, Shenvi, Roy and Tully[43–45] proposed and "Independent Electron Surface Hopping (IESH)" algorithm that has been used to model NO scattering off of a gold surface. For IESH, the basic premise is to discretize a continuum of electronic levels and then run independent trajectories, for which every electron is independent and single excitations of the metal manifold are allowed. Electronic friction is simulated by averaging over the ensemble of trajectories, and Shenvi *et al* have shown that this model captures vibrational relaxation of the NO molecule as induced by electron transfer to and from the metal. Given the power of the IESH model, we would like to find a very simple extension of FSSH for the case of many electronic states that does not require continuum discretization and that has the smallest possible computational overhead.

3.2.2 Surface-Leaking Algorithm

In contrast to the FSSH algorithm, which is usually applied for only a handful of electronic excited states, there is a different (far less well known, but also far simpler) approach in the literature for treating coupled nuclear-electronic systems with many electronic states. As originally constructed to model the effects of chemi-ionization on atom-diatom collisions,[41], the Preston-Cohen "surface leaking" (SL) model was used to predicts rearrangement, association, and dissociation branching ratios from

atom-diatom collisions.

Conceptually, the surface leaking model is very simple. Consider a Hamiltonian of the form:

$$\mathbf{H} = \mathbf{T}_n + \mathbf{H}_s + \mathbf{H}_b + \mathbf{H}_{sb} \tag{3.4}$$

Here, $\mathbf{T}_n$ denotes the nuclear kinetic energy operator and $\mathbf{H}_s$ represents the electronic Hamiltonian of the system,

$$\mathbf{H}_s = \sum_j E_j(\mathbf{R}) \left|\Xi_j\right\rangle \left\langle\Xi_j\right|, \tag{3.5}$$

and $\mathbf{H}_b$ represents a bath of electronic states:

$$\mathbf{H}_b = \sum_k \varepsilon_k(\mathbf{R}) \left|k\right\rangle \left\langle k\right| \tag{3.6}$$

$\mathbf{H}_{sb}$ signifies the coupling between system and bath which we assume is bilinear in the electronic degrees of freedom and a function of only nuclear position:

$$\mathbf{H}_{sb} = \sum_{jk} U_{jk}(\mathbf{R}) \left(\left|\Xi_j\right\rangle \left\langle k\right| + \left|k\right\rangle \left\langle\Xi_j\right|\right) \tag{3.7}$$

For an infinite bath, the system-bath interaction is quantified by its hybridization function:

$$\Gamma_j(\mathbf{R}) = 2\pi\rho(E_j(R))\overline{\left|U_{jk}(\mathbf{R})\right|^2} \tag{3.8}$$

Here $\left|U_{jk}\right|^2$ is averaged over all states $\left|k\right\rangle$ with energy $E_j(\mathbf{R})$. If $\left|U_{jk}\right|^2$ is truly independent of k, $\Gamma_j(\mathbf{R})/\hbar$ can be thought of as the lifetime of the system electronic state j (when the nuclei are at position $\mathbf{R}$). The basic premise of the surface leaking algorithm is to run nuclear dynamics along a potential energy surface of the system, while damping the population of the system by $\Gamma_j(\mathbf{R})\Delta t/\hbar$ at every time step (where

Δt is the simulation time step).

3.2.3 SL-FSSH

Given how many modern experiments involve photoexcited systems of molecule-metal interface[135–137], it would seem very natural to merge the surface leaking and surface hopping algorithms. In so doing, one would like to include both the short-time electronic coherence present in the FSSH algorithm (so as to capture potential energy surface crossings) with the long time irreversible electronic relaxation present in the SL algorithm (so as to capture electronic dissipation into a metallic bath). In other words, we would like to replace the simple system Hamiltonian in Eq. (3.5) with the more complex Hamiltonian in Eq. (3.2).

In principle, merging SL and FSSH should be straightforward to achieve. On the one hand, one ought to diagonalize the electronic states of the system and run FSSH dynamics along such adiabatic states; on the other hand, one does not want to include bath states in the above diagonalization, and one would prefer to use perturbation theory on the system-bath coupling to model the population leakage from the system to the bath. In theory, this approach should be equivalent to including complex energies in the time-dependent electronic Schrödinger equation[138] to damp out population and then allow the FSSH algorithm to dictate naturally how population evolves. In this paper, we want to formalize exactly how the algorithm is applied, discuss the competition between surface leaking and surface hopping, and then formally benchmark the resulting algorithm against exact scattering calculations.

With this in mind, a step-by-step description of our SL-FSSH algorithm is as follows:

1. Initialize all FSSH variables: the positions $\mathbf{R}$ and momenta $\mathbf{P}$ of the nuclei, the current electronic state (active PES) λ, and the electronic amplitudes c_i

according to the initial condition. Each trajectory also carries a weight, $N_{sys} = 1$, to represent the population of system.

2. (Same as FSSH) Propagate the nuclei and electronic wave functions for one time step. The nuclei are propagated by classical mechanical equations:

$$\frac{dR^\alpha}{dt} = \frac{P^\alpha}{M^\alpha} \tag{3.9}$$

$$\frac{dP^\alpha}{dt} = -\nabla_\alpha V_{\lambda\lambda}(\mathbf{R}) \tag{3.10}$$

where α labels a classical degree of freedom, $V_{ij}(\mathbf{R})$ are the matrix elements of electronic Hamiltonian at position $\mathbf{R}$ in an adiabatic basis, and M is the mass of a nucleus. The electronic amplitudes are propagated by time-dependent Schrödinger equation:

$$i\hbar\frac{dc_k}{dt} = \sum_j c_j \left(V_{kj}(\mathbf{R}) - i\hbar\frac{d\mathbf{R}}{dt}\cdot\mathbf{d}_{kj}(\mathbf{R}) \right) \tag{3.11}$$

where $\mathbf{d}_{kj}(\mathbf{R})$ is the non-adiabatic coupling vector between state k and j at position $\mathbf{R}$.

3. (Same as FSSH) Hopping probabilities $g_{\lambda j}$ from the current electronic state λ to all other states j are determined as in FSSH:

$$g_{\lambda j} = -\frac{2}{|c_\lambda|^2}\,\mathrm{Re}\left(c_\lambda c_j^* \mathbf{d}_{j\lambda}(\mathbf{R})\cdot\frac{d\mathbf{R}}{dt} \right) \tag{3.12}$$

A uniform random number ξ in $[0,1]$ is then generated and compared with the cumulative hopping probability to determine the target state. For instance, if $\lambda = 1$ and $\xi < g_{12}$ then current electronic state changes to state 2; if $g_{12} \le \xi < g_{12} + g_{13}$ the current electronic state changes to state 3, etc. If ξ is larger than

the sum $\sum_j g_{\lambda j}$, then no hopping happens and current electronic state remains unchanged.

4. (Same as FSSH) If a hop does not occur, proceed to step 5. If there is a hop, the momentum must be rescaled to account for energy conservation. The momentum is rescaled in the direction of the non-adiabatic coupling vector (assuming we are hopping from current state λ to state j):

$$\mathbf{P}^{new} = \mathbf{P} + \Delta P \hat{\mathbf{d}}_{\lambda j}(\mathbf{R}) \tag{3.13}$$

$$\sum_\alpha \frac{(P^{\alpha,new})^2}{2M^\alpha} + V_{jj}(\mathbf{R}) = \sum_\alpha \frac{(P^\alpha)^2}{2M^\alpha} + V_{\lambda\lambda}(\mathbf{R}) \tag{3.14}$$

where $\hat{\mathbf{d}}_{\lambda j}(\mathbf{R})$ is the unit vector of non-adiabatic coupling vector at position $\mathbf{R}$. If $\mathbf{P}^{new}$ is complex, the hop is not allowed. If $\mathbf{P}^{new}$ is real, a hop is allowed and the active surface is changed (in this case, to j).

5. (From SL) For a general Hamiltonian, the electronic bath might couple to an arbitrary electronic state of the system – which might be an adiabatic or diabatic state (or some other entirely different state). Assuming that the bath is coupled to a diabatic system state, we calculate the diabatic population $n_i^{(diab)}$ on each state i; for now, this is done using only the active surface (which is labeled to Method #1 in Ref. 73; see below for a few details). Then, we calculate the probability $L_i(\mathbf{R})$ of leaking out of the system from state i to its corresponding bath (the same as in the SL algorithm):

$$L_i(\mathbf{R}) = \frac{\Gamma_i(\mathbf{R})\Delta t}{\hbar} \tag{3.15}$$

Finally, the new and reduced population remaining on system state is updated:

$$N_{sys}^{(new)} = N_{sys}^{(old)} \left(1 - \sum_i n_i^{(diab)} L_i(\mathbf{R}) \right) \tag{3.16}$$

Return to step 2.

At the end of the calculation, all trajectories must be summed and weighted with N_{sys}, which must be in the range $[0, 1]$. Because N_{sys} does not have any feedback into the FSSH dynamics, SL-FSSH is very easy and straightforward to implement. Note here that, by ignoring the hopping from the bath back to the system, we are assuming that the bath is infinitely wide. In Section 3.4.3, we will discuss the use of SL-FSSH beyond the wide band approximation.

One word is now in order about how to calculate diabatic populations assuming that the bath is coupled to the diabatic populations. In this case, Ref. 73 shows that there are three straightforward means to extract diabatic populations: one can use either (i) the active electronic surface, (ii) the electron amplitudes c_i, or (iii) a combination of both active surface and amplitudes. While the third option is the most rigorous[73], unfortunately, such an option also requires that all trajectories be coupled to each other in real time, and thus is not practical for large systems. At the same time, option (ii) simply cannot recover correct long time populations[73]. Thus, option (i) is likely the only possible balance between accuracy and scalability.

3.3 Results

To investigate the algorithm presented above, we will study a set of system-bath interaction models, all restricted to one nuclear degree of freedom. The electronic system is one or two discrete states, and the bath in principle represents a continuum of states. In practice, the bath is discretized into a set of 501 parallel states for

the exact scattering calculations (see Appendix for the algorithm). The coupling between system and bath is position dependent and there is no intra-bath interaction. All simulations begin with one system state populated, followed subsequently by a combination of interstate transfer and/or relaxation into the bath. For our scattering calculation we examine transmission and reflection probabilities. We will investigate two extreme cases: (*i*) a primary system state crosses a bath of parallel electronic states; (*ii*) a primary system state is parallel to a set of bath states. See Fig. 3.1 for the diabatic potential energy surfaces (PESs) for the three model problems we will study.

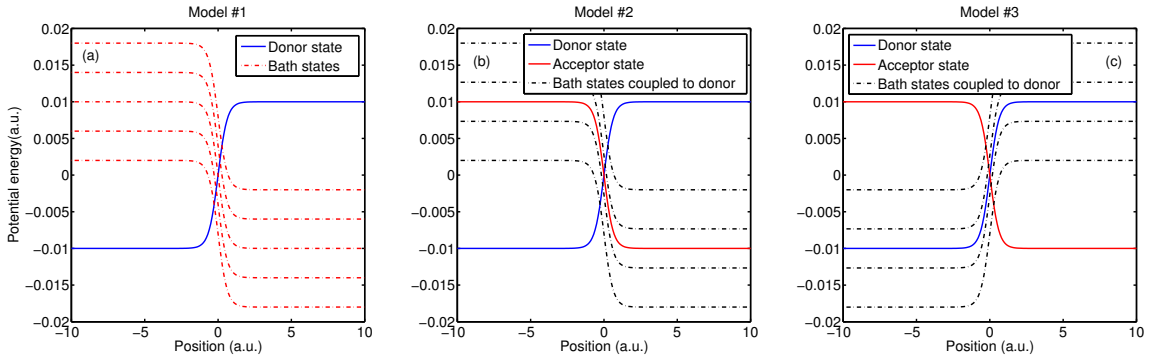

Figure 3.1: Three model problems mentioned in this manuscript. The diabatic coupling is not shown. The solid curves are the system states and dash curves are the bath states (of variable width). Note that, as drawn, the Hamiltonians appear to have only 4-5 bath states. In truth, more than 500 bath states were use for the quantum scattering calculations; for the SL-FSSH calculation, the bath is a truly infinite continuum of states. (a) Model #1: one donor state coupled to a nonparallel set of bath states. (b) Model #2: one donor state coupled to one acceptor state while the donor state is coupled to a set of nonparallel bath states. (c) Model #3: one donor state coupled to one acceptor state while the donor state is coupled to a set of parallel bath states.

3.3.1 Model #1: One System State Couples to a Set of Nonparallel Bath States

Model #1 is the simplest Hamiltonian we consider. This model can be treated easily with the surface-leaking algorithm alone (without invoking FSSH). There is only one system state:

$$V_{sys}(x) = A\tanh(Bx), \tag{3.17}$$

where $A = 0.01$ *a.u.* and $B = 1.6$ *a.u.*. The set of bath states take the following form:

$$V_{bath}(x) = -V_{sys}(x) + \Delta \tag{3.18}$$

where Δ is a shift in energy (which can be either positive or negative). A set of diabatic PES are shown in Fig. 3.1(a) for five different energy offsets, $\Delta = 0.008$, 0.004, 0, -0.004, 0.008, all in atomic unit.

The diabatic coupling between system and bath is given by V_{sb}:

$$V_{sb}(x) = C\exp(-Dx^2) \tag{3.19}$$

where $D = 1.0$ *a.u.*. To make the definition of C consistent with an infinite set of bath states, C is defined as

$$C \equiv \sqrt{\frac{\Gamma(0)}{2\pi\rho}} \tag{3.20}$$

in agreement with Eq. (3.8). Thus $\Gamma(0)$ is our free parameter of choice (not C). For our exact scattering calculation where the bath is discretized, the density of states of bath ρ is simply:

$$\rho = \frac{N_{bath}}{\Delta E_{bath}} \tag{3.21}$$

Here N_{bath} is the number of states in bath and ΔE_{bath} is the energy range of the bath.

The model problem above is particularly simple because we have only one system state. As such, there are no coherent processes and every trajectory with the same incoming energy gives exactly the same result. In other words, model #1 can be considered deterministic, so that one trajectory result is sufficient. At the beginning of the SL simulation, we set $n_i^{(diab)}(x)$ in Eq. (3.16) to be 1 for all x. Let us now explore the transmission and reflection probabilities, first for the bath states and then for the system state.

Dynamics of the Bath

To explore the distribution of population on the bath states, we run a set of surface-leaking calculations whereby each trajectory is initialized with an incoming particle on left moving along the system state. We consider two different cases with different incoming kinetic energies: (i) the incoming velocity is large enough to transmit along the system state; (ii) the incoming energy is small enough that there will be reflection along the system diabat, with the possibility for multiple crossing. To explore the problem in the fully classical limit, we set the nuclear mass to be 100000 $a.u.$. We set $\Gamma(0) = 10^{-4}$ $a.u.$ to ensure that we are in the weak coupling regime.

In Fig. 3.2, we plot the transmission probability density for the different bath states as a function of outgoing kinetic energy, according to both exact dynamics and the surface-leaking algorithm.[2] These distributions are obtained by calculating how much population is leaked by each trajectory into the bath at every time step, visualizing the bath state that crosses the system state instantaneously, and then recording the asymptotic potential energy of that crossing bath state. By conservation of energy, we can make a histogram of the distribution of outgoing kinetic energies. For Fig. 3.2, the incoming kinetic energy is large, 0.025 $a.u.$, so there need not be any reflection.

[2]To construct a probability density from a finite scattering calculation, one multiplies the probability of a given channel to be occupied by the density of states.

In fact, we find no reflection, so we plot only transmission. Note that larger outgoing kinetic energies correspond to transmission through lower energy channels.

According to Fig. 3.2, there is a strong overall agreement between surface-leaking and exact results. All SL errors lie on the edges of the kinetic energy distribution. Our strong feeling is that these errors must be caused by nuclear quantum effects, e.g. tunneling. In Section 3.4.2, we will redraw Fig. 3.2 for a particle of smaller mass to reinforce this hypothesis.

In Fig. 3.3-3.4, we treat a slightly more difficult case. For this calculation, the incoming kinetic energy is 0.015 $a.u.$. In this case, the nucleus has too little energy to transmit forward along the system state, and there will be population reflecting backwards. In Fig. 3.3, we plot transmission; in Fig. 3.4, we plot reflection. According to Fig. 3.4, the SL probability of reflection is in good agreement with exact quantum dynamics; however, there are clear discrepancies in transmission between SL and exact quantum dynamics. On the one hand, according to exact dynamics, we observe oscillations in probability between 0.005 and 0.2 $a.u.$ of kinetic energy. On the other hand, SL predicts a sudden drop in transmission as the outgoing kinetic energy grows and passes 0.02 $a.u.$. At the same time, the exact dynamics predict a smooth peak in population at outgoing energy $\sim$ 0.006 $a.u.$, while SL predicts a sharp peak in population at the smallest outgoing kinetic energy allowed (0.005 $a.u.$). These differences will be explored in detail in Section 3.4.1 but, for now, we comment that these differences should not limit the accuracy of the SL algorithm. Overall, the SL algorithm performs well for this trivial problem.

Dynamics of the System State

Having investigated the dynamics of the bath states, we now turn our attention to transmission and reflection along the system state. Fig. 3.5 explores the performance

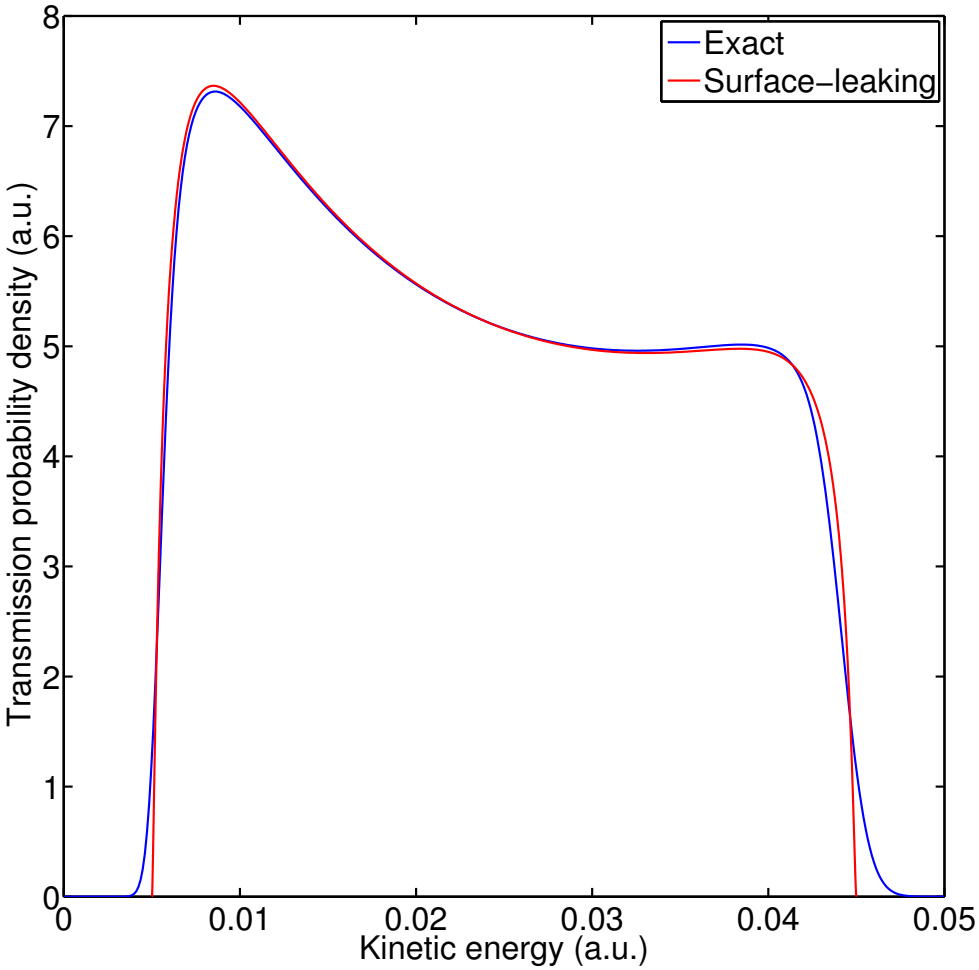

Figure 3.2: Model #1: Transmission probability density for the bath states as a function of outgoing kinetic energy according to both exact dynamics and the surface-leaking algorithm. The incoming kinetic energy is 0.025 $a.u.$, the nuclear mass is 100000 $a.u.$ and $\Gamma(0)$ is 10^{-4} $a.u.$. Note the good agreement.

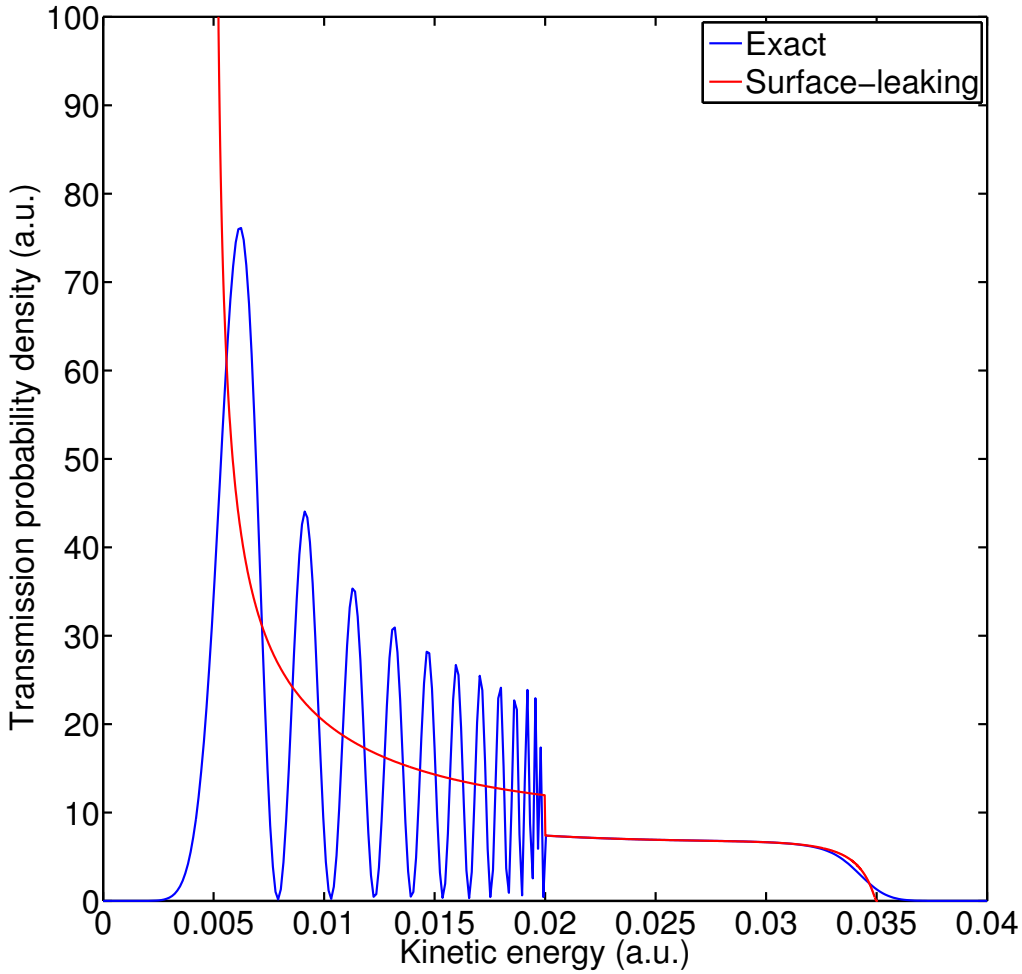

Figure 3.3: Model #1: Transmission probability density for the bath states as a function of outgoing kinetic energy according to both exact dynamics and the surface-leaking algorithm. The incoming kinetic energy is 0.015 $a.u.$, the nuclear mass is 100000 $a.u.$ and $\Gamma(0)$ is 10^{-4} $a.u.$. The differences between exact dynamics and SL will be explored in Section 3.4.2.

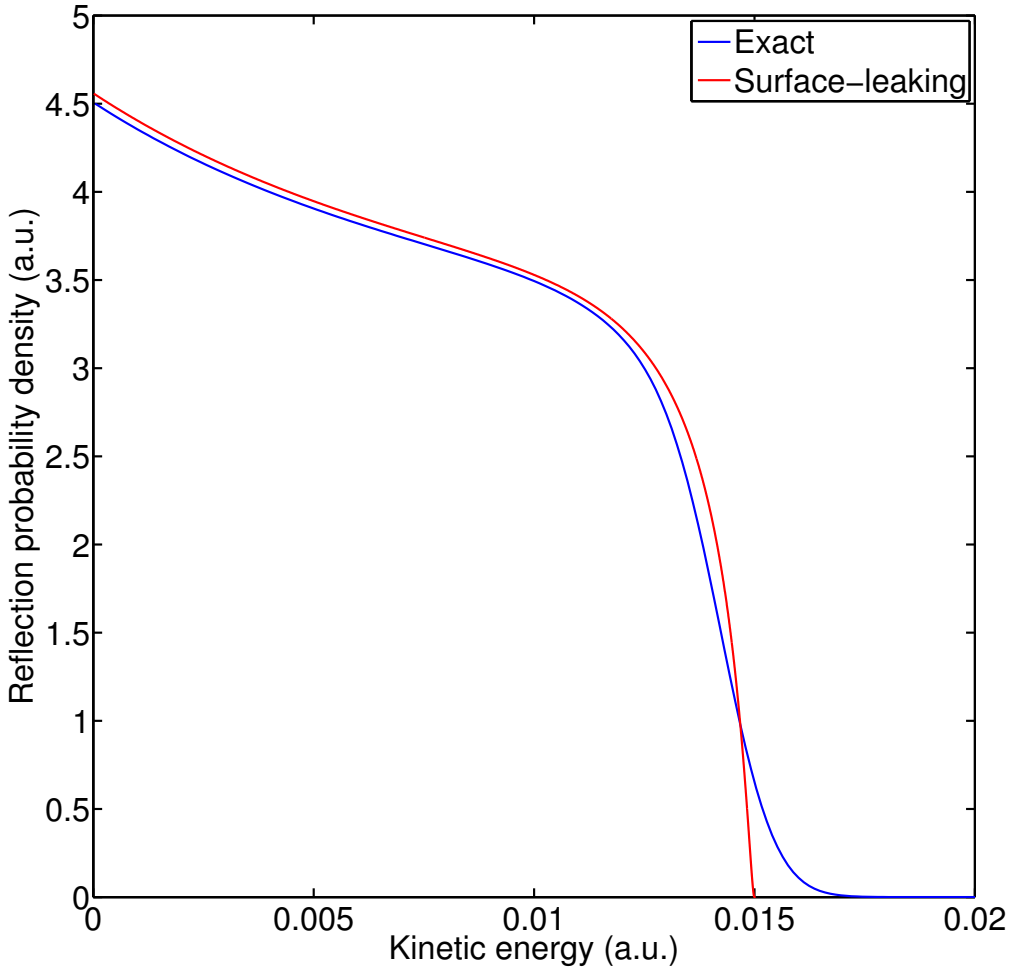

Figure 3.4: Model #1: Reflection probability density for the bath states as a function of outgoing kinetic energy according to both exact dynamics and the surface-leaking algorithm. The incoming kinetic energy is 0.015 $a.u.$, the nuclear mass is 100000 $a.u.$ and $\Gamma(0)$ is 10^{-4} $a.u.$. Note the good agreement.

of surface-leaking over a wide range of incoming kinetic energies (plotting transmission and reflection probability on the system state, $\Gamma(0) = 10^{-4}$ $a.u.$). Fig. 3.6 plots transmission and reflection as a function of $\Gamma(0)$ (keeping the incoming kinetic energy equal to 0.025 $a.u.$). In both figures, surface-leaking agree with exact quantum dynamics, further confirming that surface-leaking is the correct approach for this class of problems. As a point of comparison, in Fig. 3.5 we also plot results from a full FSSH simulation with 10 discretized baths states (as averaged over 2000 trajectories). With only 10 bath states, the FSSH results agree with exact quantum results and surface-leaking results for large incoming kinetic energy where only transmission is significant, but FSSH cannot recover the correct branching ratios for small incoming kinetic energy with only 10 bath states. Instead of a monotonic decline, notice the interesting oscillations in the FSSH reflection probabilities as a function of incoming kinetic energy. These FSSH oscillations can be understood as follows. First, if a frustrated hop is encountered, an incoming FSSH trajectory will follow the active adiabatic PES and "leak" into the bath and produce a small reflection probability. Second, while frustrated hops correspond to energies with too small a reflection probability, there are other energies for which FSSH predicts a reflection probability that is too large – these overestimates must be caused by the overcoherence of FSSH. With this rationale in mind, one would expect to find sharp oscillations in FSSH reflection branching ratios as a function of incoming kinetic energy no matter how many bath states are assumed. As such, beyond computational efficiency, the surface-leaking algorithm has some obvious advantages over FSSH when dealing with a true continuum of electronic states.

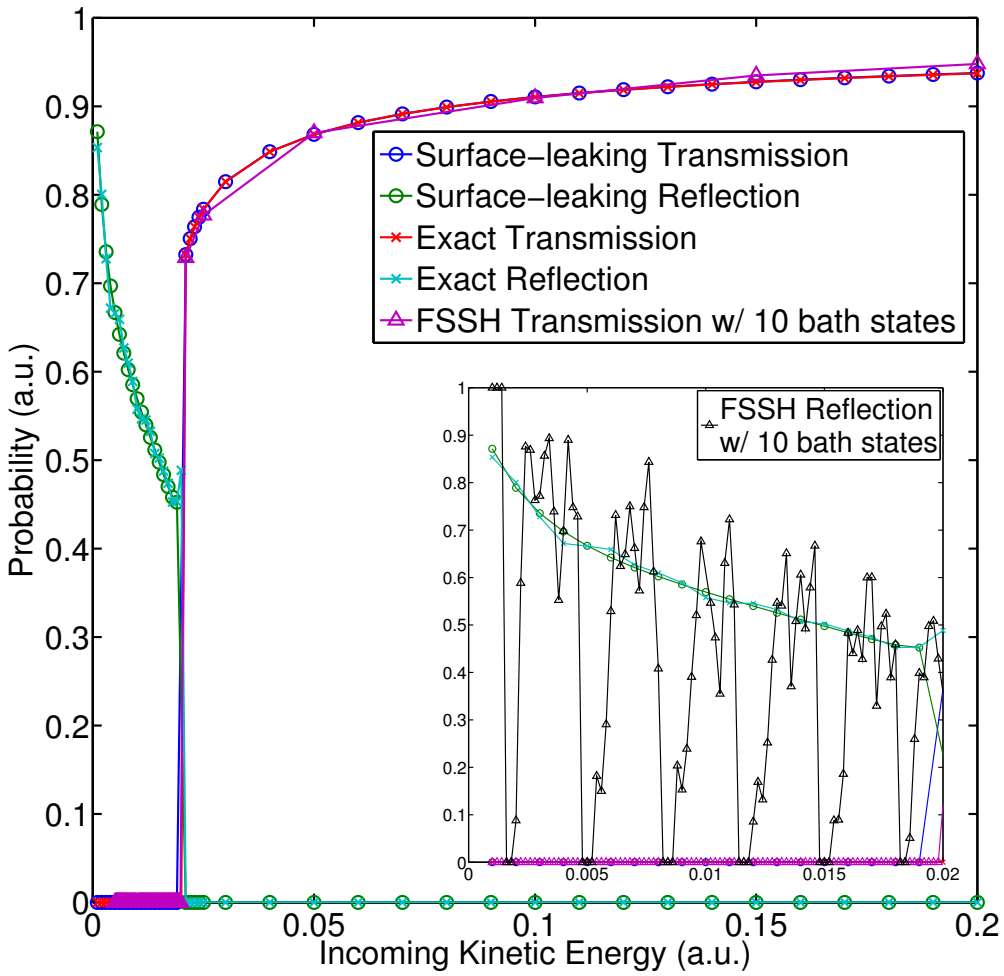

Figure 3.5: Model #1: Surface-leaking and exact transmission and reflection probabilities on the system state as a function of incoming kinetic energy. $\Gamma(0)$ is 10^{-4} $a.u.$. Note the good agreement. In this figure, we also plot results using the FSSH algorithm for a bath of 10 electronic states. In the inset, we plot reflection data for FSSH with 10 states. Clearly, at low velocity, SL-FSSH outperforms a full FSSH calculation with only 10 states. See text for more detail.

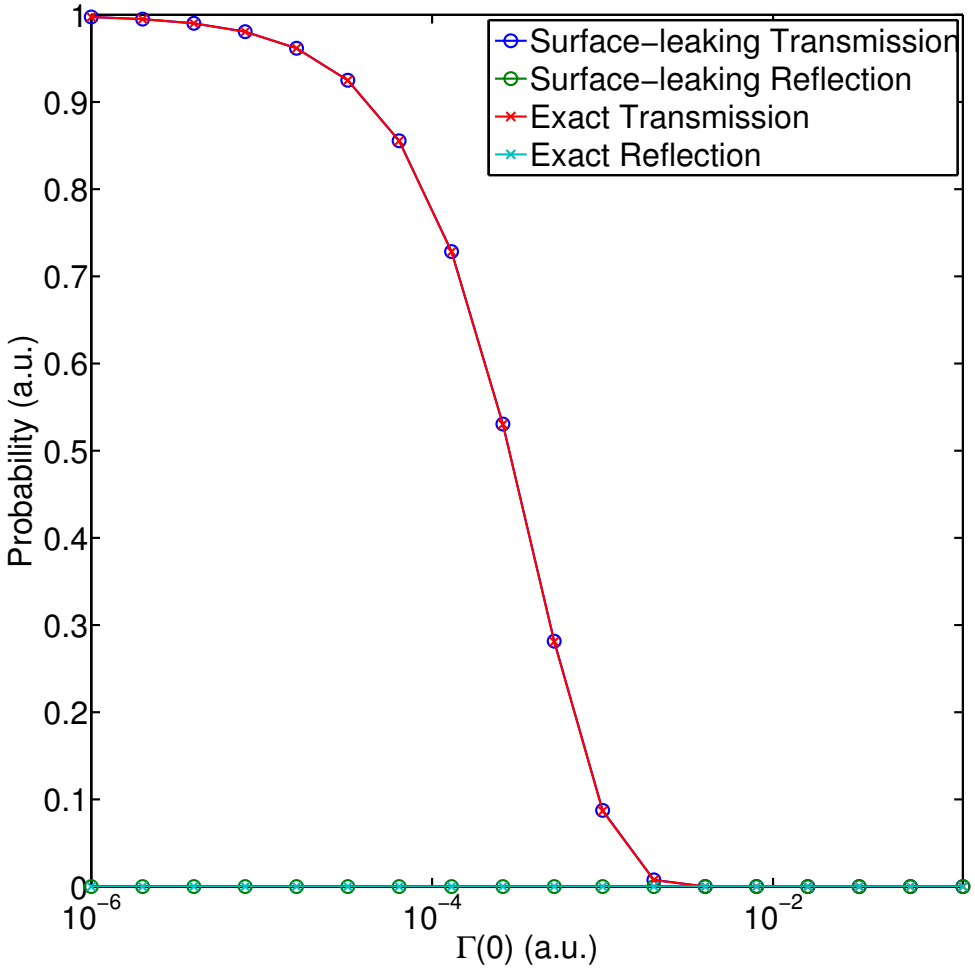

Figure 3.6: Model #1: Surface-leaking and exact transmission and reflection probabilities on system state as a function of $\Gamma(0)$. The incoming kinetic energy is 0.025 $a.u.$. Note the good agreement.

3.3.2 Model #2 and #3: Two System States With One Couples to a Set of Bath States

Having investigate the bare surface-leaking model, let us now consider the SL-FSSH model and add another system state to the Hamiltonian in Model #1. This change will allow for the possibility of some coherent non-adiabatic dynamics in addition to electronic relaxation. The Hamiltonians for two new models (#2, #3) are as follows:

$$V_{11}(x) = A\tanh(Bx) \tag{3.22a}$$

$$V_{22}(x) = -V_{11}(x) \tag{3.22b}$$

$$V_{21}(x) = V_{12}(x) = C\exp(-Dx^2) \tag{3.22c}$$

$$U(x) = 0.5K\left(\tanh(x+15) + \tanh(15-x)\right) \tag{3.22d}$$

where $A = 0.01$, $B = 1.6$, $C = 0.005$, $D = 1.0$ and K is a constant defined in the same manner as C in Eq. (3.20), and all in atomic units.

For both model problems, the system consists of two diabatic states: a donor state (Eq. (3.22a)) and an acceptor state (Eq. (3.22b)), and the coupling between them is Eq. (3.22c). For both model problems, the donor state is coupled to a set of bath states, and the system-bath coupling is shown in Eq. (3.22d). The manifold of bath states will be different for the two models. For model #2, the set of bath states is

$$V^{(2)}_{bath}(x) = V_{22}(x) = -A\tanh(Bx) \tag{3.23}$$

while for model #3, the set of bath states is:

$$V^{(3)}_{bath}(x) = V_{11}(x) = A\tanh(Bx) \tag{3.24}$$

Thus, one can think of model #2 as the donor state coupled to a set of nonparallel bath states, while the set of bath state is parallel to the donor state in model #3. A set of 6 total diabatic PESs are shown in Fig. 3.1(b) and (c) for models #2 and #3, respectively.

For these simulations, following Tully's original paper[13], the mass of the nucleus is set to 2000 $a.u.$ and the simulation is incoming from the left on V_{11}. To keep the calculations as simple as possible (without worrying representation unnecessarily), we will focus on the system populations only and we will not calculate bath distributions. Lastly, it is important to note that, in the wide band limit, models #2 and #3 are effectively identical; indeed, the SL calculations are exactly identical. For this reason, we will show only results from Model #3 in this section. To explore the differences between Models #2 and #3, see Section 3.4.3 where we report results beyond the wide band approximation.

Fig. 3.7 shows the FSSH (with no bath), SL-FSSH and exact results for transmission probability along the system state as a function of incoming kinetic energy. $\Gamma(0)$ is 10^{-4} $a.u.$. The overall agreement between SL-FSSH and exact dynamics is excellent over a wide range of incoming kinetic energies. The fact that SL-FSSH and FSSH have the same overall shape seemingly confirms the notion that the relaxation into the bath does not change the nature of the surface hopping. Notice that, as the incoming kinetic energy grows, the fraction of population remaining in the system increases, as it must (since the particle spends less time leaking into the bath).

Fig. 3.8 plots transmission as a function of $\Gamma(0)$. The incoming kinetic energy is 0.2 $a.u.$. Note here that, for FSSH (as opposed to SL-FSSH) calculations, the system is not coupled to a bath, so that all FSSH results are independent of $\Gamma(0)$. The agreement between SL-FSSH and exact dynamics is again excellent. As one would expect, transmission on both system states decreases as $\Gamma(0)$ increases – because

larger $\Gamma(0)$ leads to more relaxation into the bath. When $\Gamma(0)$ is large enough, no population survives on the system before the nucleus transmits to the right. One interesting feature of Fig. 3.8 is the competition between surface hopping and surface leaking. When $\Gamma(0)$ is small, the transmission on the upper system state is larger than that on the lower system state. As $\Gamma(0)$ increases, however, the transmission on the upper system state decreases faster than on the lower system state, and around $\Gamma(0) = 10^{-3}$ $a.u.$, the transmission on the upper system state surprisingly becomes smaller than transmission on the lower system state. This relative change in branching ratios occurs because it is the population on diabat 1 alone that leaks into the bath. Thus, on the one hand, the wavepacket transmitting on the upper state is always moving approximately along V_{11} and is constantly decaying; on the other hand, the wavepacket that transmits on lower state moves approximately along V_{22} after it leaves the coupling region, so that decay ceases in time.

Overall, the excellent agreement in both figures between SL-FSSH and exact dynamics suggests the SL-FSSH algorithm is viable in dealing with both irreversible electronic relaxation and short-time coherent non-adiabatic processes.

3.4 Discussion

There are now a few items above worth discussing in detail.

3.4.1 Decoherence: Averaging over an Initial Wigner Wavepacket

Recall the oscillations in transmission probabilities in Fig. 3.3. The oscillations exist for outgoing kinetic energy less than 0.02 $a.u.$. A transmission kinetic energy of 0.02 $a.u.$ is special because, if one follows the corresponding diabatic bath for $x \to -\infty$, one finds that the corresponding reflecting wavepacket should have outgoing kinetic energy equal 0 $a.u.$. Thus, this is a special bath state. (See Fig. 3.9 for a

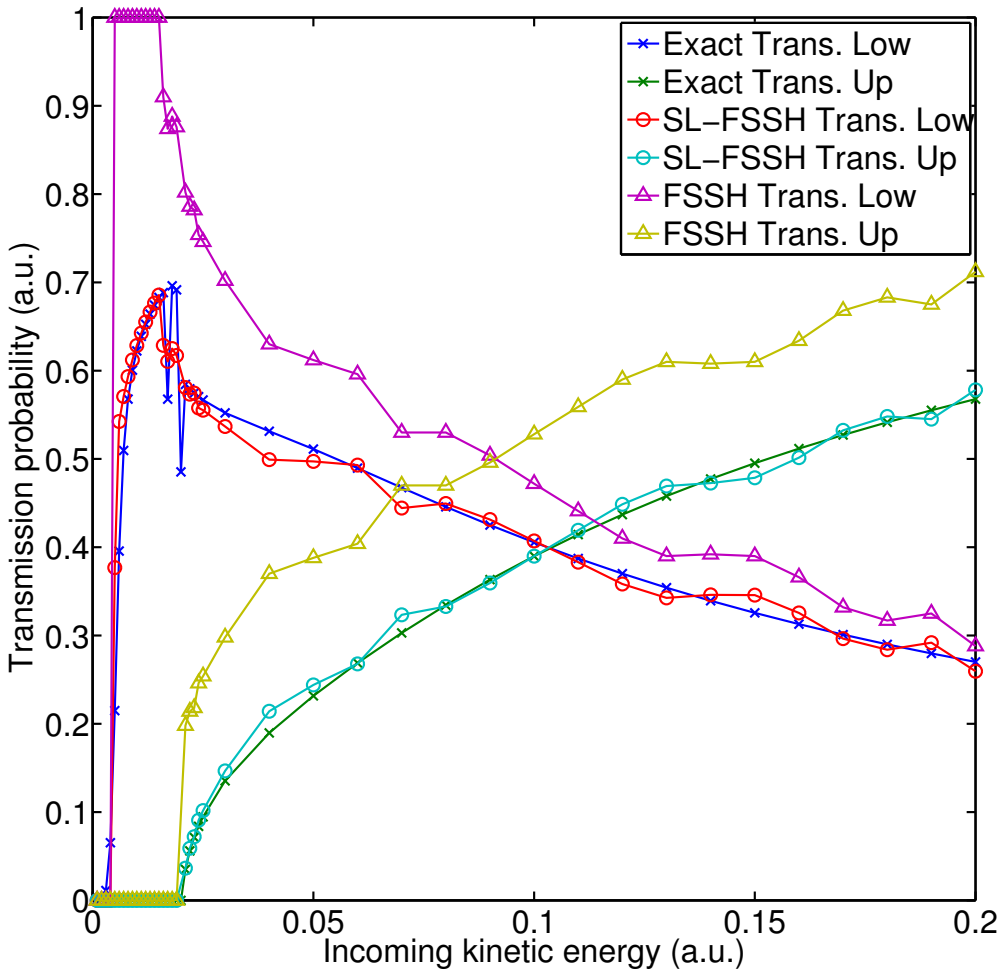

Figure 3.7: Model #3: FSSH, SL-FSSH and exact results for transmission probability on the system state as a function of incoming kinetic energy. $\Gamma(0)$ is 10^{-4} $a.u.$. Note the good agreement.

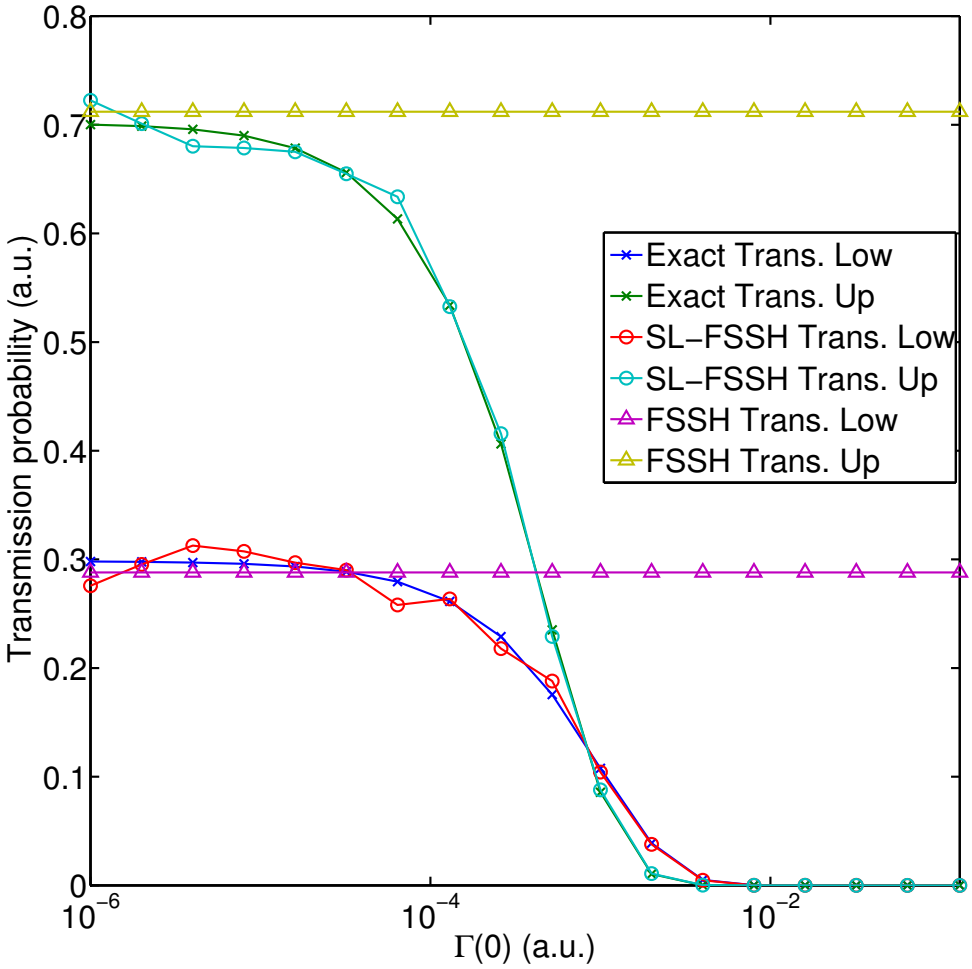

Figure 3.8: Model #3: FSSH, SL-FSSH and exact results for transmission probability on the system state as a function of $\Gamma(0)$. The incoming kinetic energy is 0.2 *a.u.*. Note the good agreement.

schematic view of the relevant wavepacket dynamics.) For bath states below this special bath state (with less potential energy), reflection is energetically allowed. But for bath states above this special bath state (with more potential energy), reflection is not energetically allowed. So any wavepacket attempting to reflect on such a diabat asymptotically must turn around and transmit to the right instead. In such a case, for a wavepacket wide enough in position space, one expects to find interference between directly transmitting wavepacket and the wavepacket that bounces back and forth. Such interference leads to the oscillations in Fig. 3.3.

The physics described above have an analogue in the surface-leaking algorithm, but in a slightly different form. Because Γ does not keep track of the coherence between wavepackets on different diabats, one does not find the oscillations in transmission in Fig. 3.3. However, one does find a big step function at the 0.02 *a.u.* kinetic energy threshold. (The peak in SL transmission in Fig. 3.3 at 0.005 *a.u.* kinetic energy is the result of the classical nucleus slowing down as it turns around to reflect; during this long time period, there is a lot of leakage into the bath.)

Now, in principle, the transmission oscillation in Fig. 3.3 should vanish if we average over a wavepacket that is wide enough in momentum space. Such initial conditions correspond to an incoming wavepacket that is narrow in position space and therefore the two transmitting wavepackets will exit the coupling region at different times with no interference. In such a case, the SL should be able to recover the exact results because there is no coherence in the dynamics – unlike FSSH[94], SL has no decoherence or multiple crossing problem.

To prove this point, see the averaged results in Fig. 3.10. For the exact quantum calculation, we calculate results for plane waves with different incoming momenta and

we average all resulting data over a Gaussian distribution:

$$\overline{|t_l|^2} = \sum_p |t_l(p)|^2 \, N \exp\left(-\frac{(p-p_0)^2}{2\sigma^2}\right) \Delta p \tag{3.25}$$

Here l is the index for a bath transmission channel, N is a normalization constant, p is the incoming momentum, p_0 is the average momentum of the wavepacket, σ is the width of wavepacket in momentum space and $|t_l(p)|^2$ represents the result transmission probability on state l when the incoming momentum is p. For the surface-leaking algorithm, we sample the initial momentum from the same Gaussian distribution as in Eq. (3.25). We invoke 2000 trajectories and set $\sigma = 1$. Note that, after averaging, surface-leaking and exact dynamics are in quite good agreement. (There is still a small disagreement in the peak position; we suspect this is a nuclear tunneling effect.)

3.4.2 The Mass Dependence of the Bath Dynamics

In Section. 3.3, we saw that the surface-leaking recovers exact quantum dynamics for system population when the mass of nucleus is either 2000 *a.u.* or 100000 *a.u.*. However, as the mass of nucleus becomes smaller, quantum effects (especially tunneling) become important when we calculate the population distribution in the bath states. In Fig. 3.11, we replot the calculation from Fig. 3.2, only now we change the nuclear mass to 2000 *a.u.*. For comparison, we include data from mass equals 100000 *a.u.* (Fig. 3.2). Even though the overall shape still matches, it is evident that the SL errors become larger as the mass decreases.

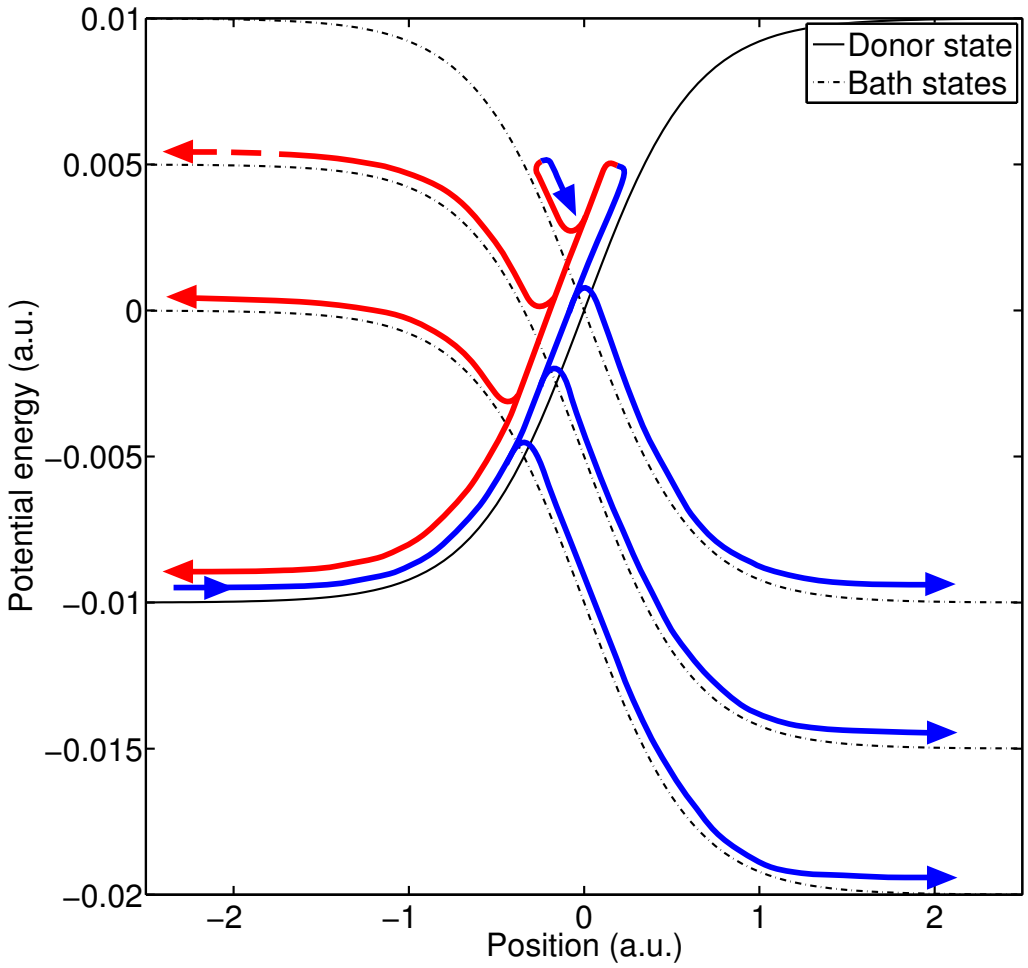

Figure 3.9: Model #1: Schematic figure showing the dynamics of population leaking associated with a nucleus whose incoming kinetic energy is 0.015 *a.u.*. The blue paths denote rightward wavepackets and the red paths denote leftward wavepackets. The dash red path for reflection (at potential energy equals 0.005 *a.u.*) signifies that the asymptotic outgoing kinetic energy is 0 *a.u.*.

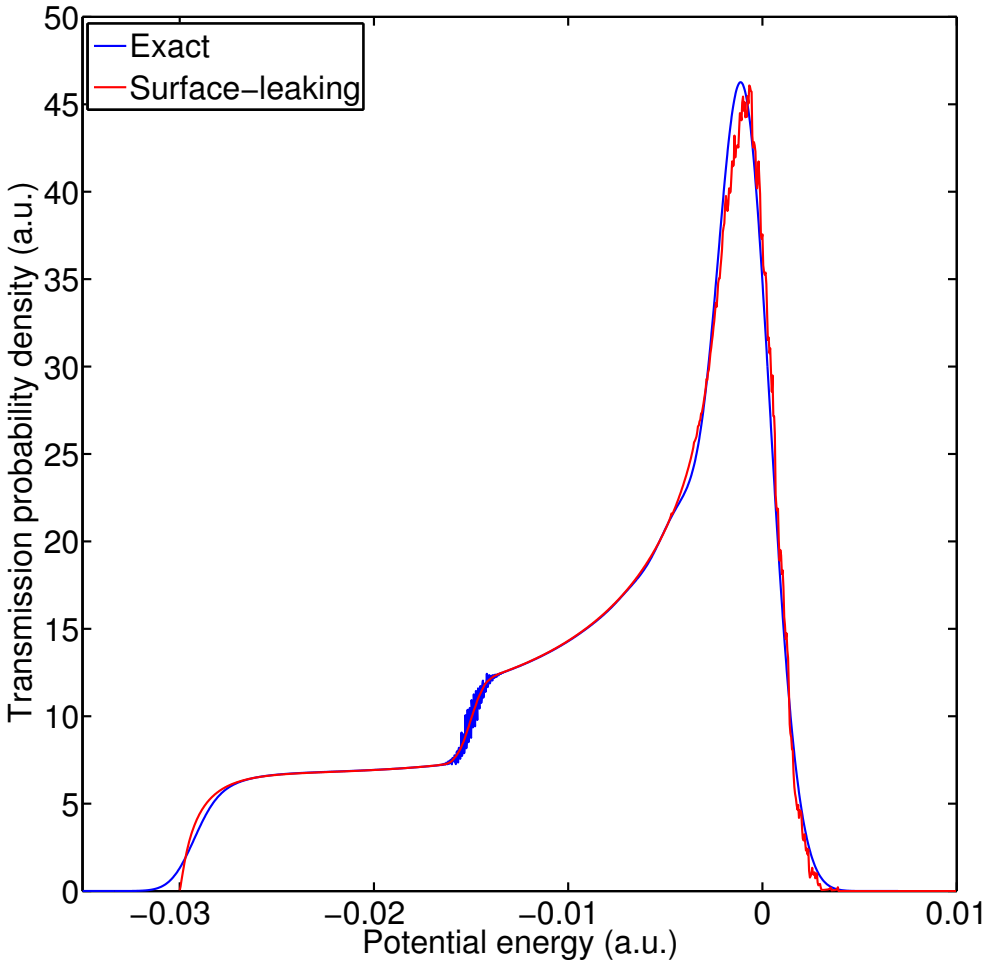

Figure 3.10: Model #1: Transmission probability density for the bath states as a function of potential energy of outgoing channels according to both exact dynamics and surface-leaking algorithm. The incoming kinetic energy for surface-leaking is 0.015 *a.u.*, the mass of nucleus is 100000 *a.u.* and $\Gamma(0)$ is 10^{-4} *a.u.*. Both exact and surface-leaking results are averaged over an incoming Gaussian wavepacket distribution (according to Eq. (3.25) with $\sigma = 1$). Note the good agreement.

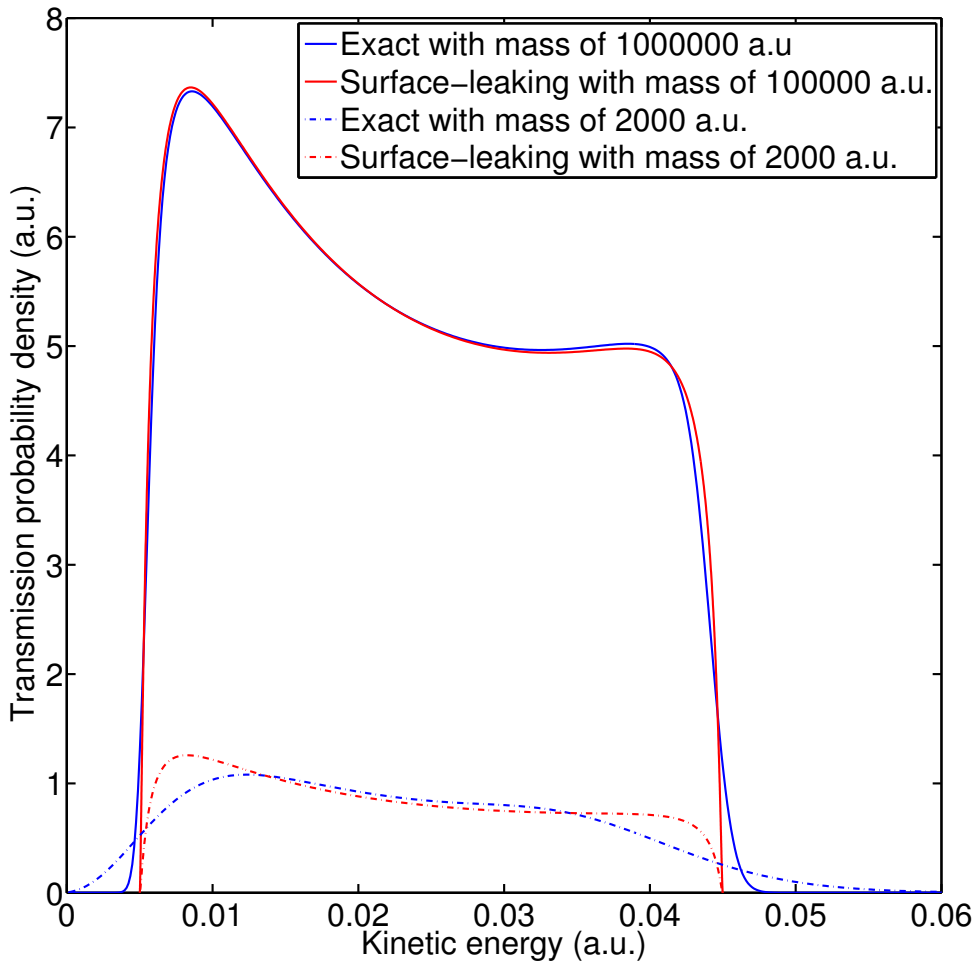

Figure 3.11: Model #1: Transmission probability density for the bath states as a function of outgoing kinetic energy according to exact dynamics and the surface-leaking algorithm. The incoming kinetic energy is 0.025 $a.u.$, $\Gamma(0)$ is 10^{-4} $a.u.$ and the mass of nucleus is 100000 $a.u.$ or 2000 $a.u.$. (For mass equals to 100000 $a.u.$, the data is the same as in Fig. 3.2.) As mass is reduced, surface-leaking results differ more and more from the exact results.

3.4.3 Wide Band Approximation

In all the SL-FSSH simulations above we have assumed that the energy range of the bath is infinite so the relaxation process follows Fermi's Golden Rule with rate Γ. Correspondingly, for the exact dynamics calculations we have always included enough bath states so that the system is completely embedded in a broad bath. While these approximations are useful and lead to simple physics, the wide band approximation is not always true, and it will be interesting to see what happens if we go beyond the wide band approximation.

When the wide band approximation breaks down, Fermi's Golden Rule is no longer valid, and the system does not decay exponentially into the bath. Instead, only a fraction of the system decays into the bath as determined by the projection of the system state into the eigenstates of the Hamiltonian. This projection can be calculated from the imaginary part of the Green's function, also known as the spectral density.

The Green's function can be written as:

$$G(E) = \frac{1}{i\hbar} \lim_{\varepsilon \to 0} \int_0^\infty dt \, \langle \psi(0) | \psi(t) \rangle \exp\left(i(E + i\varepsilon)t/\hbar\right) \tag{3.26}$$

Let the wave function $|\psi(0)\rangle$ be expressed in an adiabatic basis as:

$$|\psi(0)\rangle = \sum_j c_j \, |\phi\rangle \tag{3.27}$$

where c_j are the amplitudes. The Green's function becomes:

$$\begin{aligned} G(E) &= \frac{1}{i\hbar}\lim_{\varepsilon\to 0}\int_0^\infty dt \sum_j |c_j|^2 \exp\left(-iE_j t/\hbar + i(E+i\varepsilon)t/\hbar\right) \\ &= \frac{1}{i\hbar}\lim_{\varepsilon\to 0}\sum_j |c_j|^2 \frac{-\hbar}{i(E-E_j+i\varepsilon)} \\ &= \lim_{\varepsilon\to 0}\sum_j \frac{|c_j|^2}{E-E_j+i\varepsilon} \\ &= \mathrm{PP}\int_{-\infty}^\infty dE' \frac{\rho(E')\,|c(E')|^2}{E-E'} \\ &\quad -i\pi\int_{-\infty}^\infty dE'\rho(E')\,|c(E')|^2\,\delta(E-E') \\ &= \mathrm{PP}\int_{-\infty}^\infty dE' \frac{\rho(E')\,|c(E')|^2}{E-E'} - i\pi\rho(E)\,|c(E)|^2 \end{aligned} \tag{3.28}$$

Here PP means the Cauchy principal value and the following two transformations have been used:

$$\sum_j \to \int dE\rho(E) \tag{3.29}$$

$$\lim_{\varepsilon\to 0}\frac{1}{x+i\varepsilon} \to \mathrm{PP}\,\frac{1}{x} - i\pi\delta(x) \tag{3.30}$$

Thus, the spectral density is

$$\rho(E)\,|c(E)|^2 = \frac{-\,\mathrm{Im}(G(E))}{\pi} \tag{3.31}$$

For a model – with one discrete state (E_0) coupled linearly to a set of bath states – the Green's function is

$$G(E) = \frac{1}{E - E_0 - \sum_k \frac{|V|^2}{E-E_k}} \tag{3.32}$$

The self energy in the above equation can be calculated as:

$$\begin{aligned}\sum_k \frac{|V|^2}{E-E_k} &= \lim_{\varepsilon\to 0}\sum_k \frac{|V|^2}{E-E_k+i\varepsilon} \\ &= \mathrm{PP}\int_{-w}^{w} dE_k \rho(E_k)\frac{|V|^2}{E-E_k} - i\pi\,|V|^2\,\rho(E) \\ &= \frac{\Gamma}{2\pi}\ln\left(\frac{E+w}{w-E}\right) - \frac{i\Gamma}{2} \end{aligned} \tag{3.33}$$

where w is the half width of bath and $\Gamma = 2\pi\rho(E)\,|V|^2$. Thus, the relative proportion of the system state inside of the band is:

$$\begin{aligned} F_{inside} &\equiv -\int_{-w}^{w}\frac{\mathrm{Im}(G(E))}{\pi} \\ &= \frac{1}{\pi}\int_{-w}^{w} dE \frac{2\Gamma}{4\left[E-E_0-\frac{\Gamma}{2\pi}\ln\left(\frac{E+w}{w-E}\right)\right]^2+\Gamma^2} \end{aligned} \tag{3.34}$$

For SL-FSSH, to account for the band width, Eq. (3.15) should be rewritten as:

$$L_i(\mathbf{R}) = \frac{F_{inside}\Gamma_i(\mathbf{R})\Delta t}{\hbar} \tag{3.35}$$

In Fig. 3.12 we plot the transmission probability for system states as a function of bath width for model #2. $\Gamma(0)$ is 10^{-4} *a.u.* and the incoming kinetic energy is 0.2 *a.u.*. We plot exact scattering results with and without the bath states, as well as SL-FSSH. SL-FSSH converges to the exact results in the limit of very wide and very narrow bands. However, in between these two limits, SL-FSSH cannot recover the correct gradual transition; instead SL-FSSH predicts a steep jump. This failure indicates that our approximation for dynamics beyond the wide band limit is still too extreme to be quantitative accurate.

Results for model #3 are shown in Fig. 3.13. $\Gamma(0)$ is 10^{-4} *a.u.* and the incoming

kinetic energy is 0.2 *a.u.*. Just as we saw for model #2, we recover the correct dynamics in the two extreme limits: very wide and very narrow bands. However, for intermediate value of Γ, the agreement between SL-FSSH and exact dynamics is far worse for model #3 than for model #2. This failure can be explained by the length of time (T) spent by the donor system state interacting with the bath. For model #2, the crossing are sharper and T is smaller; for model #3, the bath follows the donor state and T is large. In the future, model #3 will be a good test case for benchmarking an improved SL-FSSH scheme that goes beyond the wide band limit.

3.5 Conclusion

In this paper, we have proposed a simple surface-leaking fewest-switches surface hopping (SL-FSSH) algorithm that combines Tully's FSSH and Preston's SL algorithms. We have benchmarked SL-FSSH on three similar but different system-bath model problems with various parameters. By comparing SL-FSSH results versus exact scattering quantum calculations, we have shown that the algorithm works well over a wide range of nuclear velocities and system-bath coupling strengths in the wide band limit. When we go beyond the wide band approximation, we find only partial success and further improvements to the algorithm will be needed in order to recover the details of the transition between a wide and narrow band of bath states. Corrections should be possible in the future. Considering the low cost of the SL-FSSH algorithm, the prevalence of wide bands, and the ubiquitousness of both relaxation and short-time coherent non-adiabatic processes, SL-FSSH should be useful in a wide variety of applications. In particular, one obvious application would be molecular processes on weakly coupled metal surfaces[139].

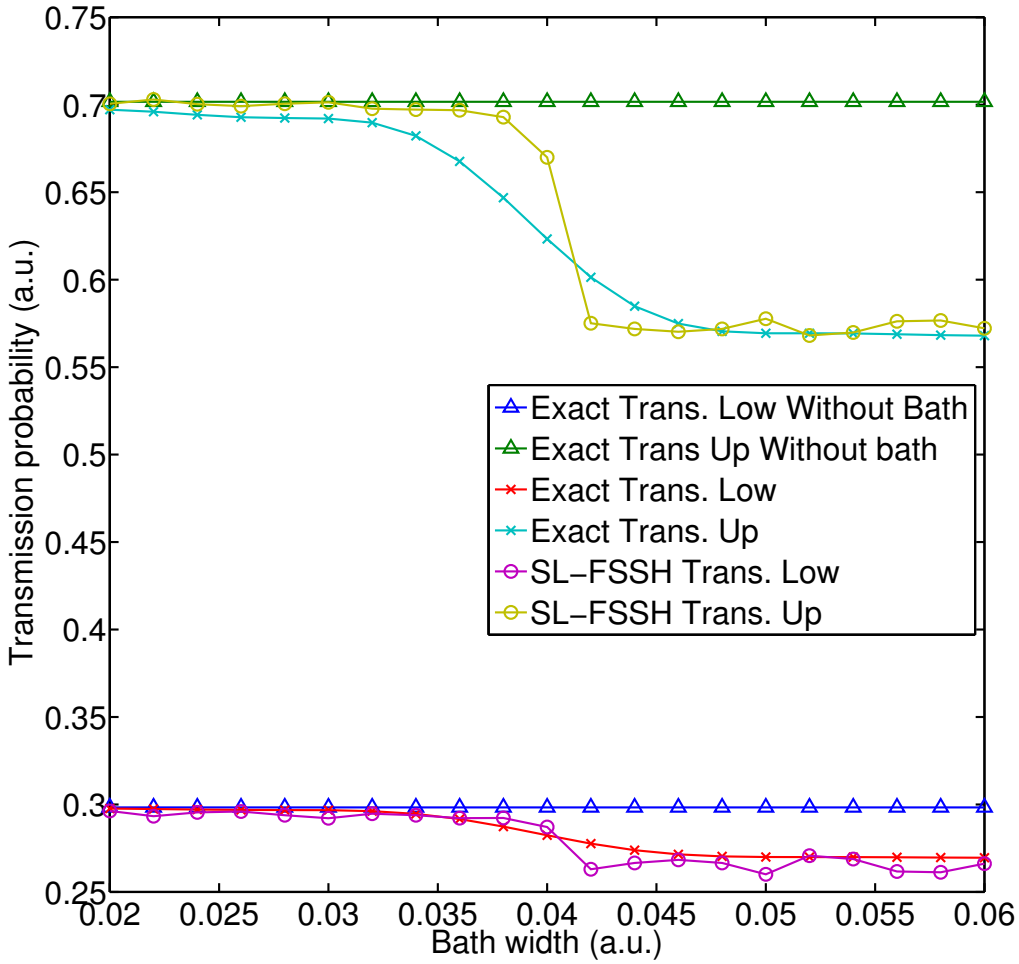

Figure 3.12: Model #2: Transmission results for the system channels as a function of bath width. The incoming kinetic energy is 0.2 $a.u.$, the nuclear mass is 2000 $a.u.$ and $\Gamma(0)$ is 10^{-4} $a.u.$. SL-FSSH results are averaged over 40000 trajectories. Note that SL-FSSH agrees with exact dynamics in the limit of very wide and very narrow band, but the crossover is not quantitative at all.

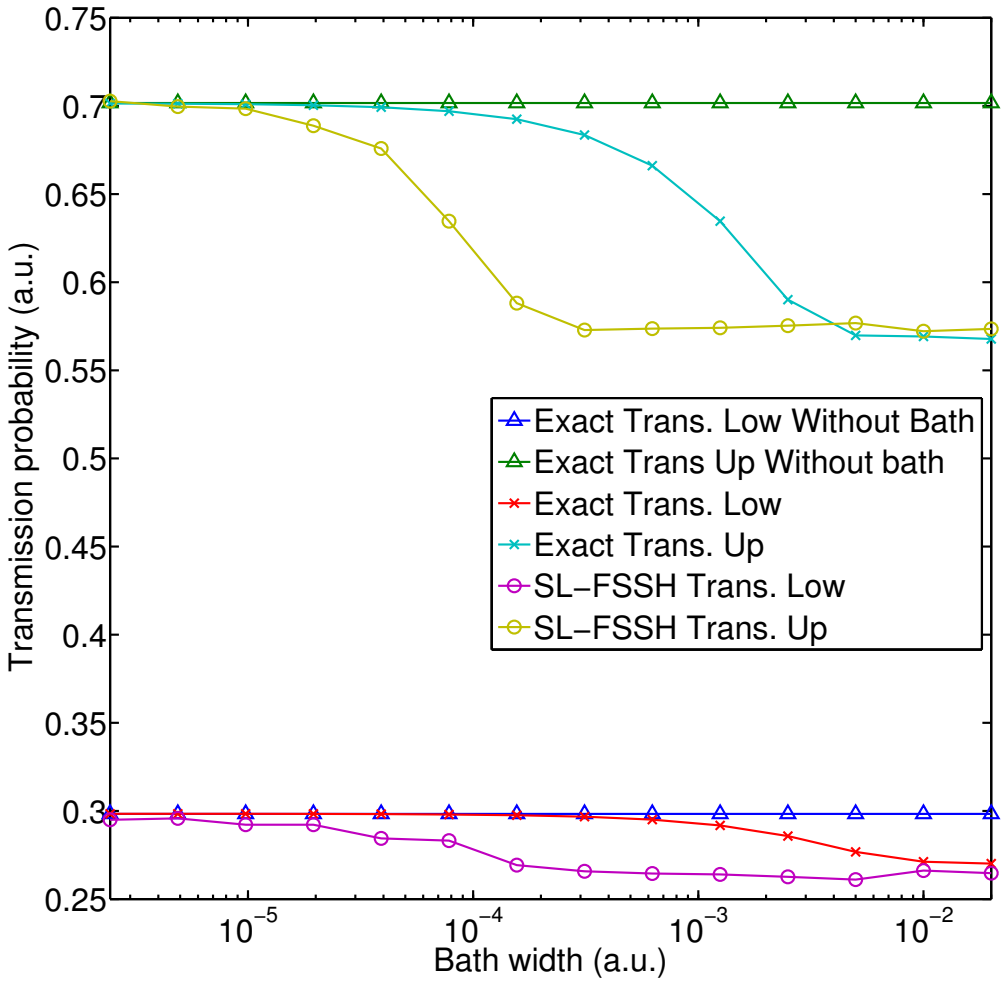

Figure 3.13: Model #3: Transmission results for the system channels as a function of bath width. The incoming kinetic energy is 0.2 $a.u.$, the nuclear mass is 2000 $a.u.$ and $\Gamma(0)$ is 10^{-4} $a.u.$. SL-FSSH results are averaged over 40000 trajectories. Note that SL-FSSH agrees with exact dynamics in the limit of very wide and very narrow band, but the crossover is not quantitative at all.

3.6 Acknowledgments

This material is based upon work supported by the (U.S.) Air Force Office of Scientific Research (USAFOSR) PECASE award under AFOSR Grant No. FA9950-13-1-0157. J.E.S. acknowledges a Cottrell Research Scholar Fellowship and a David and Lucille Packard Fellowship.

CHAPTER 4

A Surface Hopping View of Electrochemistry: Non-Equilibrium Electronic Transport through an Ionic Solution with a Classical Master Equation

This chapter is adapted from The Journal of Physical Chemistry C, Volume 119, Issue 36, Page 20833-20844, 2015.

4.1 Introduction

The field of electrochemistry is an area of physical chemistry where the theoretical tools are unfortunately limited. By its very nature, electrochemistry is difficult to model atomistically: one must treat the nuclear motion of solute and solvent molecules (including mass transport over long distances), the electronic and nuclear dynamics of the metal electrode, and electron transfer at the electrode interface. As such, simulating electrochemistry is difficult[140]. That being said, the field of electrochemistry touches upon so many interesting phenomena–corrosion, battery lifetimes, aluminum production, biosensors, fuel cells, etc.–that it is worthwhile developing new and approximate theoretical tools.

In practice, for our purposes, it is convenient to consider electrochemistry as the combination of two different phenomena. First, in many electrochemistry experiments, chemical reactions occur at a metal electrode; some covalent bonds are broken, some are created. Second, at an electrochemical interface, there will be electron transfer between a metal electrode and a molecular species in solution. And this electron transfer can come in different flavors: either outer sphere electron trans-

fer (where metal-molecule coupling is weak) or inner sphere electron transfer (where metal-molecule coupling is strong). Below, we will focus mostly on outer sphere electron transfer; we will only briefly discuss the role of breaking/making bonds in Sec. 4.5.2.

Our goal in the present paper is to model the solution-phase flow of electrons through a simple electrochemical setup. See Fig. 4.1. In particular, we want to model the following three steps: (*i*) electrons hop from one metal electrode surface (cathode on the right) onto solute charge carriers in solution, (*ii*) charged ions drift through an ambient liquid, (*iii*) electrons leave the solute charge carriers and hop onto a metal electrode surface (anode on the left), thus completing a cycle of reduction and oxidation of the charge carrier. From the point of view of physical chemistry, most research in electrochemistry has traditionally focused on the statistical mechanics of the ions near the electrode interface (screening, e.g.[141]) rather than dynamics. In this paper, our main focus is on treating the quantum processes in step (*i*) and (*iii*).

To achieve this goal of explicitly addressing charge injection, we will run dynamics on a fluctuating stochastic potential. Consider a molecule that can be either charged or uncharged near a wide-band metal[142]. Without loss of generality, we assume the charge-carrier molecule starts off neutral (at time 0) and we run classical dynamics for the neutral molecule for some period of initialization time. Thereafter, we allow stochastic changes in the charge state of the molecule, which will in turn change the molecule's local environment and vibrational frequencies. The details of when we change charge states are described below (and in Ref. 42).

From the perspective of chemistry, the stochastic algorithm just described can be considered a member of the surface hopping family, in the same spirit as the original Tully algorithm.[13] However, whereas the original Tully algorithm was applied to systems with only a few electronic states, the present algorithm concerns surface

hopping with a continuum of electronic states. As such, there are key distinctions between the two surface hopping algorithms.

- Tully's surface hopping algorithm (e.g. for two states) propagates classical nuclei along adiabatic surfaces while keeping track of the electronic coherences with an auxiliary set of amplitudes. Electronic hops are accompanied by momentum adjustments to maintain energy conservation and, for accuracy, electronic decoherence must be included on top of the Tully scheme[20,23–40,129].

- The present algorithm for many states propagates nuclei along diabatic potential energy surfaces corresponding to different charge states of the molecule and does not propagate any electronic coherence at all (because we assume the wide band limit for the metal surface). According to the present algorithm, individual trajectories do not maintain energy conservation and there are no momentum adjustments.

Nevertheless, despite these differences, both the Tully and the present approach follow the same rules roughly: classical nuclear motion along static (not mean-field) potential energy surfaces with hops between surfaces to account for nonadiabatic relaxation. Furthermore, both approaches recover detailed balance, either approximately (in the case of the Tully algorithm[71,72]) or exactly (in the case of the present algorithm). In practice, the need to go beyond Tully's original algorithm is dictated only by computational cost: running Tully dynamics over a continuum of adiabatic electronic states would be astronomically expensive (though approximations can be made[43–45]). This statement about computational cost would be true for most other quantum or mixed quantum-classical methods[1–12] if they treat the electronic bath explicitly. In short, the present many-body version of surface hopping was designed to treat an open quantum system with minimal cost.

Now, from the perspective of molecular conduction, the many-body surface hopping algorithm just described can be (and was) derived[143] in a straightforward fashion by (*i*) assuming the metal-molecule coupling is small (in the spirit of outer-sphere electrochemistry) which leads to a master equation, and (*ii*) assuming the temperature is large enough that all nuclear motion can be considered classical. Thus, our surface hopping algorithm can be considered a "classical master equation", which guarantees that the method evolves to recover the correct equilibrium distribution. Naturally, this approach should be valid in the limit of outer sphere electrochemistry, i.e. electron transfer between a metal surface and molecules that are close by, but not covalently attached[42]. Given the interdisciplinary nature of electrochemistry, it is perhaps not surprising that simple techniques in one area of physics (molecular conduction through molecules) will be useful in a very different area of chemistry (solution-phase charge carrier transport). After all, there is a long history of non-equilibrium chemical dynamics in statistical physics[144,145].

Interestingly, recently Voth and co-workers[146,147] performed related non-equilibrium simulations to capture the flow of ions through a solution of electrolytes across a voltage. The algorithm in the present paper can effectively be considered an atomistic version of the Voth coarse-grained scheme in Refs. 146,147 which evaluates hopping probabilities with an averaged Marcus rate and does not allow back transfer. The method proposed herein explicitly allows back electron transfer and uses an atomistic electron transfer rate while assuming no averaging of the transfer rate. While Voth *et al* treat the problem of the image charge properly, in the present paper, we treat the effect of the image charge only heuristically–just enough to ensure that we extract the proper physics.

Finally, our aim is to study ionic conduction. Our plan of attack is as follows. We consider a liquid made up of solvent and redox-active solute atoms. We will simu-

late the ionic current through the liquid using both fully non-equilibrium molecular dynamics and a combination of equilibrium dynamics with chemical kinetics. We will investigate how and when the latter matches the former. Our paper is organized as follows. Section 4.2 defines our model Hamiltonian, outlines the details of our non-equilibrium algorithm, and reviews the working equations for estimating current with linear response. Section 4.3 provides all the necessary atomistic details about our simulation. Section 4.4 analyzes our simulation results and makes a comparison between non-equilibrium and equilibrium dynamics. Section 4.5 separates mass transport versus electron transfer contributions to the final current. Section 4.6 concludes the paper.

4.2 Theory

For the notation we let q be the charge of an ion and e be the charge of an electron, so that q/e is dimensionless.

4.2.1 The Model Hamiltonian

Our model system is a slab system consisting of two parallel plane electrodes separated in the z direction. Periodic boundary conditions are applied in the x and y directions (not z). We consider two classes of atoms: solvent atoms ("A") and charge carrier solute atoms ("B"). The total Hamiltonian of the system is the following:

$$H(\mathbf{r}^{(A)}, \mathbf{r}^{(B)}, \mathbf{v}^{(A)}, \mathbf{v}^{(B)}, q^{(B)}) \equiv E_k + U_{AA} + U_{AB} + U_{BB} + U_{electrode} + U_{field} + U_{atomic} \quad (4.1)$$

where E_k is the total kinetic energy, $\mathbf{r}$ and $\mathbf{v}$ are the sets of 3D coordinates and velocities of a particular atom type, and q is the charge on B atoms. A schematic figure of the system is shown in Fig. 4.1 where we also indicate the pairwise interactions

and the hybridization function for electron transfer.

A-A and A-B Interactions

Since the A atoms are neutral, the A-A and A-B interactions are chosen to be simple Lennard-Jones interactions whether B is neutral or charged:

$$U_{AA} = \sum_{i<j} 4\varepsilon_{AA} \left[\left(\frac{\sigma_{AA}}{\left| \mathbf{r}_i^{(A)} - \mathbf{r}_j^{(A)} \right|} \right)^{12} - \left(\frac{\sigma_{AA}}{\left| \mathbf{r}_i^{(A)} - \mathbf{r}_j^{(A)} \right|} \right)^{6} \right] \tag{4.2}$$

$$U_{AB} = \sum_{i<j} 4\varepsilon_{AB} \left[\left(\frac{\sigma_{AB}}{\left| \mathbf{r}_i^{(A)} - \mathbf{r}_j^{(B)} \right|} \right)^{12} - \left(\frac{\sigma_{AB}}{\left| \mathbf{r}_i^{(A)} - \mathbf{r}_j^{(B)} \right|} \right)^{6} \right] \tag{4.3}$$

where $\mathbf{r}_i^{(A)}$ and $\mathbf{r}_j^{(B)}$ are the coordinates of A and B atoms labeled i and j. The sum in each case is restricted to A-A and A-B pairs. For simplicity in this study, we assume that A and B are identical with respect to these interactions: $\varepsilon_{AA} = \varepsilon_{AB} = \varepsilon$ and $\sigma_{AA} = \sigma_{AB} = \sigma$. For simplicity of notation, we define the pair potential U_{LJ}:

$$U_{LJ}(r) = 4\varepsilon \left[\left(\frac{\sigma}{r} \right)^{12} - \left(\frac{\sigma}{r} \right)^{6} \right] \tag{4.4}$$

Here ε and σ are the Lennard-Jones constants.

B-B Interaction

A solute (B) atom can be charged or neutral. Let q_i and q_j be the charges on two atoms. The B-B interaction is defined as a Lennard-Jones interaction plus a Coulomb interaction.

$$U_{BB} = \sum_{i<j} U_{BB} \left(\mathbf{r}_i^{(B)}, \mathbf{r}_j^{(B)} \right) \tag{4.5}$$

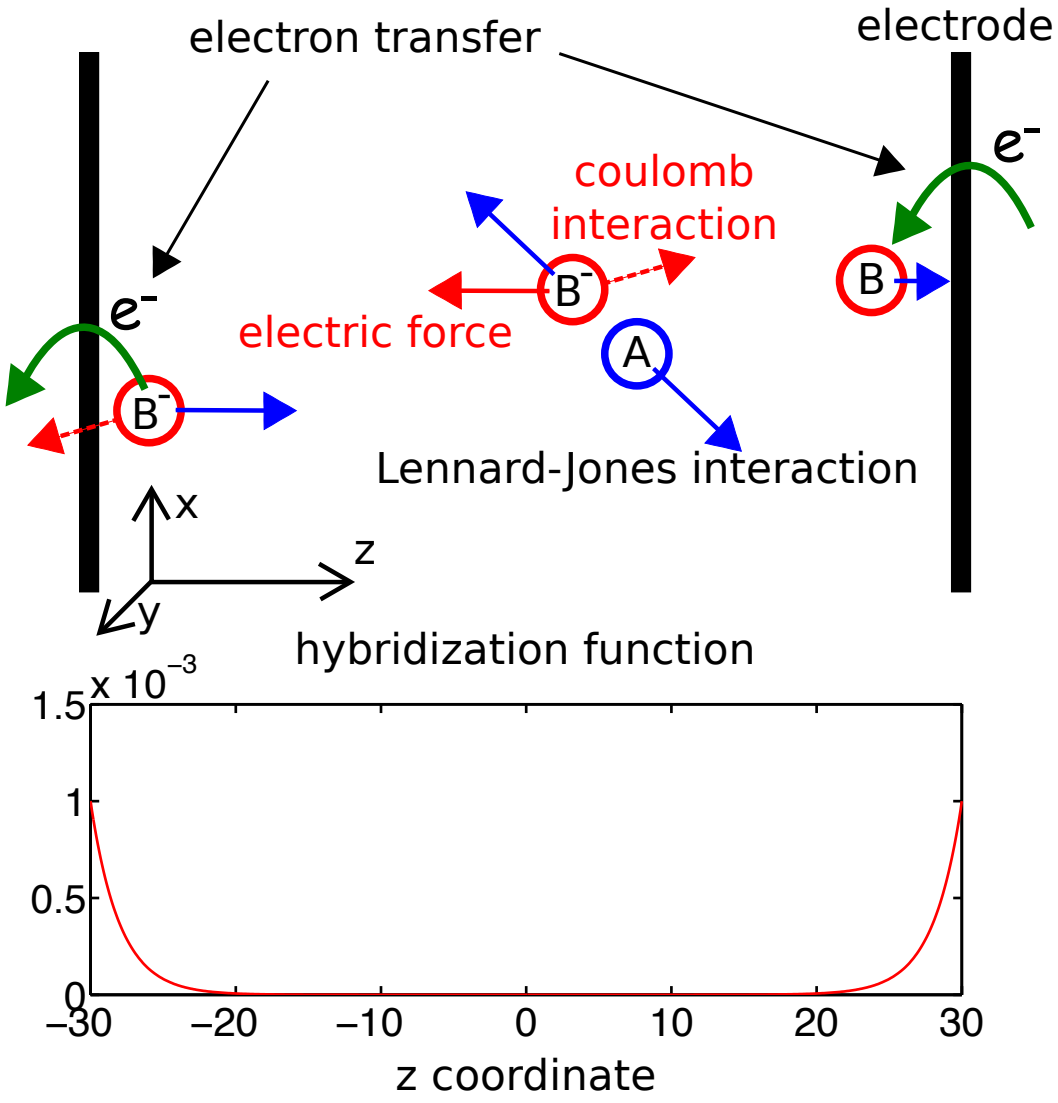

Figure 4.1: (Top) A schematic picture of our system. The blue open circles labeled "A" denote solvent atoms and the red open circles labeled "B" or "B$^-$" denotes solute atoms. Solute atoms can be neutral ("B") or charged ("B$^-$"). The Lennard-Jones interaction is shown with blue arrows, the electric force due to the electric field is represented by a red arrow, and the long-range Coulomb interactions between charged B$^-$ atoms is shown with dashed red arrows. The direction of electron transfer is illustrated with a curved green arrow. (Bottom) The electronic hybridization function as a function of z (which is also known as the electronic broadening, $\Gamma(z)/h$; see Eq. (4.11)).

$$U_{BB}\left(\mathbf{r}_i^{(B)}, \mathbf{r}_j^{(B)}\right) \equiv U_{LJ}\left(\left|\mathbf{r}_i^{(B)} - \mathbf{r}_j^{(B)}\right|\right) + \frac{q_i q_j}{4\pi\epsilon\left|\mathbf{r}_i^{(B)} - \mathbf{r}_j^{(B)}\right|} \tag{4.6}$$

Here ϵ is the permittivity. Note that if one or both of the solute atoms is neutral, $U_{BB} = U_{LJ}$.

Electrode-A and Electrode-B Interactions

We represent each electrode as a simple planar surface with respect to its interactions with the atoms in the liquid. The interaction between electrodes and an A atom or a B atom is a Lennard-Jones interaction defined above in Eq. (4.4). If $z^{(L)}$ is the z-coordinate for the left electrode, $U_{electrode}^{(LA)}\left(\mathbf{r}^{(A)}\right) \equiv U_{LJ}\left(\left|z^{(A)} - z^{(L)}\right|\right)$. All other atom-electrode potentials are defined analogously.

Interaction with External Electric Field

The relationship between the voltage (V) and the electrochemical potential (μ) of the left (L) and right (R) electrodes is defined as:

$$V_L \equiv \frac{\mu_L}{e}, V_R \equiv \frac{\mu_R}{e}, V \equiv V_L - V_R \tag{4.7}$$

where e is the electron charge (negative). The external electric field can be calculated from the voltage between the two electrodes:

$$\mathcal{E} \equiv \frac{V}{L_z} = \frac{V_L - V_R}{L_z} = \frac{\mu_L - \mu_R}{eL_z} \tag{4.8}$$

where L_z is the distance between the two electrodes. When the voltages V_L and V_R at the two electrodes are different–or equivalently the electrochemical potentials for electrons μ_L and μ_R differ–the applied electric field will interact with charged B^-

atoms. The potential energy due to the electric field is:

$$U_{field} = \sum_i U_{field}\left(z_i^{(B)}\right) \equiv \sum_i \left(\mu_L + \frac{\mu_R - \mu_L}{L_z}\left(z_i^{(B)} - z^{(L)}\right)\right)\frac{q_i}{e} \qquad (4.9)$$

Electron Affinity

The electron affinity energy is included in the term U_{atomic} in Eq. (4.1). Note that we do not include ionization energy in Eq. (4.1) because we do not have a positive charge carrier in our system for simplicity. In the future, it will be interesting to have two types of charge carriers, negative and positive.

4.2.2 Boundary Conditions and Electron Transfer

Let us now discuss the boundary conditions at the electrode, where B atoms can accept charge from the metal and B^- can donate a charge to the metal. Our approach will be based on the classical master equation and surface hopping dynamics presented in Refs. 42,143. The model is very simple: if the i^{th} solute atom (B_i) accepts an electron (making B_i^-), then the charge q_i changes from 0 to e in Eq. (4.6) and Eq. (4.9) and the system evolves accordingly. Vice versa, if the i^{th} solute atom (B_i^-) donates an electron (making B_i), then the charge q_i changes from e to 0.

The probability for a neutral solute atom (B) to accept an electron from the left metal is:

$$\zeta_{accept}(\Delta z_L, \Delta H) = dt\frac{\Gamma(\Delta z_L)}{\hbar}\frac{1}{1+\exp(\beta(\Delta H - \mu_L q/e))} \qquad (4.10)$$

where dt is the time span in which electron transfer is considered, Δz_L is the absolute distance between the atom and the left electrode, $\beta = 1/(k_b T)$. For the electron transfer probability for the right electrode, one substitutes R for L. $\Gamma(z)$ is the

position dependent hybridization function defined as:

$$\Gamma(z) = \Gamma_0 \exp(-z/\lambda). \tag{4.11}$$

The parameter Γ_0 denotes the strength of coupling when the solute sits at the metal surface, and λ is the decay parameter for the coupling in space (also known as β^{-1} for electron transfer in molecules[142]). ΔH is the change in energy (see Eq. (4.1)) after the charge is accepted, to which we add the effect of a new image charge:

$$\begin{aligned} \Delta H &= H(\mathbf{r}, \mathbf{v}, q_1, q_2, \cdots, q_i = e, \cdots, q_{N_B}) - H(\mathbf{r}, \mathbf{v}, q_1, q_2, \cdots, q_i = 0, \cdots, q_{N_B}) \\ &\quad + \Delta U_{image} \end{aligned} \tag{4.12}$$

ΔU_{image} must be included in Eq. (4.12) because image charges in the metal will adjust very quickly to the appearance of a B^- atom, and the effect of such an image charge need not be small if a B^- atom is close to an electrode. In truth, an optimal algorithm should actually evaluate all image charges (corresponding to all charged B^- atoms) at every time step as part of the Hamiltonian (Eq. (4.1))–not just when a B atom approaches a surface and accepts a charge. Calculating the locations and fields of all image charges (on both conducting electrodes) is possible[148] and has been achieved by Voth *et al*[146]. For now, though, and for the sake of simplicity, we presume that image charge effects will be significant only near the electrode surface and we include such effects only through Eq. (4.12).[3] Thus, for example, when B accepts a charge from the left electrode, to first order, we assume

$$\Delta U_{image} = \mu_L \frac{-q}{e} \tag{4.13}$$

[3]In practice, the reader will note that, if we do not include image charges, then Eq. (4.10) strikingly becomes independent of the electrochemical potentials, μ_L and μ_R, which is completely unphysical.

To complete the story, the probability for a charge B^- to donate an electron to the left electrode is completely analogous to Eq. (4.10):

$$\begin{aligned}\zeta_{donate}(\Delta z_L, \Delta H) &= dt\frac{\Gamma(\Delta z_L)}{\hbar}\left(1 - \frac{1}{1+\exp(\beta(\Delta H - \mu_L q/e))}\right) \\ &= dt\frac{\Gamma(\Delta z_L)}{\hbar}\frac{1}{1+\exp(\beta(\mu_L q/e - \Delta H))}\end{aligned} \tag{4.14}$$

and similarly for the right electrode.

Finally, we make one comment on periodicity in the x and y directions. In principle, we should use fully two-dimensional periodic boundary conditions in the x, y directions to eliminate spurious wall effects where there is no electrode. That being said, in practice, simulating 2D periodic boundary conditions for long-range Coulombic interactions (that cannot be truncated) in a charged box is tedious; Ewald summation in two dimensions with a charged unit cell is possible but not trivial[149–152]. Thus, for this paper, we will take a short-cut and calculate the direct Coulomb interaction only between a given atom and the closest periodic image of another atom (the minimum image convention[153]); this prescription should be accurate enough with only a few charged particles present simultaneously in the system.

4.2.3 Algorithm

A step-by-step outline of our simulation algorithm is as follows:

1. Initialize the model system.
   (a) Initialize for each atom its position ($\mathbf{r}_i$), velocity ($\mathbf{v}_i$), charge (q_i), atomic mass (m_i) and Lennard-Jones constants (σ and ε).
   (b) Fix the value of the electrochemical potentials μ_L and μ_R.

2. Propagate each atom and a Nosé thermostat[154] using the velocity Verlet algorithm[155].

   The forces are obtained by calculating the negative gradient of the total Hamiltonian in Eq. (4.1):

$$F(\mathbf{r}) = -\nabla_{\mathbf{r}} H \tag{4.15}$$

3. Evaluate the probability for electron transfer between the electrodes and a charge carrier. Loop over all charge carriers (i.e. B atoms):

   (a) Calculate ΔH with Eq. (4.12).

   (b) If B is charged, use Eq. (4.14) to calculate the probability $\zeta^{(L)}_{donate}$ for charge donation ($B^- \rightarrow$B) to the left electrode (and the analogous probability for the right electrode $\zeta^{(R)}_{donate}$).

   Generate a random number g sampled from $[0, 1]$. If $g < \zeta^{(L)}_{donate}$, B^- donates the electron to the left electrode. Otherwise if $g < \zeta^{(L)}_{donate} + \zeta^{(R)}_{donate}$, B^- donates the electron to the right electrode. Go to step 3d.

   (c) If B is neutral, use Eq. (4.10) to calculate the probability $\zeta^{(L)}_{accept}$ for charge acceptance (B$\rightarrow$ B^-) from the left electrode (and the analogous probability for the right electrode $\zeta^{(R)}_{accept}$).

   Generate a random number g sampled from $[0, 1]$. If $g < \zeta^{(L)}_{accept}$, B accepts the electron from the left electrode. Otherwise if $g < \zeta^{(L)}_{accept} + \zeta^{(R)}_{accept}$, B accepts the electron from the right electrode. Go to step 3d.

   (d) If an electron transfer event occurs, update the charges as used in Eq. (4.1) and Eq. (4.15).

4. Continue to step 2.

4.2.4 Linear Response Theory

With equal electrochemical potentials on both left and right electrodes (i.e. no voltage, $V = 0$), the methodology just described is essentially a sampling of the grand canonical ensemble for charge carrier species B and B^- [156]. The only nuance here is that, in the course of a Monte-Carlo simulation, we add/subtract charges according to a position dependent criteria based on $\Gamma(z)$–whereas the insertion rate is usually treated as a constant [156]. That being said, many interesting phenomena appear when we have different electrochemical potentials on two electrodes (e.g., a current).

Within the context of equilibrium statistical mechanics, linear response theory (and specifically the Green-Kubo relation) is a powerful tool for estimating the conductivity of the system. According to linear response, if we denote the perturbation to the equilibrium system as $H_1 = \mathcal{E}qz$, then to first order of βH_1, the response of the system is proportional to the time integral of the velocity autocorrelation function as calculated from an equilibrium simulation. The mobility u is then calculated to be [142]:

$$u = \beta \int_0^\infty dt \, \langle v_z(0) v_z(t) \rangle = \frac{\beta}{3} \int_0^\infty dt \, \langle \mathbf{v}(0) \cdot \mathbf{v}(t) \rangle \tag{4.16}$$

More generally, if we define the current density $\mathbf{J}$

$$\mathbf{J}(\mathbf{r}, t) = \frac{q \sum_j \mathbf{v}_j(t) \delta(\mathbf{r} - \mathbf{r}_j)}{V}, \tag{4.17}$$

where V is the volume of the system, Eq. (4.16) becomes the Green-Kubo expression for conductivity:

$$\sigma_c = \frac{\beta}{3} \int d\mathbf{r} \int_0^\infty dt \, \langle \mathbf{J}(0,0) \cdot \mathbf{J}(\mathbf{r}, t) \rangle \tag{4.18}$$

In practice, below we would like to compare (i) the current as calculated with our non-equilibrium surface hopping approach versus (ii) the current as calculated

with linear response. To make this comparison, we have calculated and integrated the velocity-velocity correlation function in Eq. (4.16).[4]

With this in mind, the conductance ($G = I/V$, the inverse of resistance) is calculated as follows. First, we calculate the conductivity:

$$\langle J_z \rangle = \sigma_c \mathcal{E}_z = \rho_q e \langle v_z \rangle = \rho_q e^2 u \mathcal{E}_z \tag{4.19}$$

$$\implies \sigma_c = \rho_q u e^2 \tag{4.20}$$

where ρ_q is the density of B^- atoms, $\mathcal{E}_z = \mathcal{E}$ is the electric field and u is the mobility defined in Eq. (4.16). Second, the conductance of our system:

$$G = \sigma_c \frac{S_{xy}}{L_z} = \rho_q u e^2 \frac{S_{xy}}{L_z} = u e^2 \frac{N_q}{\mathcal{V}} \frac{S_{xy}}{L_z} \tag{4.21}$$

where S_{xy} is the cross-sectional area in xy plane of our system. Here $\rho_q \equiv N_q/\mathcal{V}$. N_q is the total number of B^- atoms in the system and $\mathcal{V}$ is the effective volume of the system ($\mathcal{V} < V$):

$$\mathcal{V} = S_{xy} L_z^{(eff)} \tag{4.22}$$

$L_z^{(eff)}$ is the system's effective length in the z-direction. Because of the repulsion

[4]There are two subtleties that are worth comment. First, as is well known, the velocity-velocity correlation function decays slowly (non-exponentially) and tails can be important [157,158]. In the context of our calculation–with a fixed box size in the z-direction–it is crucial to use the velocity-velocity correlation function in the unconstrained x, y directions for Eq. (4.16). Otherwise, anomalies will appear when the particles reach the box edge. Second, when evaluating the dynamics for the velocity-velocity correlation function, we will ignore Coulomb repulsion between charged B^- atoms. Our reasons are practical and twofold: (a) at any time, we never have more than 5 or 6 charged B^- atoms and usually fewer than 4[5]; (b) without periodic boundary conditions, as discussed above, the tails of the velocity-velocity correlation functions will be highly distorted in a confined box where, with Coulomb interactions, charged particles will inevitably repel one another at long times. By rerunning the entire simulation without any Coulombic repulsion at all, we have checked numerically that this neglect of Coulombic forces does not affect the conclusions of our paper regarding linear response.

[5]This information can be found in the Supporting Information

between atoms and electrodes at short distances (according to a Lennard-Jones potential), we should expect $L_z^{(eff)} < L_z$, where L_z is the total distance between two electrodes. In practice, $L_z^{(eff)}$ is calculated by measuring the distance between the two peaks closest to the left and right electrodes in Fig. 4.5(a).

In the end, Eq. (4.21) leads to:

$$G = \frac{ue^2 N_q}{L_z L_z^{(eff)}}, I = G \cdot V \tag{4.23}$$

Eq. (4.23) will be used below to estimate the current of our system according to linear response theory.

4.3 Atomistic Details

For our simulation cell, the two electrodes extend along the xy plane between $z = \pm 30$Å, and the cell length is 20Å in both the x and y directions. Between the electrodes, there are 490 "argon" (A) atoms and the charge carriers are modeled by 14 "fluorine" (B) atoms. For the sake of simplicity, all atoms share the same Lennard-Jones constants as those of argon atom: $\sigma = 3.405$Å and $\varepsilon = 0.2379$ kcal/mol (see Eq. (4.4)). The mass of the A atoms is 39.948 amu and the mass of the B atoms is 18.998 amu. For computational convenience, we use the minimum image convention[153] for both Coulomb and Leonard Jones interactions, whereby each atom interacts with only one (i.e. the closest) of the periodic images of another atom. For simplicity, we truncate all Lennard-Jones interactions at 8.5Å in Eq. (4.1). For the Coulomb interaction between B^- atoms, the permittivity is set as $\epsilon = 80\epsilon_0$, i.e. water. Our system is thermostatted[154] at 300K. For the electron transfer, the strength of electronic coupling is chosen such that the largest transferring rate is $\Gamma_0/\hbar = 0.001$/fs for the definition of hybridization function, and $\lambda = 2$Å. The electron affinity of the B

atoms is 3.4011895eV[159] (U_{atomic} in Eq. (4.1)). Before activating any external electric field or electron transfer, our system is evolved (at 300K) for 1ns. We gather statistics from 100 trajectories of length 4ns.

The electrochemical potential of the right electrode is fixed at -3.4000000eV which is close to the electron affinity of the fluorine charge carriers (i.e. the B atoms); with this choice of electrochemical potential, there should be neither too many nor too few charged B^- atoms in the system. To simulate a change in voltage as applied to the system, we change only the electrochemical potential of the left electrode. We restrict ourselves to the nonresonant case that the electrochemical potential of the left electrode should be less than or equal to the electrochemical potential of the right electrode; thus, the electric field always points to the right (and electrons drift to the left). See the inset in Fig. 4.3. [6]

4.4 Results

We now analyze the model above exhaustively.

[6]Readers will notice that, while we observe plateauing in Fig. 4.3, Ref. 146 by Voth *et al.* predicts that the linear relationship between current and applied voltage extends to quite a high voltage (without plateauing). These two findings are not contradictory. The subtlety here is the way in which one applies the external (i.e. source-drain) voltage across the electrochemical cell. In Ref. 146, the voltage is applied such that the left electrode has potential of $+V/2$ and the right electrode has potential of $-V/2$. In other words, as the source-drain voltage is increased, the potential of the left electrode is raised and the potential of the right electrode is decreased, so that for the large voltage, the current will proceed resonantly. In such a resonant regime, the average number of charged atoms should only increase with voltage. A picture of the relevant chemical potentials in Ref. 146 is shown in the supporting information. By contrast, as shown in the inset of Fig. 4.3, we apply the external source-drain voltage differently (with one particular gate voltage). We simulate the external source-drain voltage by decreasing the electrochemical potential on only the left electrode. For our system (as indicated in Fig. 4.4), the average number of charged atoms decreases when the voltage increases, which leads to plateauing in our I-V curves at high voltage in Fig. 4.3, rather than a linearly increasing current (as found in Ref. 146). In a subsequent paper, we will consider the resonant case.

4.4.1 I-V Curve

In Fig. 4.2 we plot the cumulative net electron transfer count as a function of time for 0.05V. The blue and red curves are the cumulative count of net electron transfer into the left electrode and out of the right electrode, respectively. The steady-state current is the average slope of the curves at long time (i.e. after 1ns). The difference between the two curves in Fig. 4.2 is simply the average net charge of the system as a function of time. (Note that, at time 0, the system starts off charge neutral.)

The I-V data is shown in Fig. 4.3. The solid curve with cross markers is data from our non-equilibrium simulation. While the overall curve is not linear, we do find a linear I-V relationship for small voltages. To better understand this linear regime, we compare our simulation data versus the linear response prediction. To evaluate Eq. (4.23), we must first calculate N_q (the total number of charged solute atoms in the system) and $L_z^{(eff)}$ (the effective length of the box in the z direction).

- The average net charge of the system (N_q) can be calculated easily by measuring the difference between the two curves in Fig. 4.2, assuming that the system starts off (at $t = 0$) with no charge.

- To estimate $L_z^{(eff)}$, we use the distance between the two major peaks in the position distribution for electron transfer, which is 53.2Å. More details about these peaks in the electron transfer position distribution will be discussed in Sec. 4.4.3.

In Fig. 4.3, we plot two different versions of the linear response current (Eq. (4.23)). First, we plot the estimated current evaluated with the correct, steady-state non-equilibrium number of charged B^- atoms ($N_q(V)$) as in Fig. 4.4; this plot recovers the basic plateauing of the I-V curve. Second, we plot the estimated current assuming

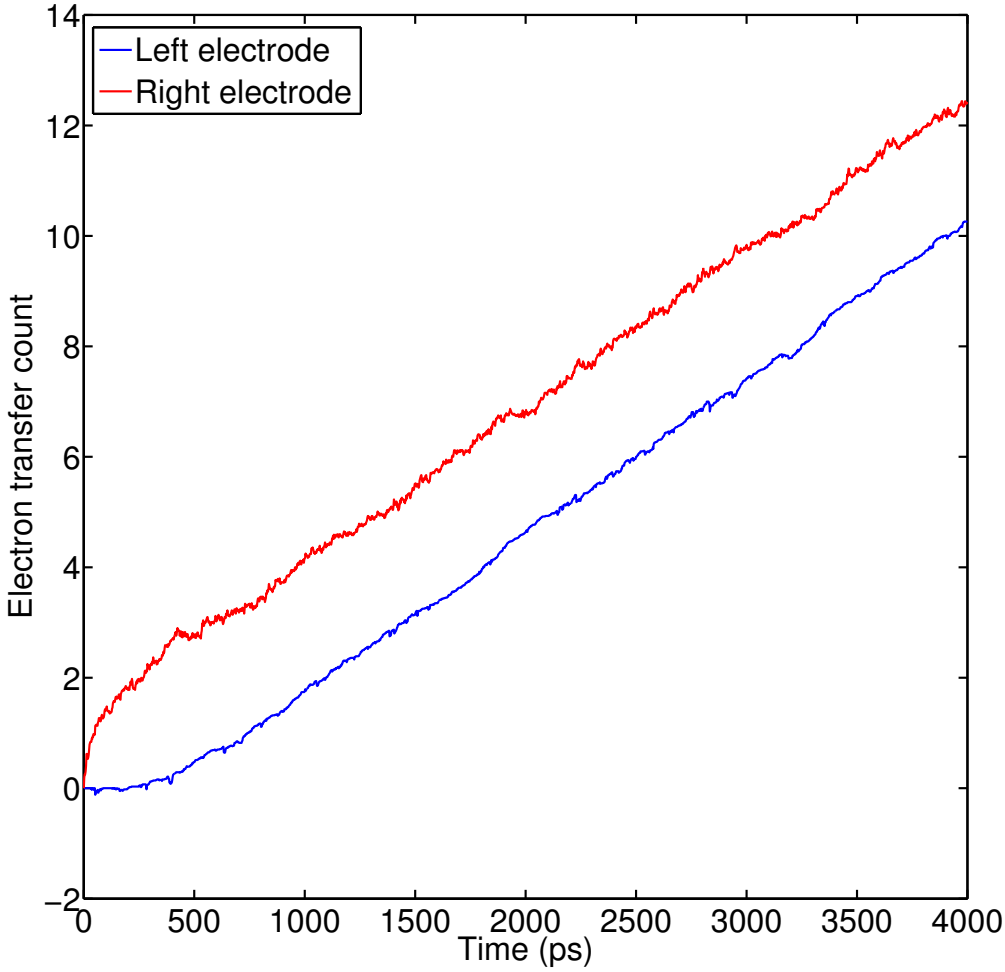

Figure 4.2: Cumulative net electron transfer count as a function of time at voltage 0.05V. $\Gamma_0/\hbar = 0.001/fs$. For the left electrode (blue), the net electron count is the total number of electrons that have been donated by the solute up through time t minus the total number of electrons that have been accepted by the solute up through time t. For the right electrode (red), the net electron count is the total number of electrons that have been accepted by the solute up through time t minus the total number of electrons that have been donated by the solute up through time t. The difference between the red and blue curves is the net charge of the system. At early times, the net electron transfer count does not grow linearly, but after some transient time, a steady state is reached whereby the net electron transfer count grow linearly; the current can be calculated from the slope.

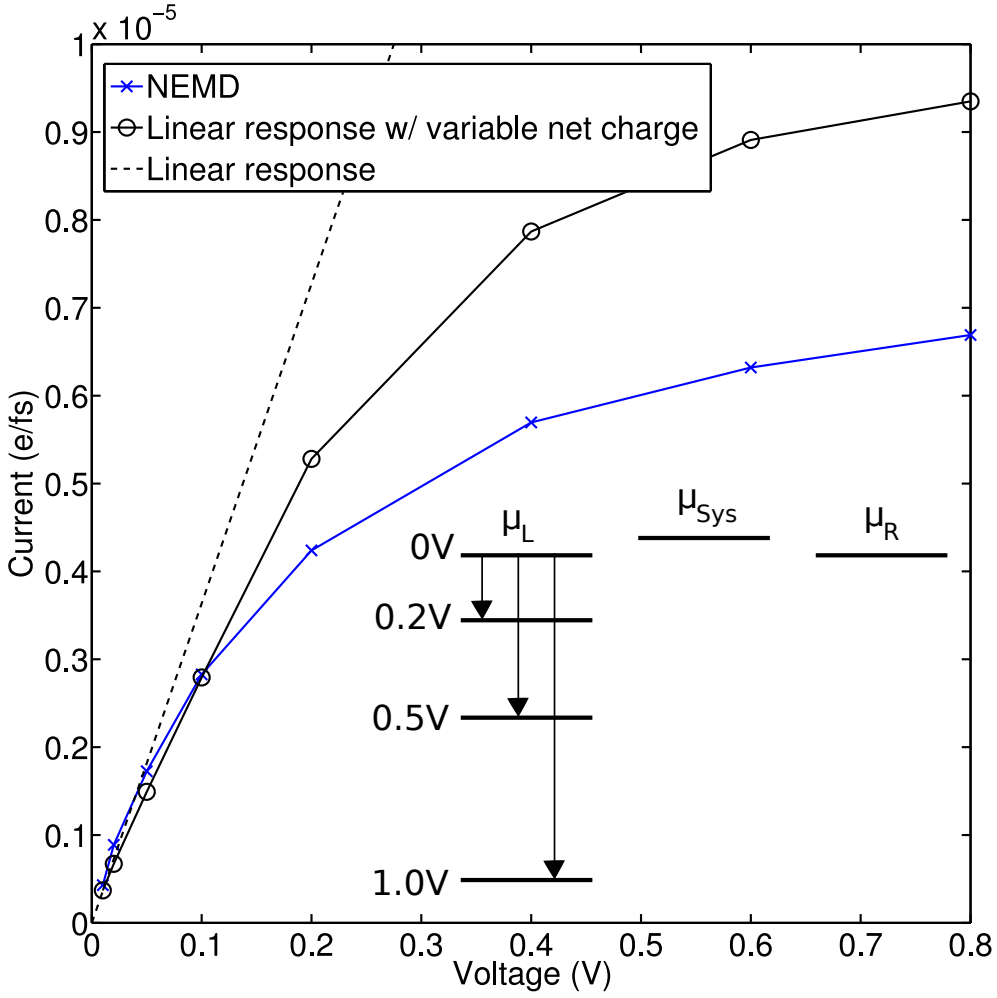

Figure 4.3: The current of the system as a function of the voltage applied. $\Gamma_0/\hbar = 0.001/fs$. The blue curve marked by crosses is the result from our non-equilibrium simulation (NEMD = Non-Equilibrium Molecular Dynamics). The black curves are estimates from linear response theory (Eq. (4.23)). The black curve with open circles calculates the current using a voltage-dependent number of B^- atoms (see Fig. 4.4); the dashed black line assumes that the number of charged solute atoms is fixed (at zero voltage). At low voltages, linear response theory agrees with our non-equilibrium results quite well, but linear response overestimates the current in the case of high voltage. The inset is a schematic figure illustrating how a change in voltage is applied to the system: we keep a fixed electrochemical potential μ_R for the right electrode and we decrease the electrochemical potential of the left electrode μ_L: $\mu_L \leq \mu_R$, resonant transport is not considered. μ_{Sys} denotes the electrochemical potential of the system (which is close to the electron affinity of the B atoms).

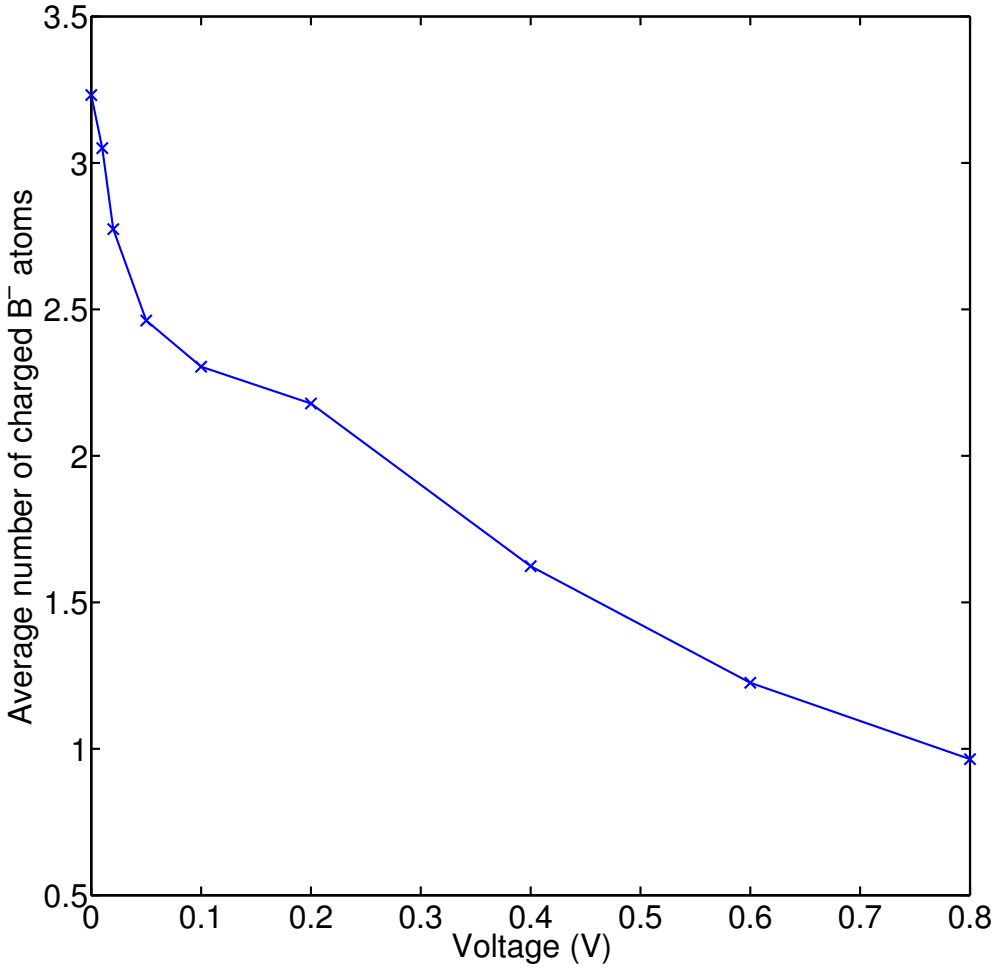

Figure 4.4: The average number of charged (B^-) atoms in the system as a function of voltage. $\Gamma_0/\hbar = 0.001/fs$. This number decreases as the voltage increases because our voltage window is applied only to the left electrode (see the inset of Fig. 4.3 for a schematic illustration).

the number of charged B^- atoms (N_q) is fixed and does not change with voltage (we choose the equilibrium (V = 0) density of B^- atoms in Fig. 4.4); naturally, this plot gives a completely linear I-V relationship. All three curves agree at small voltage but both linear response curves consistently overestimate the current at large voltages.

There are two possible explanations for the overestimation by linear response. First, at large voltages, the charge carriers need not respond linearly to the voltage so the charge carriers might move slower than suggested by a linear response estimate.[7] Second, as the voltage increases, the time scale for charge carrier drift decreases. Eventually, if the box is small enough, this time scale will become comparable to the time scale of electron transfer at the leads. At the same time, however, Eq. (4.23) takes into account only the migration of charge carriers (i.e. mass transport) to calculate current. Thus, if the waiting time experienced by charge carriers (before an electron transfer event) is not small compared to the mass transport time, linear response theory will obviously overestimate the current.

These two explanations are not mutually exclusive; both could be present in our simulation box. In fact, in Sec. 4.5.1, we will isolate how much each explanation contributes to the final current.

4.4.2 Position of Charged Solute (B^-) Atoms

Electrochemistry is the study of chemical reactions at metal surfaces. Our ultimate interest in these simulations are the dynamics of charge injection to or from the metal surface, and how those charge injection dynamics are influenced by the local environment at the surface of the metal (including the ambient electric field). For example, there is currently a great deal of interest in studying the double layer of

[7] After all, linear response theory works only when a perturbation is small compared to k_bT, which is approximately 0.026eV when $T = 300K$. Thus we can expect linear response theory to fail when the voltage is larger than 0.02V.

solvated ions near metallic surfaces[160–166]. To that end, a natural quantity for us to calculate is the distribution of charged ion position; this distribution is one measure of the solute's structure at the electrode interface and should be highly correlated with the dynamics of charge injection.

We have calculated this distribution in two different ways:

- We calculate a histogram while sampling ion positions from snapshots of non-equilibrium simulations.
- We fix a specific number of charged solute atoms for the system, and then construct a histogram while sampling ion positions from equilibrium simulations with a static electric field defined in Eq. (4.8).

These non-equilibrium and equilibrium distributions must be separately normalized for any comparison. *A priori*, we can expect two limiting cases. On the one hand, with weak enough coupling between the solution and the metal ($\Gamma_0 \to 0$), the equilibrium simulations must be equivalent to the non-equilibrium simulations if the charge is chosen correctly. On the other hand, if Γ_0 is large enough, we expect that ion density will be nearly uniform throughout the system, as current flows through the system.

Fig. 4.5(a) shows the normalized distribution (of z coordinates) corresponding to negative ion position both for non-equilibrium and equilibrium simulation at a low voltage (0.02V). For the equilibrium simulation, we inserted three B^- atoms into the simulation (which should be a good estimate; see Sec. 4.4.1 and Supporting Information). From Fig. 4.5(a), we find that, even with small voltage, the equilibrium distribution is nearly the mirror opposite of the non-equilibrium distribution. Whereas the equilibrium distribution (with a small electric field pointing to the right) slightly favors negative ions sitting on the left, the non-equilibrium distribution slightly favors negative ions on the right. This discrepancy is easy to rationalize: for the

non-equilibrium simulations alone, there is a small sink on the left which can accept electrons. (Note that the layer structure near both electrodes results simply from the Lennard-Jones interaction between the electrodes and the atoms; this layer structure is not terribly interesting.)

The differences between the equilibrium and non-equilibrium distributions in Fig. 4.5(a) are amplified dramatically in the case of higher voltage. Fig. 4.5(b) shows the normalized distributions at voltage 0.4V. For the equilibrium simulations, we consider either one or two B^- atoms. In this figure, the electric field drives all of the charged B^- ions far to the left according to the equilibrium simulations; however, according to the non-equilibrium simulations, there is nearly a uniform density of charged ions across the simulation box corresponding to a steady current through the liquid. Moreover, the density of anions decreases slowly as one approaches the sink on the left electrode. From this figure, one ascertains that there is far more screening of the external electric field in the equilibrium simulation as opposed to the non-equilibrium simulation. Whereas the B^- ions yield a strong electric field going from right to left in the equilibrium simulation (and against the external field), there is no such effect in the non-equilibrium simulations. In fact, in the non-equilibrium simulations, the B^- ions might even yield a small electric field going from left to right (in the same direction as the external field). In the future, it will be illuminating to insert bystander electrolytes into our simulation, as done by Voth *et al.* in Ref. 146, to model the screening effects of nonreactive ions.

In Fig. 4.5(c), we plot the non-equilibrium results from 0.02V and 0.4V on the same y-scale. Here, we see the density of B^- ions near the left electrode is indeed far lower in the case of high voltage as compared to the case of low voltage. To understand the difference, note that there are two opposing effects here. On the one hand, with higher voltage, the B^- ions feel an external field pushing them to the left.

On the other hand, however, with higher voltage, the electrons can also more easily escape into the left electrode once the B^- ion is close by. Apparently, in this regime, the second effect wins out. With a smaller Γ_0, however, the first effect does win out (as shown with the green cure in Fig. 4.5(c)).The relative sizes of these two effects will be crucial for understanding solvent structure at the interfaces of polarizable and non-polarizable electrodes.

4.4.3 Position of Electron Transfer

Lastly, we calculate the distribution of B or B^- ions at the time of electron transfer to help us to understand the I-V curve atomistically. We will calculate this distribution in two different ways:

- For the non-equilibrium simulations, we simply make a histogram of all B or B^- positions at the time of electron transfer.
- For the equilibrium simulations, we calculate the equilibrium distribution of B or B^- positions (assuming there is no electron transfer, $\Gamma_0 = 0$), and we multiply that equilibrium distribution by the position dependent hybridization function defined in Eq. (4.11).

Fig. 4.6 shows the normalized distribution of z coordinates for electron transfer events for both non-equilibrium and equilibrium simulations at low voltage (0.02V). The equilibrium simulation contains three B^- atoms. Note here that, in each subplot, the distributions are normalized across either the left side of the box $[-30, 0]$ or the right side of the box $[0, 30]$ (rather than across the whole region $[-30, 30]$ as in Sec. 4.4.2). As can be seen from the figure, the equilibrium and non-equilibrium results agree nearly exactly. This agreement can be understood by investigating Fig. 4.5 (a); even though the NEMD (blue) and equilibrium (red) curves are quantitatively

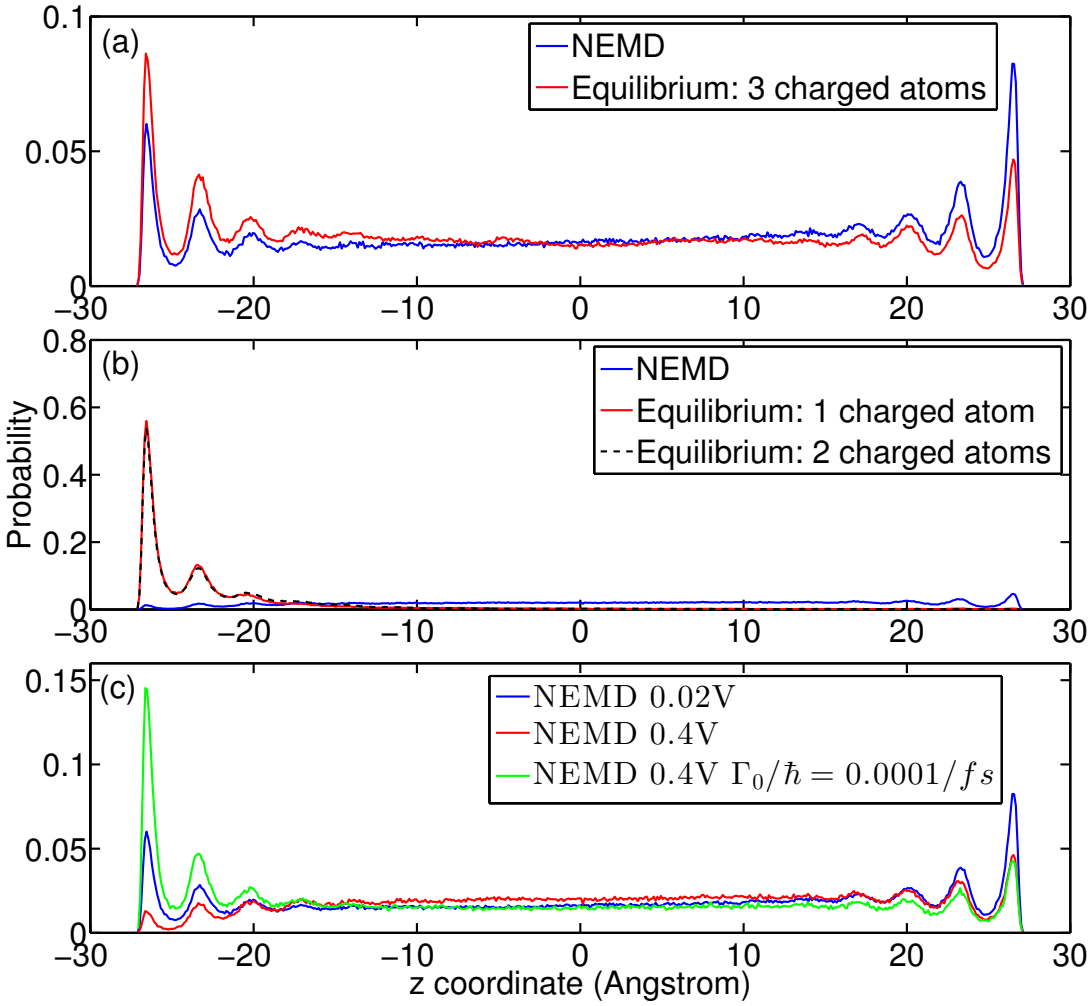

Figure 4.5: Normalized distribution of the z coordinates for the positions of the B^- ions using both non-equilibrium and equilibrium simulations. $\Gamma_0/\hbar = 0.001/fs$. (a) Low voltage 0.02V. (b) High voltage 0.4V. (c) Comparison of low and high voltage. For the green curve, we reduce the hybridization Γ_0 by a factor of 10, $\Gamma_0/\hbar = 0.0001/fs$. Equilibrium simulations with a number of B^- ions do not recover the non-equilibrium data at either low or high voltage, and the disagreement increases at higher voltage. Obviously, one cannot ignore the electron transfer rate at the electrodes for large enough Γ_0.

different from each other, the two curves are very similar if renormalized on the left and right hand sides respectively. For both curves in Fig. 4.5(a), the innermost layer nearest the electrode has a larger magnitude than the second layer. Thus, at low voltage, an equilibrium approach can correctly recover some features of non-equilibrium electron transfer–even with relatively large Γ_0.

Whereas Fig. 4.6 shows the equilibrium calculations can yield some useful information at low voltage, Fig. 4.7[8] shows that at high voltage (0.4V), the equilibrium simulations do not recover even the relative ratio of electron transfer events occurring in the different layers of the solution. This mismatch is perhaps not surprising given the different ion densities in Fig. 4.5(b) between the equilibrium and NEMD simulations. To confirm this interpretation, in Fig. 4.7(b) we plot a fourth curve, labeled "NEMD factorization", which is the NEMD ion distribution in Fig. 4.5(b) multiplied by $\Gamma(z)$ in Eq. (4.11). The agreement between this fourth curve and the histogram of non-equilibrium electron transfer positions suggests that, at steady state, the dynamics of charge transfer into the electrode can sometimes be characterized completely by the simple steady-state distribution of negative ions–but calculating such a distribution does require performing non-equilibrium molecular dynamics.[9]

[8]The keen observer will note that Fig. 4.7 holds only two subplots, as opposed to the four subplots in Fig. 4.6. This discrepancy exists because, in the case of high voltage, NEMD simulations do not allow for any electron transfer events from the left electrode to neutral solute atoms, while equilibrium simulation predict no B^- atom near the right electrode.

[9]And even then, this conclusion may not be general. Normally, one would at least need to consider the Fermi function in Eqs. (4.10) and (4.14) in order for the green curve to match the blue curve in Fig. 4.7(b). In the present case, however, the voltage is large enough such that, once a B^- ion reaches the vicinity of the left electrode where $\Gamma(z)$ is non-negligible, one can safely ignore the Fermi function.

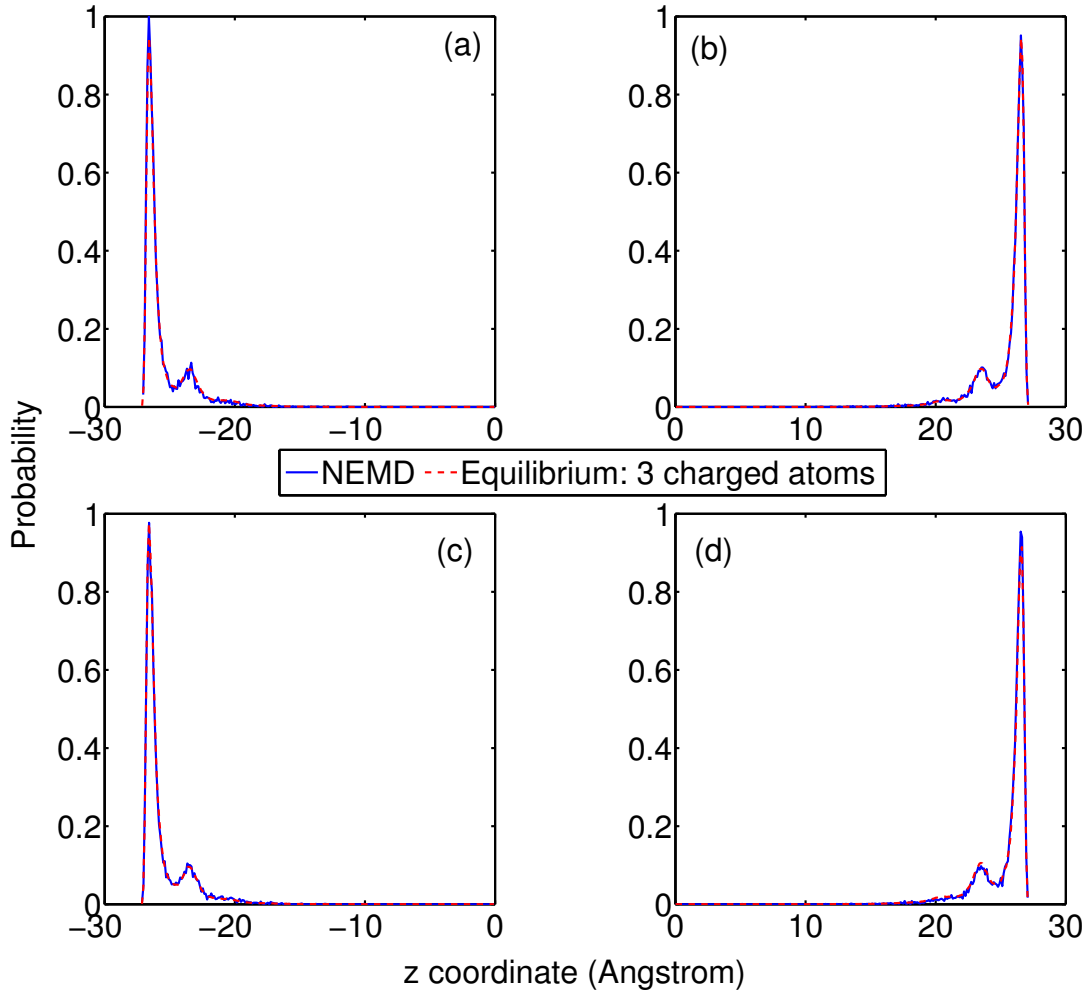

Figure 4.6: The normalized z-coordinate distribution of solute atoms during electron transfer events for both non-equilibrium and equilibrium simulations at voltage 0.02V. $\Gamma_0/\hbar = 0.001/fs$. Top: electron transfer from the electrodes to solute atoms. Bottom: electron transfer from solute atoms to the electrodes. (a) and (c) are normalized on the left hand side $[-30, 0]$; (b) and (d) are normalized on right hand side $[0, 30]$, The equilibrium simulation has three B^- atoms in the system. Clearly, an equilibrium simulation can recover the correct ratio of electron transfer events between different layers.

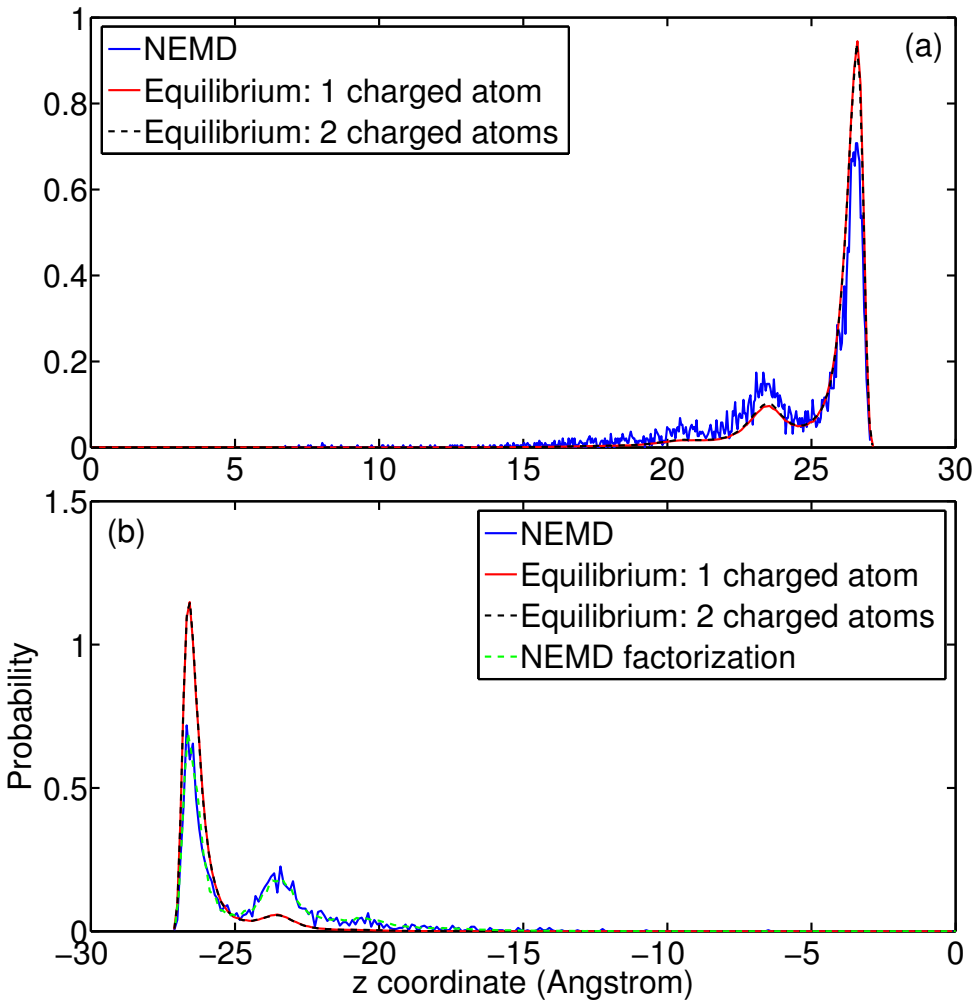

Figure 4.7: Voltage = 0.4V otherwise (a) Same as Fig. 4.6(b); (b) Same as Fig. 4.6(c). The equilibrium simulations have one and two B^- atoms in the system. Equilibrium simulations fail to recover the ratio of electron transfer events between different layers in such high voltage. However, as shown by the green dash curve labeled "NEMD factorization" in (b), the correct answer is recovered by multiplying the NEMD ion distribution in Fig. 4.5(b) by $\Gamma(z)$ in Eq. (4.11).

4.5 Discussion

4.5.1 Nonlinearity and Electron Transfer

In Sec. 4.4.1 (Fig. 4.3), we found that linear response consistently overestimates the true NEMD current. Given that the current in an electrochemical cell is limited by two major processes, (*i*) mass transport of charge carriers and (*ii*) electron transfer at the electrode interface, one would like to isolate the contribution of each process to the total current.

To disentangle these effects, we now use a very simple model to calculate the current in our solution. We divide the set of all negatively charge B^- anions into those near the left electrode and those near the right electrode, and imagine the mechanism:

$$B_r^- \xrightarrow{k_f} B_l^- \xrightarrow{\Gamma_{ET}/\hbar} B_l \tag{4.24}$$

Here, $B_{l/r}^-$ denotes the number (density) of B^- atoms near the left and right electrodes, respectively, k_f represents the drift rate of B^- atoms from right to left as caused by the ambient electric field, and $\Gamma_{ET}/\hbar$ is the electron transfer rate as the B^- atoms inject an electron into the left electrode. The kinetic equations for this model are:

$$\frac{dB_r^-}{dt} = -k_f B_r^- + S \tag{4.25a}$$

$$\frac{dB_l^-}{dt} = k_f B_r^- - \frac{\Gamma_{ET}}{\hbar} B_l^- \tag{4.25b}$$

$$\frac{dB_l}{dt} = \frac{\Gamma_{ET}}{\hbar} B_l^- \tag{4.25c}$$

where S represents a source current.

Now, the measurable current through the system is the electron transfer rate:

$$I = \frac{\Gamma_{ET}}{\hbar} B_l^- = \frac{\Gamma_{ET}}{\hbar} \frac{B_l^-}{B_r^- + B_l^-} \left(B_r^- + B_l^- \right) \tag{4.26}$$

At steady state (where $dB_l^-/dt = 0$ in Eq. (4.25b)), we find $B_l^- = \hbar k_f B_r^- / \Gamma_{ET}$, so Eq. (4.26) becomes:

$$I = \frac{\Gamma_{ET} k_f}{\Gamma_{ET} + \hbar k_f} \left(B_r^- + B_l^- \right) = \frac{\Gamma_{ET} k_f}{\Gamma_{ET} + \hbar k_f} N_q \tag{4.27}$$

Here N_q is the total number of B^- atoms in the system. Inverting Eq. (4.27), one finds a familiar equation[167]:

$$\frac{1}{I} = \frac{1}{k_f N_q} + \frac{\hbar}{\Gamma_{ET} N_q} = \frac{1}{I_{MT}} + \frac{\hbar}{\Gamma_{ET} N_q} \tag{4.28}$$

where I_{MT} is defined as the current of mass transport. Thus, within this model, we conclude that the total electron transfer time is the sum of the mass transport time plus the electron transfer time at the electrode. Note that Eqs. (4.25)-4.28 neglect the backward electron transfer from the left electrode to neutral B atoms. This unidirectional flow of electrons should be valid only at large voltages according to Eq. (4.10); as such, we expect Eq. (4.28) may deviate from reality when the voltage is low.

Eq. (4.28) can be used to roughly disentangle the effects of a slow charge injection time versus the effect of a breakdown of linear response at high voltage. To make such an argument, we must specify N_q, Γ_{ET}, and I_{MT} in Eq. (4.28).

- First, for N_q, the number of B^- atoms is taken from Fig. 4.4 (and the corresponding curve for smaller Γ_0).

- Second, for Γ_{ET}, one must use caution because the electron transfer rate in Eq. (4.11) is position dependent. Furthermore, from Fig. 4.6-4.7, we know that electron transfer events occur over a range of atomic positions. For the sake of simplicity (and also for consistency with the definition of I_{MT}), we will estimate Γ_{ET} by (i) calculating the average position of electron transfer from the atoms to the left electrode $\langle z_{ET} \rangle$ and (ii) replacing $z = L_z/2 - |\langle z_{ET} \rangle|$ in Eq. (4.11) to calculate a single rate $\Gamma_{ET}/\hbar$ for a specific voltage.

- Third and finally, to demonstrate the limitations of linear response theory, we will calculate the mass transport current I_{MT} in two different ways:

  1. We calculate the mass transport current according to linear response for ion flow, with Eq. (4.23).

  2. We analyze the non-equilibrium (NEMD) velocity profile of the B^- atoms (i.e. velocity distribution in space) and calculate the average velocity in the z direction $\langle v_z \rangle$. We then calculate I_{MT} as:

$$I_{MT} = \frac{N_q e \langle v_z \rangle}{L_z^{(eff)}}. \tag{4.29}$$

     A typical velocity profile is shown in Fig. 4.8, where one can differentiate the non-equilibrium velocity from the linear response velocity. The average non-equilibrium velocity $\langle v_z \rangle$ in the middle region of the system is approximately 31% smaller than the linear response velocity.

For consistency with Γ_{ET}, in Fig. 4.9 only, we redefine the effective length as $L_z^{(eff)} \equiv 2\,|\langle z_{ET} \rangle|$. Note that, with this definition, $L_z^{(eff)}$ will change a little bit depending on voltage.

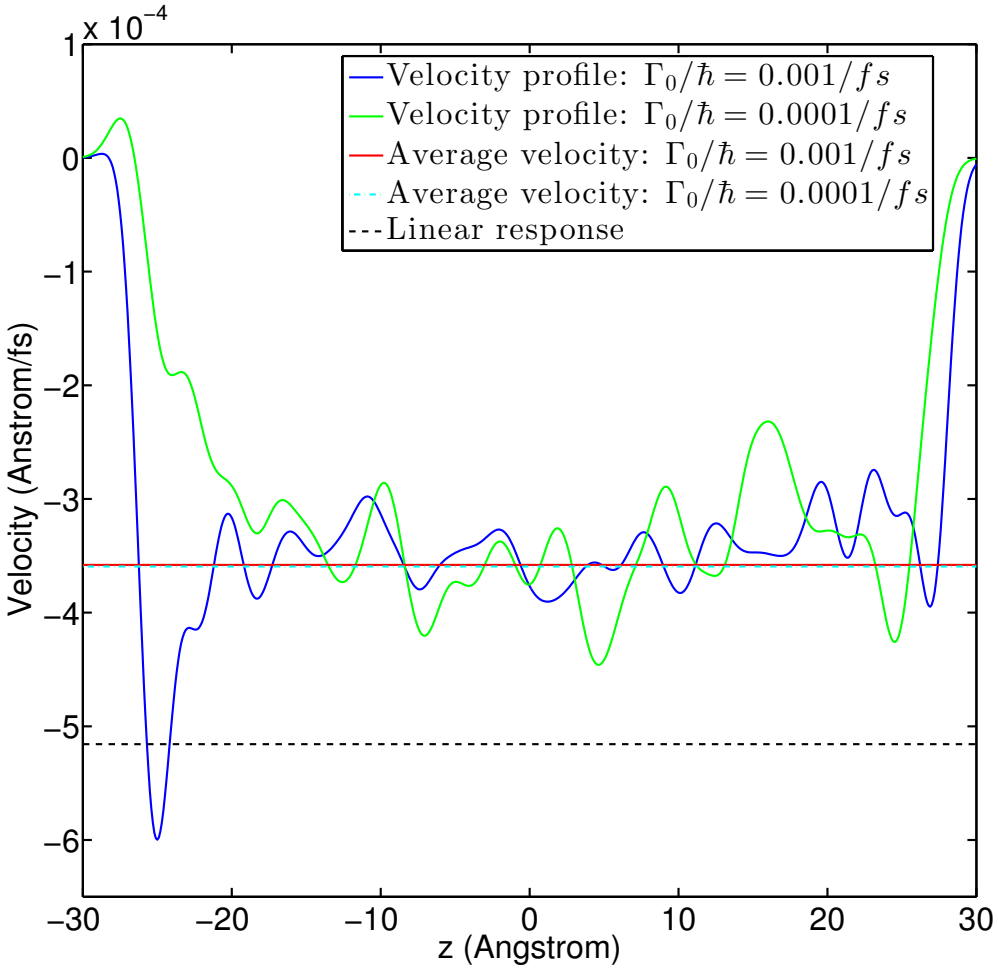

Figure 4.8: The NEMD velocity profiles for a voltage of 0.8V with $\Gamma_0/\hbar = 0.001$ (blue curve) and $\Gamma_0/\hbar = 0.0001$ (green curve). The velocity profiles have been smoothed by convolution with a Gaussian of width $\sigma = 1$Å. At the edges of the box, near the electrodes, the ions have net velocity zero (as they must). The red solid line and the cyan dashed-dot line are the average velocities in the range $[-10, 10]$Å for the two different Γ_0, respectively. Note that the average velocity in the middle of the system box is effectively independent of the value of Γ_0, and can be used to estimate the effective bulk drift velocity at high voltage. The black dashed line is the velocity calculated from linear response: $\langle v_z \rangle = u\mathcal{E}_z e$. The velocities are negative because the B^- atoms flow from right to left. The linear response result overestimates the velocity of the B^- atoms by approximately 31%.

In Fig. 4.9, we plot the NEMD I-V curves corresponding to two different hybridization functions (on the left $\Gamma_0/\hbar = 0.001$/fs, on the right $\Gamma_0/\hbar = 0.0001$/fs). We also plot Eq. (4.28): for I_{MT} we use either Eq. (4.23) or the non-equilibrium velocity profile in Fig. 4.8 with Eq. (4.29). For reference, we also include the raw linear response Green-Kubo estimates from Fig. 4.3. At high voltage, Fig. 4.9 isolates the corrections to the linear response current that arise from (*i*) calculating the velocity profile of a charge particle beyond linear response and (*ii*) including explicitly the waiting time for electron transfer.

This effectively completes our analysis of the I-V curves. The seasoned electrochemist might be surprised by the fact that, at high voltage, the current in our model is not limited by the diffusion of charge carriers as in a common electrochemical cell[167]. Instead, at large voltages, the current in Fig. 4.9 is limited largely by charge injection. The explanation for this discrepancy is that our simulations above do not include supporting electrolyte. If there are no supporting electrolytes to form a double layer near the electrode and screen almost all of the electric field, charged ions move by drift (i.e. they are pushed by the electric field) instead of by diffusion. And, in such a case, mass transport is not limiting at high voltage and small length scales.

4.5.2 Interfacial Reaction

Before concluding, we now want to say a few words about chemical reactions at electrode interfaces. Clearly, such chemical reactions (that create and break bonds) are missing in our treatment above. One simple means to incorporate such chemical reactions is to change the Lennard-Jones constants between charge carrying solute atoms and the electrodes, such that the charge carriers might be trapped on electrodes. The trapping of charge carriers at interfaces can be considered the simplest model of a chemical reaction whereby charge carriers become bonded to the electrode.

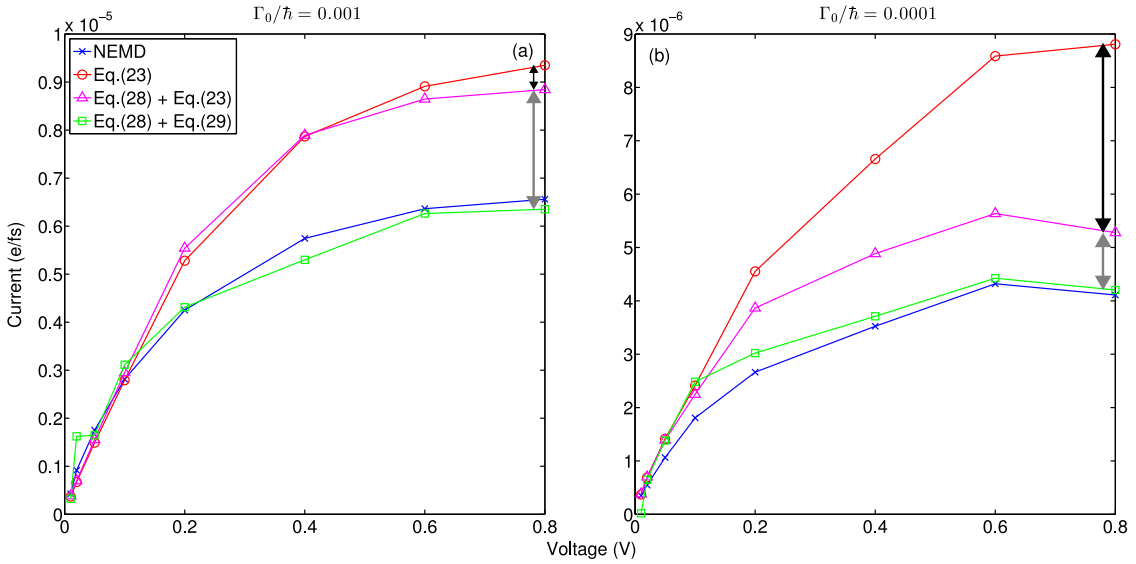

Figure 4.9: I-V curves calculated from NEMD simulations, linear response theory (Eq. (4.23), (same as in Fig. 4.3), and with a more sophisticated kinetic theory (Eq. (4.28)). Two different $\Gamma_0/\hbar$ are used in the simulations, (a) 0.001/fs and (b) 0.0001/fs. In Eq. (4.28), I_{MT} is calculated in two different ways : either with Eq. (4.23) or with Eq. (4.29). The black arrows represent the errors in current that arise from ignoring the waiting time for electron transfer, and the gray arrows represent the errors in current that arise from assuming that ionic velocity follows linear response theory.

With this in mind, we have studied different Lennard-Jones potentials as obtained by changing the constant ε and thereby adjusting the depth of the potential well. The base (1x) ε is set as 0.2379 (as used above in Sec. 4.3), and we consider Lennard-Jones constants ε of 2.379 (10x) and 11.895 (50x). In Fig. 4.10, we show the cumulative net electron transfer count as a function of time. We can see from the slope that, as ε increases, the current decreases. At 10x, we still measure a continuous current as the charge carriers are trapped only fleetingly; the B^- atoms manage to escape the attracted potential well of the electrode due to the collision with other atoms. However, when ε is very large (50x the base), the trapped charge carrier can no longer escape the trap of the electrode's potential and the electron transfer count becomes flat (i.e. there is no longer a current). One of the most exciting directions for future research will be modeling interfacial chemical reactions.

4.6 Conclusions and Future Directions

In this paper, we have employed a non-equilibrium simulation to investigate the transport of electrons as mediated through an ionic solution. Fig. 4.9 shows the key conclusions of this paper: in order to recover the results of a non-equilibrium simulation in the case of high applied voltage, we find it necessary to explicitly model both the nonequilibrium dynamics of the electron transfer processes and the nonlinear behavior of solute velocity.

Looking forward, we would next like to study larger simulations (e.g. those of Voth *et al.*[146,147]), including heterogeneous liquids made up of many polarizable solvent molecules and a host of electrolytes. While the model above was applied only for a collection of Lennard-Jones spheres, the approach should certainly be applicable to a variety of electrochemical systems, with arbitrarily complicated force fields. We would expect that, with polarizable waters as solvent, the electron-transfer dynamics

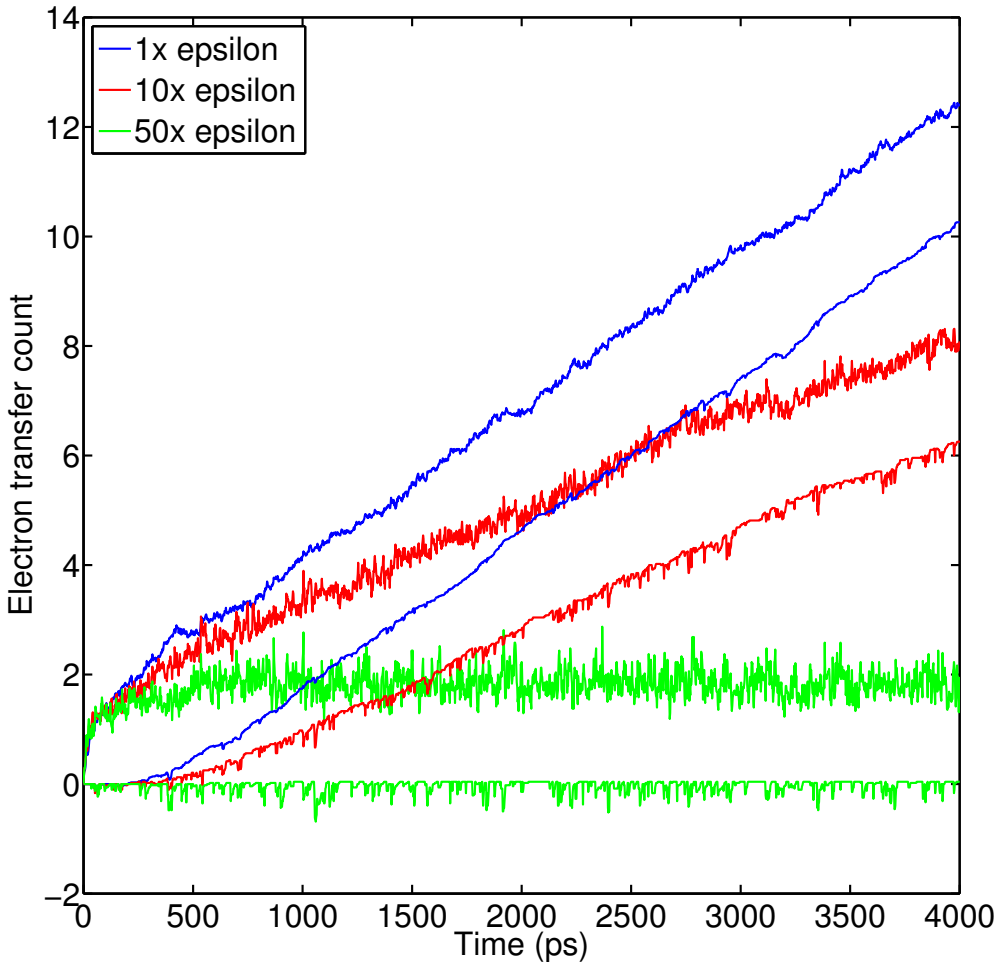

Figure 4.10: Cumulative net electron transfer count as a function of time at voltage 0.05V. Curves with different colors correspond to different Lennard-Jones constants (ε) that measure the strength of the attraction between charge carriers and electrodes. ε is set as 0.2379, 2.379 and 11.895 for the blue, red and green curves, respectively. The upper blue curve corresponds to the net number of electron transfer events from the right electrode to the solute atoms and the lower blue curve corresponds to the net number of electron transfer events from the solute atoms to left electrode, etc. The slope of the curves is the current. As ε increases, charge carriers become trapped near the electrode and the current through the system decreases. When ε is large enough, the trapped charge carriers can no longer escape the potential well and the steady state current is effectively zero as indicated by the flat green curves.

will be sensitive to the time scale for water reorientation ($\sim$ 1 ps) and that solvent structure and electrostatic shielding may greatly affect the probability for an electron hop. Furthermore, as is well known, with electrolytes, a double layer will appear that will further shield the external electric field so that, even at reasonably high voltages, mass transfer is by diffusion rather than by drift. We are now beginning to run such calculations.

For very large systems, a direct study of charge transport may be difficult with the direct approach detailed in Sec. 4.2. The reasons are threefold: First, because the electronic coupling is position dependent and the electron transfer event is probabilistic, our simulation time step (dt) is severely limited by the time scale for electron transfer and dt cannot be too large. Second, we waste a great deal of time calculating solvent reconfiguration and diffusion, especially since there are potentially more computationally efficient means to addresses such processes. If we want to handle large electrochemical cells, we expect methodological advances will be necessary to enhance the sampling of the electron transfer processes. Third and finally, one difficult question that will need to be addressed is how does the presence of polarizable solvent molecules affect the quantum mechanical lifetime (or broadening) of a charged ion (Eq. (4.11)). This work is ongoing.

4.7 Acknowledgments

This material is based upon work supported by the (U.S.) Air Force Office of Scientific Research (USAFOSR) PECASE award under AFOSR Grant No. FA9950-13-1-0157. J.E.S. acknowledges a Cottrell Research Scholar Fellowship and a David and Lucille Packard Fellowship. J.G.S. acknowledges support from NSF: MRSEC DMR-1120901 and CHE-1412496.

CHAPTER 5

The Dynamics of Barrier Crossings for the Generalized Anderson-Holstein Model: Beyond Electronic Friction and Conventional Surface Hopping

This chapter is adapted from Journal of Chemical Theory and Computation, Volume 12, Issue 9, Page 4178-4183, 2016.

5.1 Introduction

The Anderson-Holstein (AH) model is the most basic model describing electron transfer (ET) at a metal surface: it captures the necessary electronic coupling (i.e. electronic tunneling), nuclear-electronic coupling (which leads to nuclear motion), and electronic relaxation (which leads to broadening). In short, the model can be considered the generalization of the simple spin-boson model[168], but now with a manifold of donor and acceptor states[169].

While the usual AH model requires diabatic potential energy surfaces (PESs), a generalized AH model can be written as follows[60]:

$$H = H_s + H_b + H_c, \tag{5.1a}$$

$$H_s = E(x)d^\dagger d + V_0(x) + \frac{p^2}{2m}, \tag{5.1b}$$

$$H_b = \sum_k \left(\epsilon_k - \mu\right) c_k^\dagger c_k, \tag{5.1c}$$

$$H_c = \sum_k W_k \left(c_k^\dagger d + d^\dagger c_k\right), \tag{5.1d}$$

$E(x)$ represents the change in the nuclear PES that occurs when the electronic im-

purity level ($d^\dagger, d$) becomes occupied, and μ is the Fermi level of bath. If $V_0(x)$ is the diabatic PES for the unoccupied state, we define the diabatic PES for the occupied state to be:

$$V_1(x) \equiv V_0(x) + E(x). \tag{5.2}$$

The key parameters for the AH model are: the molecule-metal coupling ($\Gamma(\epsilon) \equiv 2\pi \sum_k |W_k|^2 \delta(\epsilon_k - \epsilon)$), the nuclear motion ($\omega \equiv \sqrt{V_0''(x_{eq})/m}$), the temperature of the metal (T) and the nuclear-electronic coupling ($E(x)$). Note that, in the wide band approximation, $\Gamma(\epsilon)$ is independent of energy, $\Gamma(\epsilon) = \Gamma$.

In this paper, we will work exclusively in the high temperature limit ($\omega \ll k_b T$) whereby the nuclear degree of freedom can be calculated classically. Whereas there are many literature regarding the activated nonadiabatic ET rate between two level systems in solution[142,170–173], there is a far smaller literature studying barrier crossings in the presence of a manifold of electronic states at high temperatures (without tunneling) using mixed quantum-classical dynamics. A few research groups have investigated this problem in the electrochemistry community. Mohr and Schmickler *et al*[174,175] have investigated short time dynamics (ignoring some feedback of the solvent) to estimate rates. Mishra and Waldeck[176,177] have hypothesized two different approaches for treating the continuum of states: one (a "density of states" model) averages Fermi Golden Rule rates over a degree of freedom that implicitly represents a solvent parameter; the other (a "potential energy curve" model) treats the nuclei explicitly and uses a variation of Landau-Zener transition state theory. These authors have not directly investigated the nonadiabatic dynamic trajectories.

Now, in the molecular conduction community, there is an enormous literature on the study of the AH model with a focus on electron-phonon effects at low temperatures, for which vibrational degrees of freedom are kept quantum mechanical (without

passing to the classical limit). For instance, a great deal of work with nonequilibrium Green's functions has been published by Nitzan and Galperin and others predicting inelastic electron tunneling spectra (IETS) as occurs when vibrations scatter with tunneling electrons[48–51]. In the context of heterogeneous electron transfer, Wang, Thoss and Kondov partially diagonalized the AH model Hamiltonian to study an ultrafast electron transfer reaction at a dye-semiconductor interface[52–55]. Very recently, Wang, Thoss, Rabani and co-workers have investigated the dynamics of barrier crossings through reduced density matrices[178,179] in order to examine hysteresis at very low temperatures and quantify the effects of tunneling.[56–59]. We also note that Refs 49,169 have connected the rates of electronic transport for the AH model to semiclassical Marcus rates of ET in solution.

In the present article, our focus is not low temperature physics (which is difficult because of vibrational quanta) but rather high temperature physics (which is more tractable). Our goal is to implement a host of relatively new, semiclassical techniques to directly calculate the rate of activated barrier crossings for the AH model at classical temperatures. We will explore barrier crossings over a range of parameter regimes, all the way from the nonadiabatic (small Γ) to the adiabatic (large Γ). We will focus on two dynamical approaches: surface hopping (SH)[47] and electronic friction (EF)[46,180,181]. (*i*) On the one hand, SH captures the correct physics when Γ is small and is consistent with Marcus's theory of outer sphere ET[47]. (*ii*) On the other hand, EF dynamics are appropriate when nuclear velocities are small, such that dynamics can be approximated along a single adiabatic PES – almost in a Born-Oppenheimer picture (with large Γ) – but with a new source of electronic friction[46,180–187]. (*iii*) Beyond SH and EF dynamics, we will also benchmark a third approach, namely a broadened classical master equation (BCME) approach, that we recently proposed

as an extrapolation between the two limits[60,61][10] Below, we will show that BCME dynamics do in fact recover the correct rates of barrier crossings in the presence of a manifold of electronic states for all values of Γ; thus, we will conclude that BCME trajectories can be used to guide our intuition for the appropriate dynamics.

5.2 Theory

5.2.1 Dynamics

To begin our discussion, let us review how to propagate the dynamics for the Hamiltonian in Eq. (5.1) using SH and EF dynamics.

Surface Hopping (SH)/Classical Master Equation (CME)

For SH dynamics, we assume we are in the limit of small Γ ($\Gamma \ll k_b T$) and, as always, classical nuclear motion ($\omega \ll k_b T$) so that electronic transitions between diabats are rare and there is a valid separation of vibrational and electronic timescales. SH dictates (as derived by Redfield's perturbation theory[143,188]) that one propagate dynamics on the diabatic surfaces with hops between them. Let $P_0(x,p,t)$ ($P_1(x,p,t)$) be the probability density for the electronic impurity level to be unoccupied (occupied) at time t with the nucleus at position (x,p) in phase space. Mathematically, one must

[10]Note that the BCME using the potential in Eq. (5.10) describes only a single orbital coupled to a continuum of states. Extending the BCME to multiple orbitals coupled to a continuum of states is nontrivial. Such an extension will be studied in the future.

solve the following classical master equation (CME)[47]:

$$\begin{aligned}\frac{\partial P_0(x,p,t)}{\partial t} =& \frac{\partial V_0(x,p)}{\partial x}\frac{\partial P_0(x,p,t)}{\partial p} - \frac{p}{m}\frac{\partial P_0(x,p,t)}{\partial x} \\ &- \frac{\Gamma}{\hbar} f\left(E(x)\right) P_0(x,p,t) \\ &+ \frac{\Gamma}{\hbar}\left(1 - f\left(E(x)\right)\right) P_1(x,p,t), \qquad (5.3a)\\ \frac{\partial P_1(x,p,t)}{\partial t} =& \frac{\partial V_1(x,p)}{\partial x}\frac{\partial P_1(x,p,t)}{\partial p} - \frac{p}{m}\frac{\partial P_1(x,p,t)}{\partial x} \\ &+ \frac{\Gamma}{\hbar} f\left(E(x)\right) P_0(x,p,t) \\ &- \frac{\Gamma}{\hbar}\left(1 - f\left(E(x)\right)\right) P_1(x,p,t). \qquad (5.3b)\end{aligned}$$

Here $f(\epsilon) \equiv 1/(1+e^{\beta(\epsilon-\mu)})$ is the Fermi function with $\beta \equiv 1/(k_b T)$. Note that the SH dynamics in Eq. (5.3) are appropriate for open electronic systems (where energy can flow to or from the bath when the system hops between states). These dynamics are distinct from the more conventional, energy-conserving dynamics proposed by Tully[13] that are appropriate in a closed system.

Electronic Friction (EF)

As an alternative to SH dynamics, EF dynamics are relevant for "slow" nuclear velocities (where the meaning of slow will be discussed below). For EF, one propagates nuclei along an "adiabatic" potential of mean force (PMF) subject to Langevin dynamics. One can define two different PMFs, one PMF with the correct broadening (BPMF) prescribed by nonequilibrium Green's functions[46,60,181]

$$U^{(b)}(x) = V_0(x) + \int_{x_0}^{x} dx' n(E(x')) \frac{\partial E(x')}{\partial x'}, \qquad (5.4)$$

$$n(E) \equiv \int_{-\infty}^{\infty} \frac{d\epsilon}{2\pi} \frac{\Gamma}{(\epsilon - E)^2 + \Gamma^2/4} f(E) \qquad (5.5)$$

and one approximate PMF without broadening

$$U(x) = V_0(x) - \frac{1}{\beta}\log\left(1 + e^{-\beta E(x)}\right). \tag{5.6}$$

Here, x_0 is an arbitrary constant. See Fig. 5.1(a) for a plot of these potentials. At high temperature, broadening is not important and $U(x) = U^{(b)}(x)$.

For the Langevin dynamics, the correct form of electronic friction (with broadening) is[46,60,181,185–187]:

$$\gamma_e^{(b)} = \frac{\hbar\beta}{\Gamma} D(E(x)) \left(\frac{dE(x)}{dx}\right)^2, \tag{5.7}$$

$$D(E) \equiv \Gamma \int_{-\infty}^{\infty} \frac{d\epsilon}{\pi} \left(\frac{\Gamma/2}{(\epsilon - E)^2 + \Gamma^2/4}\right)^2 f(E)\left(1 - f(E)\right) \tag{5.8}$$

and an approximate form (without broadening) is

$$\gamma_e = \frac{\hbar\beta}{\Gamma} f(E(x))(1 - f(E(x))) \left(\frac{dE(x)}{dx}\right)^2. \tag{5.9}$$

Henceforward, we will refer to Langevin dynamics with Eqs. (5.4) and (5.7) as broadened Fokker-Planck (BFP) dynamics and Langevin dynamics with Eqs. (5.6) and (5.9) as (unbroadened) Fokker-Planck dynamics (FP) dynamics. We emphasize that, in order to derive the notion of electronic friction, one must necessarily throw out several terms in any derivation and take the limit of "slow"-moving nuclei[189]. Previously, we have argued that, in the context of parabolic diabatic surfaces (with frequency ω), electronic friction should be relevant only when $\Gamma > \omega$[46]; as shown below, this condition should be sufficient for the validity of electronic friction, but not always necessary if there is a source of external, non-electronic nuclear friction ($\gamma_n \neq 0$).

Broadened Classical Master Equation (BCME)

Lastly, we have recently proposed a third option for running dynamics for the Hamiltonian in Eq. (5.1). For these dynamics, denoted broadened classical master equation (BCME), we run SH along broadened diabatic PESs, defined as ($i = 0, 1$)[61]:

$$V_i^{(b)}(x) \equiv V_i(x) + \int_{x_0}^{x} dx' \left(n(E(x')) - f(E(x'))\right) \frac{dE(x')}{dx'}. \tag{5.10}$$

See Fig. 5.1(a) for a plot of these potentials.

As shown in Ref. 60, these BCME (diabatic) dynamics are equivalent to EF (adiabatic) dynamics along the BPMF (Eq. (5.4)) but with unbroadened friction (Eq. (5.9)). Empirically, to date, we have found that BCME dynamics successfully interpolate between SH (in the limit of small Γ) and BFP dynamics (in the limit of large Γ)[60,61].

One historical note is perhaps appropriate. In 2002, Mohr and Schmickler conjectured a different surface-hopping scheme[190] to extrapolate between the adiabatic and nonadiabatic limits. According to their scheme, one runs nuclear dynamics on a mean-field potential followed by collapsing events to a diabatic potential energy surface. Thus, the Mohr-Schmickler proposed dynamics were in the spirit of what Prezhdo-Rossky[191] and Hack-Truhlar[192] conjectured for Tully's normal fewest-switches surface-hopping algorithm[13] in solution. Although we do not believe these approaches can be justified rigorously, the methods clearly have a physical motivation and the similarity between these approaches is itself noteworthy.

5.2.2 Rate Constant

We will now investigate the rate of escape for a particle which is subject to Langevin dynamics with an external non-electronic source of nuclear friction ($\gamma_n \neq 0$); the

particle must emerge from one diabatic PES (V_0 in Eq. (5.1)) into another diabatic PES (V_1). We start with parabolic PESs:

$$V_0(x) = \frac{1}{2} m\omega^2 x^2, \tag{5.11a}$$

$$V_1(x) = \frac{1}{2} m\omega^2 (x-g)^2 + \Delta G^0. \tag{5.11b}$$

The reorganization energy E_r is defined to be $E_r \equiv 1/2 m\omega^2 g^2$. For comparison, there are three relevant analytical rate theories.

First, in the limit of small Γ, the Marcus rate of electron transfer is[188]:

$$k_{1\to 0} = \int_{-\infty}^{\infty} d\epsilon \frac{\Gamma(\epsilon)}{\hbar} (1 - f(\epsilon)) \frac{e^{-(E_r - \Delta G^0 + \epsilon)^2 / 4E_r k_b T}}{\sqrt{4\pi E_r k_b T}}, \tag{5.12a}$$

$$k_{0\to 1} = \int_{-\infty}^{\infty} d\epsilon \frac{\Gamma(\epsilon)}{\hbar} f(\epsilon) \frac{e^{-(E_r + \Delta G^0 - \epsilon)^2 / 4E_r k_b T}}{\sqrt{4\pi E_r k_b T}}. \tag{5.12b}$$

Here, ΔG^0 is the free energy difference between the occupied impurity state (denoted as "1") and the unoccupied impurity state (denoted as "0"). Eq. (5.12) can be derived through many different pathways, either starting with Fermi's Golden Rule or using Redfield theory.[142]

Second, in the limit of large Γ, all dynamics are adiabatic along a BPMF (Eq. (5.4)). Provided that electronic friction is small (see Eq. (5.7)), one can use straightforward adiabatic transition state theory (TST) for the rate:

$$k_{TST} = \kappa \frac{\omega}{2\pi} e^{-\beta U^{(b)\ddagger}}. \tag{5.13}$$

Here, $U^{(b)\ddagger}$ is the barrier height in Eq. (5.4) and κ is a transmission function that must be calculated ($\kappa \leqslant 1$).

Third, for an analytic rate expression that interpolates between the Marcus nona-

diabatic rate (at small Γ) and the adiabatic rate (at large Γ), one option is to invoke Landau-Zener theory (which can be applied in the nonadiabatic and adiabatic limits). However, because the system is coupled to a continuum of electron bath states, Landau-Zener theory must necessarily require a sum-over-states approach (which must be done carefully; see Ref. 177 for a good discussion). This will be the subject of another paper. Another interpolation scheme is the Zusman approach[171,172,193,194], which is roughly:

$$k_{Zusman}^{-1} = k_{Marcus}^{-1} + k_{TST}^{-1}. \tag{5.14}$$

5.3 Results and Discussion

5.3.1 Parabolic Diabats

Results for the parabolic PESs defined in Eq. (5.11) are plotted in Fig. 5.1. Rates were obtained by fitting diabatic population to an exponential as a function of time. We observe that, as Γ increases from small to large, the rate changes from: (*i*) linear in Γ (which agrees with Marcus theory, Eq. (5.12)), (*ii*) followed but a slight-leveling off, and then (*iii*) eventually followed by another nearly exponential rise (which agrees with transition state theory, Eq. (5.13)). These features have been predicted earlier by Schmickler[190]: as we increase Γ, the escape rate increases for small Γ because one increases the probability for an electron to hop; while, for large Γ, the rate increases because the adiabatic barrier decreases. See Refs. 177 for a nice discussion of this physics. A similar phenomenon is also seen for the ET rate of a standard two level system in solution.[195,19611] Note that our prescribed BCME (Eq. (5.10)) agrees with this interpretation and interpolates correctly from the CME to BFP, giving us a very

[11]The physics of the AH model and the spin-boson model Hamiltonian can be very different however. For instance, note that there is no analogue of electronic friction for spin-boson Hamiltonians; for a meaningful notion of electronic friction, one requires a manifold of electronic states.

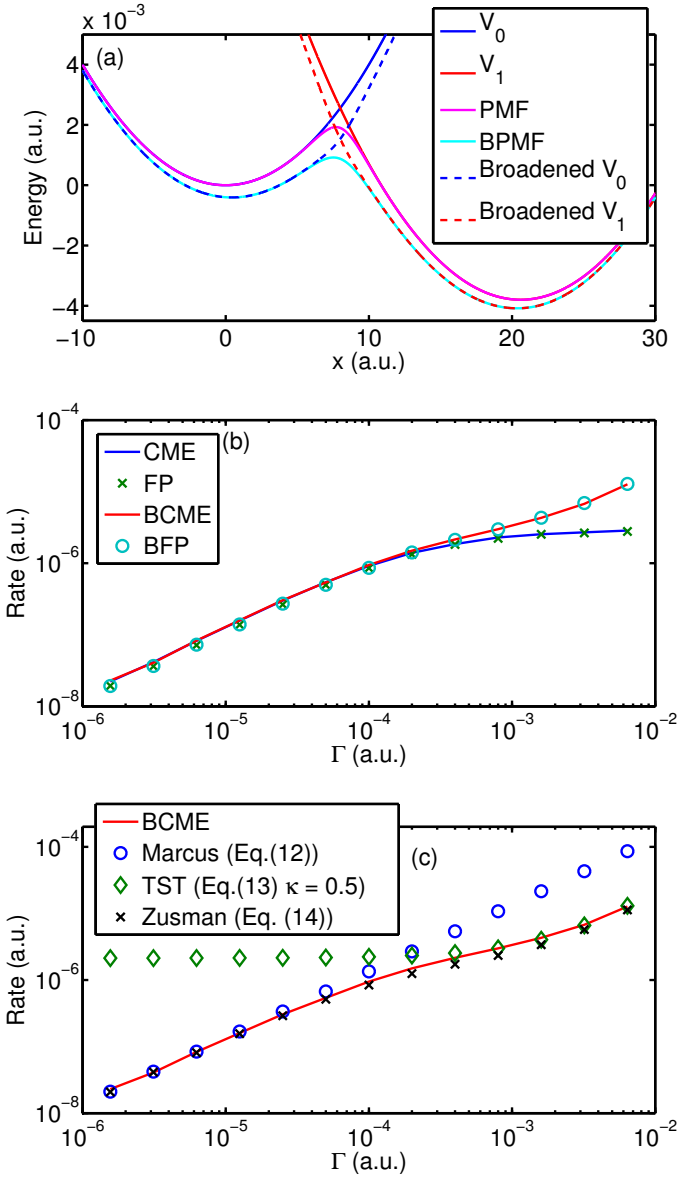

Figure 5.1: (a) Shifted, diabatic harmonic PESs defined in Eq. (5.11). The potential of mean force (PMF, Eq. (5.6)), broadened PMF (BPMF, Eq. (5.4)) and broadened diabatic PESs (Eq. (5.10)) for $\Gamma = 0.0016$ $a.u.$ are also shown. (b) The rates of reaction as a function of Γ for the four dynamics algorithms. The parameters are (all in atomic units): mass $m = 2000$, $\omega = 0.0002$, $g = 20.6097$, $\Delta G^0 = -0.0038$ and nuclear friction $\gamma_n = 2m\omega = 0.8$. The temperature is $300K$ (so $k_bT = 9.5 \times 10^{-4} a.u.$). The barrier height for the unbroadened surfaces is 0.00256 $a.u.$. The CME must be valid for small Γ and BFP must be valid for large Γ. Note that BCME and BFP work across the full range of Γ. (c) The rate as a function of Γ according to standard rate theories. The transmission coefficient κ in Eq. (5.13) is fit to be $\kappa = 0.5$.

simple picture of the correct semiclassical trajectories.

The Zusman rates are shown in Fig. 5.1(c) and agree fairly well with our BCME results. This near agreement is perhaps surprising because Zusman theory can be derived[171,172,193,194] for a two-state spin-boson model, whereas the physics here involve a continuum of electronic states (rather than two). For instance, note that electronic transitions can be delocalized according to the surface hopping protocol (Eq. (5.3)), whereas ET is assumed to happen only at the diabatic crossing point according to Zusman theory. From the agreement in Fig. 5.1(c), we hypothesize that, even for the AH model, ET between diabats must occur mostly at the crossing point (where the Fermi function switches quickly from 0 to 1).

5.3.2 Electronic Friction for Small Γ

The most surprising feature of Fig. 5.1 is the behavior of FP/BFP at small Γ. As stated above, we do not expect FP dynamics to be correct for $\Gamma \ll \omega$ (at least in vacuum)[46]. That being said, note that FP dynamics agree with CME and Marcus theory. In fact, let us now prove a near equivalence (which will be valid for escape rates over large barriers).

First, let us rewrite Marcus's nonadiabatic theory of ET (Eq. (5.12)) as an integral over the real space of the oscillator[188]:

$$k_{0\to 1} = \int_{-\infty}^{\infty} dx \frac{\Gamma}{\hbar} f\left(E(x)\right) \frac{e^{-\beta V_0(x)}}{Z_0}. \tag{5.15}$$

Here, Z_0 is the partition function for $V_0(x)$; for the harmonic case in Fig. 5.1, $Z_0 =$

$\sqrt{2\pi/(\beta m\omega^2)}$. According Eq. (5.6), Eq. (5.15) can be written as:

$$\begin{aligned} k_{0\to 1} &= \int_{-\infty}^{\infty} dx \frac{\Gamma}{\hbar} f\left(E(x)\right)\left(1-f\left(E(x)\right)\right)\frac{e^{-\beta U(x)}}{Z_0} \\ &= \int_{-\infty}^{\infty} dx \frac{\Gamma}{\hbar}\left(\frac{-df\left(E(x)\right)}{dx}\right)\left(\beta\frac{dE(x)}{dx}\right)^{-1}\frac{e^{-\beta U(x)}}{Z_0} \\ &\approx \int_{-\infty}^{\infty} dx \frac{\Gamma}{\hbar}\delta\left(x-x_B\right)\left(\beta\left|\frac{dE(x)}{dx}\right|\right)^{-1}\frac{e^{-\beta U(x)}}{Z_0} \\ &= \frac{\Gamma}{\beta\hbar}\left|\frac{dE(x)}{dx}\right|_{x=x_B}\Bigg|^{-1}\frac{e^{-\beta U(x_B)}}{Z_0}. \end{aligned} \tag{5.16}$$

Here, we have used the large barrier approximation so the derivative of Fermi function is approximated as a Dirac delta function. x_B is the coordinate of the diabatic crossing point. Eq. (5.16) was obtained long ago by Wolynes[197], Ulstrup[198] and Levich[199].

Second, let us treat FP dynamics with electronic friction. Note that, as $\Gamma \to 0$, the electronic friction (Eqs. (5.9)-(5.7)) becomes infinite. According to Kramer's theory[142] of the adiabatic rate constant in the overdamped limit, the rate can be written as:

$$\begin{aligned} k &= \left[\int_{-\infty}^{x_B} dx e^{-\beta U(x)}\int_{x}^{\infty} dx'\beta\gamma_e e^{\beta U(x')}\right]^{-1} \\ &= \left[\int_{-\infty}^{x_B} dx e^{-\beta U(x)}\int_{x}^{\infty} dx'\frac{\beta^2\hbar}{\Gamma} f\left(E(x')\right)\left(1-f\left(E(x')\right)\right)\left(\frac{dE(x')}{dx'}\right)^2 e^{\beta U(x')}\right]^{-1} \\ &= \left[\int_{-\infty}^{x_B} dx e^{-\beta U(x)}\int_{x}^{\infty} dx'\frac{\beta\hbar}{\Gamma}\left(\frac{-df(E(x'))}{dx'}\right)\frac{dE(x')}{dx'}e^{\beta U(x')}\right]^{-1}. \end{aligned} \tag{5.17}$$

Converting df/dx to a delta function again,[12]

$$\begin{aligned} k &\approx \left[\int_{-\infty}^{x_B} dx e^{-\beta U(x)} \int_{x}^{\infty} dx' \frac{\beta\hbar}{\Gamma} \delta\left(x' - x_B\right) \left|\frac{dE(x')}{dx'}\right| e^{\beta U(x')}\right]^{-1} \\ &= \left[\int_{-\infty}^{x_B} dx e^{-\beta U(x)} \frac{\beta\hbar}{\Gamma} \left|\frac{dE(x)}{dx}\right|_{x=x_B} \right| e^{\beta U(x_B)}\Bigg]^{-1} \\ &\approx \frac{1}{Z_0}\frac{\Gamma}{\hbar\beta} \left|\frac{dE(x)}{dx}\right|_{x=x_B}\Bigg|^{-1} e^{-\beta U(x_B)}. \end{aligned} \tag{5.18}$$

In the last line, we have approximated $\int_{-\infty}^{x_B} \exp\left(-\beta U(x)\right)$ as Z_0, again based on the large barrier approximation.

From the manipulations above, it is clear that Eq. (5.16) and Eq. (5.18) are identical, so that FP and Marcus theory should be roughly equivalent for small Γ when there is a large barrier preventing any escape from one diabatic well and an external source of nuclear friction ($\gamma_n \neq 0$). Thus, adiabatic dynamics can seemingly recover nonadiabatic features.

5.3.3 Quartic versus Quadratic Diabatic Potentials

Before concluding, we must emphasize that, for small Γ, even though FP and Marcus theory may agree for the case of large barriers, neither of these models needs to be correct and neither one will necessary agree with the correct CME dynamics. Consider Fig. 5.2 and the corresponding diabatic PESs:

$$V_0(x) = a\left(x^4 - bx^2\right), \tag{5.19a}$$

$$V_1(x) = \frac{1}{2}m\omega^2(x-g)^2 + E_d. \tag{5.19b}$$

[12] One word of caution. In Eqs. (5.16) and (5.18), we twice approximate $f(E(x))(1-f(E(x)))$ as a delta function; this approximation cannot be exact given that $U(x)$ in Eq. (5.6) will not be smooth in the limit of large reorganization energies. Different manipulations can lead to slightly different prefactors, e.g. up to a factor of 2.

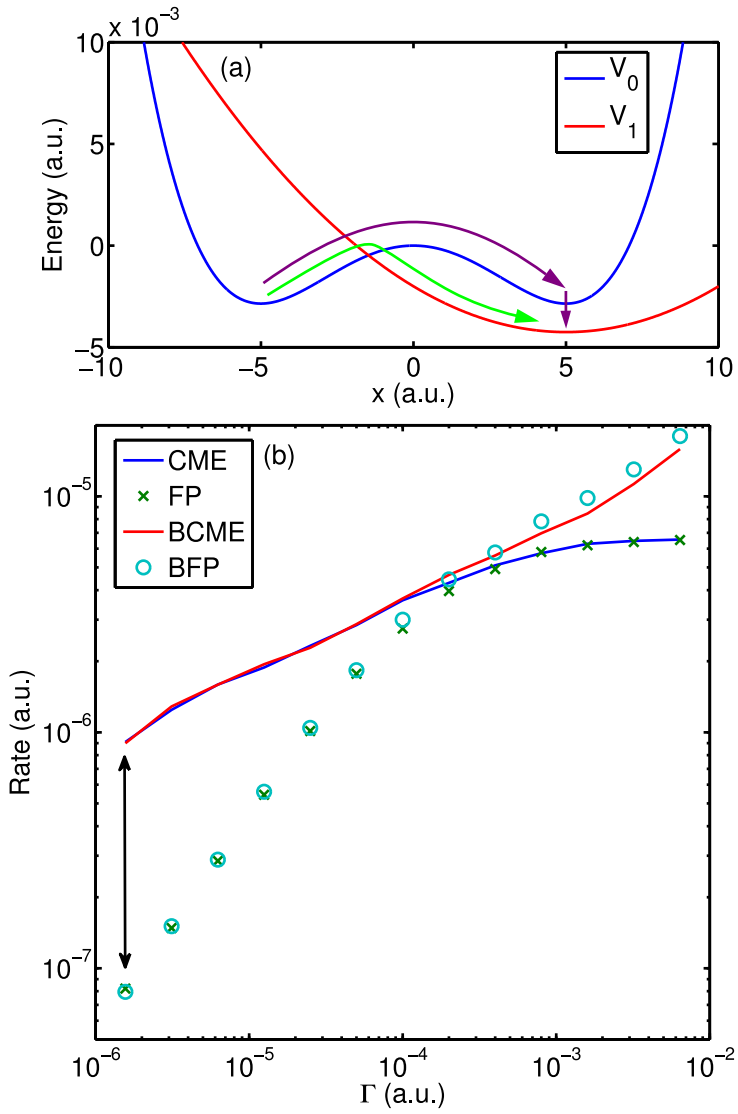

Figure 5.2: (a) Anharmonic, diabatic PESs defined in Eq. (5.19). (b) The rates of reaction as a function of Γ. The parameters for the PES are (all in atomic units): $m = 2000$, $a = 4.56 \times 10^{-6}$, $b = 50$, $\omega = 0.0003$, $g = 5$, $E_d = -0.00425$ and nuclear friction $\gamma_n = 2.7$. The temperature is $300K$ (so $k_bT = 9.5 \times 10^{-4} a.u.$). The unbroadened barrier height for the two paths denoted by green and purple arrows are 0.002375 $a.u.$ and 0.00285 $a.u.$, respectively. The CME must be valid for small Γ and BFP must be valid for large Γ. Note that surface-hopping based algorithms (CME and BCME) capture ground state dynamics (green arrow in (a)) and excited state dynamics (purple arrows), whereas mean-field based algorithms (FP and BFP) capture only the former. This leads to large differences for small Γ, as highlighted with the black arrow in (b).

Initially, we imagine the particle is equilibrated in the left basin of V_0 and we fit the average position of the nucleus to get the rate constant. Now, unlike Fig. 5.1, the FP and CME rate constants are very different for small Γ (as highlighted with the arrow in Fig. 5.2(b)). This discrepancy comes from the fact that, according to the mean-field based algorithms (FP and BFP), there is only one channel for the barrier crossing (the green arrow in Fig. 5.2(a)). However, according to the surface-hopping algorithms (CME and BCME), there are two channels through which the particle can escape the basin on the left: either a direct hop from V_0 to V_1 at the crossing point (the green arrow) or motion over the barrier on V_0 followed by subsequent relaxation on V_0 and later on a hop down to V_1 (the purple arrows). Thus, it is not simply slow motion or a large barrier per se that justifies EF dynamics; in general, an electronic friction model will fail whenever excited state dynamics are important.

5.4 Conclusions

To conclude, we have calculated the rates of activated barrier crossings with SH, FP, BFP, and BCME dynamics for the AH model. Let us summarize our findings:

- As one should have expected from perturbation theory, SH dynamics work well (only) when Γ is small.
- More interestingly, if we merely broaden the diabatic PESs, our resulting BCME dynamics capture the correct rates in both the small and large Γ limits. In fact, because of the algorithm's simplicity, we hypothesize that BCME trajectories should be trustworthy more generally.
- Perhaps most surprisingly, we have shown that BFP dynamics are also meaningful both in the large and small Γ limits, assuming parabolic diabats and large barriers. Indeed, Eqs. (5.16)-(5.18) above prove that, for electronic transitions

with large nuclear barriers and only one possible escape channel, Marcus theory is effectively consistent with Kramer's theory in the limit of small Γ (and large, overdamped electronic friction). This finding contradicts our intuition that EF dynamics should be correct only when $\Gamma > \omega$[46] and raises the question of what are the exact conditions necessary for EF dynamics to be valid?[13]

Fig. 5.2 is arguably the most important figure in this article. The figure reminds us that, if there are any excited state dynamics at all, electronic friction must fail. And in practice, it may well be very hard to rule out such dynamical processes, especially in multidimensional problems. These findings should be useful in the context of electrochemistry and surface physics, where there is a continuous transition from outer to inner sphere ET, and inexpensive dynamical models are sorely needed.

5.5 Acknowledgments

JES thanks Misha Galperin for very helpful discussions. This material is based upon work supported by the (U.S.) Air Force Office of Scientific Research (USAFOSR) PECASE award under AFOSR Grant No. FA9950-13-1-0157. J.E.S. acknowledges a Camille and Henry Dreyfus Teacher Scholar Award and a David and Lucille Packard Fellowship.

[13]Note that, in Fig. 5.1, $\gamma_n = 2m\omega$ so that ω is the correct relaxation time for the damped harmonic oscillator.

CHAPTER 6

Conclusions

We have explored different variants of surface hopping algorithms, from the well established fewest-switches surface hopping (FSSH) algorithm to its improved variant augmented-FSSH (A-FSSH), and from the surface-hopping/classical master equation (SH/CME) that is specialized to handle weak coupling between a metal surface and a nearby molecule to the broadened CME (BCME) that is capable of handling strong coupling as well.

In chapter 2 we investigated the decoherence issue in FSSH from the novel angle of entropy. By looking at the phase space representation of the trajectories, we were able to identify the erroneous coherence produced by FSSH and justify the coherence damping in A-FSSH as a reasonable improvement upon FSSH. Using a frozen Gaussian dynamics analysis, we established that FSSH trajectories cannot capture nonlocal coherences. This study also gave us a clearer picture as to why A-FSSH can yield reasonably accurate results: without recoherences, the coherence can either be approximated (when wavepackets are close together) or simply eliminated (when wavepackets are far apart).

In chapter 3 we further enhanced FSSH by incorporating the surface-leaking algorithm that was designed to tackle the incoherent relaxation into electronic bath. We investigated a model problem with an electronic bath in the wide band limit, and the surface-leaking FSSH (SL-FSSH) algorithm handled the competition between coherent nonadiabatic transition and incoherent electronic relaxation very well. In the narrow band limit, SL-FSSH successfully converged to a donor-accepter system without an electronic bath. However, the transition between the wide band limit and the

narrow band limit still requires further research to capture the incoherent electronic relaxation beyond the wide band limit.

In chapter 4, we turned our attention to metal surface and applied the SH/CME (i.e. an incoherent surface hopping scheme) to a simple electrochemical setting to investigate the nonequilibrium phenomena in an ionic conducting solution. We explored the breakdown of linear response theory and studied the origin of nonequilibrium effects by looking at the differences between nonequilibrium and equilibrium simulations. We further proposed a kinetic model to isolate the contributions from mass transport and electron transfer. With the help of the kinetic model, we were able to converge our linear response results to the nonequilibrium simulation results, identifying the deficiencies of linear response theory.

In chapter 5, we benchmarked two classes of MQC algorithms that were designed to deal with coupling with metal surface, namely electronic friction (EF) and SH/CME. We found a very surprising result,namely that EF performed well even in the nonadiabatic limit and we uncovered a connection between the Kramer's theory in overdamped limit and the Marcus's theory. When going beyond a harmonic potential, we finally showed that EF breaks down if we can identify multiple channels for barrier crossing. The failure of EF reminds us of the importance of excited dynamics that is captured by SH. That being said, we found that the BCME performed very well in all scenarios investigated thus far scenarios.

Looking forward, it will be very interesting to employ the BCME to a more realistic condensed phase system. When working in a larger system, the computational complexity for calculating surface hopping probabilities can be demanding. More research can be done to improve the efficiency of simulating larger systems. For instance, if one moves on one PES (V_a), one would want to reduce the frequency that the other PES (V_b) must be calculated because the force calculation is usually

the bottleneck of large system simulation. Another key direction will be to model chemical reactions at a electrode surface. The interplay between chemical reactions and electron transfer can inspire novel insights into the interfacial phenomena in the electrochemistry. Finally, there are many questions regarding electrochemistry that cannot be answered without an atomistic understanding of the dynamics involved.

APPENDIX A

1D Exact Quantum Scattering Calculation

This chapter is adapted from The Journal of Chemical Physics, Volume 142, Issue 8, Page 084109, 2015.

Let us now describe how we have calculated exact quantum scattering results with ~ 1000 electronic states[39]. Our notation will be as follows. For indices of electronic states, α is an index for reflecting states, β is an index for transmitting states and ε is an index for either. For quantity labeling, a superscript of (r) refers to reflections related quantities and (t) for transmission, superscript of $(left)$ and $(right)$ are for quantities evaluated on the left and right sides of the region of interest respectively, a subscript of inc refers to quantities attached to the incoming electronic state. For physical quantities, $\mathbf{H}$ denotes the Hamiltonian, $|\phi\rangle$ is diabatic electronic state, k is a wave number, and V is the potential energy.

Exact quantum results are calculated by solving equation:

$$(\mathbf{H} - E_0)\,|\psi(x)\rangle = 0 \tag{A.1}$$

where $\mathbf{H}$ is the Hamiltonian, E_0 is initial total energy and $|\psi(x)\rangle$ is the wave function defined in three regions. Region I is on the left of region of interest, Region II is the region of interest and Region III is on the right of region of interest. (The region of

interest is where all coupling occurs.) The wave function can be written as:

$$|\psi(x)\rangle = \begin{cases} e^{ik_{inc}x}\,|\phi_{inc}\rangle + \sum_\alpha r_\alpha e^{-ik_\alpha^{(r)}x}\,|\phi_\alpha\rangle & \text{Region I,} \\ \sum_\varepsilon c_\varepsilon(x)\,|\phi_\varepsilon\rangle & \text{Region II,} \\ \sum_\beta t_\beta e^{ik_\beta^{(t)}x}\,|\phi_\beta\rangle & \text{Region III.} \end{cases} \tag{A.2}$$

The wave numbers are defined as:

$$k_{inc} = \sqrt{2M(E_0 - V_{inc}^{(left)})}/\hbar \tag{A.3}$$

$$k_\alpha^{(r)} = \sqrt{2M(E_0 - V_\alpha^{(left)})}/\hbar \tag{A.4}$$

$$k_\beta^{(t)} = \sqrt{2M(E_0 - V_\beta^{(right)})}/\hbar \tag{A.5}$$

where M is the nuclear mass. r_ε and t_ε are reflection and transmission amplitudes respectively on state ε, and $c_\varepsilon(x)$ are amplitudes for the wave function in the interior region of interest (region II). The sum over α (β) includes all electronic states such that the $k_\alpha^{(r)}$ ($k_\beta^{(t)}$) are real, i.e. those electronic states that are energetically accessible.

Clearly, the wave function $|\psi(x)\rangle$ has four parts: (1) an asymptotically incoming wave, (2) an asymptotically reflecting wave, (3) an asymptotically transmitting wave, (4) an interior wave function. The first three components are localized plane waves. For a fixed incoming wave, the challenge is to compute the other 3 unknown variables by solving Eq. (A.1).

We solve Eq. (A.1) using a grid in position space with the kinetic operator in Hamiltonian expressed by a 5-stencil finite difference matrix. Eq. (A.1) is then rearranged into the form:

$$(\mathbf{H} - E_0)(|\psi(x)\rangle - |\psi_{inc}(x)\rangle) = -(\mathbf{H} - E_0)\,|\psi_{inc}(x)\rangle \tag{A.6}$$

where $|\psi_{inc}(x)\rangle$ is the known incoming wave and $|\psi(x)\rangle - |\psi_{inc}(x)\rangle$ is the unknown vector that must be solved.

We use a two-dimensional basis for the Hamiltonian, $|\varepsilon, x\rangle = |\phi_\varepsilon\rangle \otimes |x\rangle$. Here ε labels each diabatic electronic state, $\varepsilon = 1, 2, \ldots, N_\varepsilon$ where N_ε is the total number of electronic states. We set x as the index for a grid in position space, $x = -2, -1, \ldots, N_x + 2, N_x + 3$ where N_x is the total number of grid point in the region of interest. The bra space of the Hamiltonian is defined as:

$$\begin{aligned}\Big\{ &\langle 1,1| \,, \langle 1,2| \,, \ldots, \langle 1,N_x| \,, \langle 2,1| \,, \langle 2,2| \,, \ldots, \langle N_\varepsilon, N_x| \,, \\ &\langle 1,0| \,, \langle 2,0| \,, \ldots, \langle N_\alpha, 0| \,, \langle 1, N_x+1| \,, \langle 2, N_x+1| \,, \ldots \\ &, \langle N_\beta, N_x+1| \Big\}\end{aligned} \tag{A.7}$$

The ket space of the Hamiltonian is defined as:

$$\begin{aligned}\Big\{ &|1,1\rangle \,, |1,2\rangle \,, \ldots, |1,N_x\rangle \,, |2,1\rangle \,, |2,2\rangle \,, \ldots, |N_\varepsilon, N_x\rangle \,, \\ &|r_1\rangle \,, |r_2\rangle \,, \ldots, |r_{N_\alpha}\rangle \,, |t_1\rangle \,, |t_2\rangle \,, \ldots, \left|t_{N_\beta}\right\rangle \Big\}\end{aligned} \tag{A.8}$$

Here N_α and N_β are the total number of states that are energetically allowed for reflection and transmission, respectively. $|r_\varepsilon\rangle$ is a basis function for a reflecting state defined as:

$$|r_\varepsilon\rangle \equiv e^{2ik_\varepsilon^{(r)}\Delta x} |\varepsilon, -2\rangle + e^{ik_\varepsilon^{(r)}\Delta x} |\varepsilon, -1\rangle + |\varepsilon, 0\rangle \tag{A.9}$$

where Δx is the bin size of position grid. Similarly, $|t_\varepsilon\rangle$ is a basis function for a transmitting state defined as:

$$|t_\varepsilon\rangle \equiv |\varepsilon, N_x + 1\rangle + e^{ik_\varepsilon^{(t)}\Delta x} |\varepsilon, N_x + 2\rangle + e^{2ik_\varepsilon^{(t)}\Delta x} |\varepsilon, N_x + 3\rangle \tag{A.10}$$

Note that the bra and ket spaces are the same for the first $N_\varepsilon N_x$ dimensions but different for the last $N_\alpha + N_\beta$ dimensions. While the ket basis contains transmitting and reflecting wave, the bra basis contains the grid points$\langle 0|$ and $\langle N_x + 1|$ to encode the boundary.

In the basis above, the Hamiltonian is not symmetric and can be broken down by region as:

$$\mathbf{H} = \begin{pmatrix} \mathbf{H}_{II,II} & \mathbf{H}_{II,I} & \mathbf{H}_{II,III} \\ \mathbf{H}_{I,II} & \mathbf{H}_{I,I} & 0 \\ \mathbf{H}_{III,II} & 0 & \mathbf{H}_{III,III} \end{pmatrix} \tag{A.11}$$

$\mathbf{H}_{II,II}$ is the Hamiltonian for the region of interest while other blocks involve the boundary. $\mathbf{H}_{II,II}$ has dimensionality of $N_\varepsilon N_x \times N_\varepsilon N_x$ and the ket space is the same as bra space. The matrix elements of $\mathbf{H}_{II,II}$ are defined as:

$$\begin{aligned} \langle \varepsilon_1, x_1 | \mathbf{H}_{II,II} | \varepsilon_2, x_2 \rangle &= C \left[\left(\frac{5}{2} + \frac{V_{\varepsilon_1}(x_1)}{C} \right) \delta_{x_1,x_2} - \frac{4}{3}\delta_{x_1,x_2\pm 1} + \frac{1}{12}\delta_{x_1,x_2\pm 2} \right] \delta_{\varepsilon_1,\varepsilon_2} \\ &\quad + U_{\varepsilon_1,\varepsilon_2}(x_1)\delta_{x_1,x_2} \end{aligned} \tag{A.12}$$

Here δ is the Kronecker delta, $U_{\varepsilon_1,\varepsilon_2}$ is the electronic coupling between state ε_1 and ε_2, and the constant factor $C = \hbar^2/(2M\Delta x^2)$ where M is the nuclear mass. $\mathbf{H}_{I,I}$, $\mathbf{H}_{II,I}$ and $\mathbf{H}_{I,II}$ are the matrix elements at the boundary for the reflecting wave, and have dimensionality of $N_\alpha \times N_\alpha$, $N_\varepsilon N_x \times N_\alpha$ and $N_\alpha \times N_\varepsilon N_x$, respectively. $\mathbf{H}_{I,I}$ is defined as:

$$\langle \varepsilon, 0 | \mathbf{H}_{I,I} | r_\alpha \rangle = C \left(\frac{1}{12} e^{2ik_\varepsilon^{(r)}\Delta x} - \frac{4}{3} e^{ik_\varepsilon^{(r)}\Delta x} + \frac{5}{2} + \frac{V_\varepsilon(0)}{C} \right) \delta_{\varepsilon,\alpha} \tag{A.13}$$

$\mathbf{H}_{II,I}$ is defined as:

$$\langle \varepsilon, x | \mathbf{H}_{II,I} | r_\alpha \rangle = C \left[\left(\frac{1}{12} e^{ik_\varepsilon^{(r)} \Delta x} - \frac{4}{3} \right) \delta_{x,1} + \frac{1}{12} \delta_{x,2} \right] \delta_{\varepsilon,\alpha} \tag{A.14}$$

$\mathbf{H}_{I,II}$ is defined as:

$$\langle \varepsilon_1, 0 | \mathbf{H}_{I,II} | \varepsilon_2, x \rangle = C \left(-\frac{4}{3} \delta_{x,1} + \frac{1}{12} \delta_{x,2} \right) \delta_{\varepsilon_1,\varepsilon_2} \tag{A.15}$$

$\mathbf{H}_{III,III}$, $\mathbf{H}_{II,III}$ and $\mathbf{H}_{III,II}$ are the matrix elements at the boundary for the transmitting wave, and have dimensionality of $N_\beta \times N_\beta$, $N_\varepsilon N_x \times N_\beta$ and $N_\beta \times N_\varepsilon N_x$, respectively. $\mathbf{H}_{III,III}$ is defined as:

$$\langle \varepsilon, N_x + 1 | \mathbf{H}_{III,III} | t_\beta \rangle = C \left(\frac{1}{12} e^{2ik_\varepsilon^{(t)} \Delta x} - \frac{4}{3} e^{ik_\varepsilon^{(t)} \Delta x} + \frac{5}{2} + \frac{V_\varepsilon (N_x + 1)}{C} \right] \delta_{\varepsilon,\beta} \tag{A.16}$$

$\mathbf{H}_{II,III}$ is defined as:

$$\langle \varepsilon, x | \mathbf{H}_{II,III} | t_\beta \rangle = C \left[\left(\frac{1}{12} e^{ik_\varepsilon^{(t)} \Delta x} - \frac{4}{3} \right) \delta_{x,N_x} + \frac{1}{12} \delta_{x,N_x - 1} \right] \delta_{\varepsilon,\beta} \tag{A.17}$$

$\mathbf{H}_{III,II}$ is defined as:

$$\langle \varepsilon_1, N_x + 1 | \mathbf{H}_{III,II} | \varepsilon_2, x \rangle = C \left(-\frac{4}{3} \delta_{x,N_x} + \frac{1}{12} \delta_{x,N_x - 1} \right) \delta_{\varepsilon_1,\varepsilon_2} \tag{A.18}$$

The incoming wave function is chosen as:

$$|\psi_{inc}(x)\rangle = e^{-2ik_{inc}\Delta x} |inc, -2\rangle + e^{-ik_{inc}\Delta x} |inc, -1\rangle + |inc, 0\rangle \tag{A.19}$$

The elements of $(E_0 - \mathbf{H})\,|\psi_{inc}(x)\rangle$ are evaluated as:

$$\begin{aligned}\langle \varepsilon, x|\,(E_0 - \mathbf{H})\,|\psi_{inc}(x)\rangle \;\; &= \;\; C\left[\left(-\frac{5}{2} + \frac{4}{3}e^{-ik_{inc}\Delta x} - \frac{1}{12}e^{-2ik_{inc}\Delta x} + \frac{E_0 - V_{inc}}{C}\right)\delta_{x,0}\right. \\ &\left. + \left(\frac{4}{3} - \frac{1}{12}e^{-ik_{inc}\Delta x}\right)\delta_{x,1} - \frac{1}{12}\delta_{x,2}\right]\delta_{\varepsilon,inc} \qquad \text{(A.20)}\end{aligned}$$

This completes our description of how the Hamiltonian is constructed. In practice, Eq. (A.6) is solved numerically by using Intel MKL PARDISO solver[200] which is a parallel direct sparse solver. Taking advantage of the large sparsity of the Hamiltonian, the sparse solver minimizes the memory needed to storing the matrix as well as the CPU time for solving Eq. (A.6). As such, the sparse solver makes it possible to include thousands of electronic states in the bath and grid points in position space and solve Eq. (A.6) in a reasonable time. For instance, the calculation associated with results in Fig. 3.13 has 501 discretized electronic states in the bath combined with 6000 grid points in region II ($[-30, 30]$ $a.u.$), and the CPU time is less than 4 minutes (the real time is 1 minute by running in parallel with 4 cores).

Reflection probabilities are then found by renormalizing the amplitudes of every channel n according to:

$$\left|r_n^{(norm)}\right|^2 = \frac{k_n^{(r)}}{k_{inc}}\,|r_n|^2 \qquad \text{(A.21)}$$

Transmission amplitudes are renormalized analogously.

REFERENCE AND NOTES

(1) Meyer, H.-D.; Miller, W. H. *J. Chem. Phys.* **1979**, *70*, 3214–3223.

(2) Meyer, H.-D.; Miller, W. H. *J. Chem. Phys.* **1980**, *72*, 2272–2281.

(3) Stock, G.; Thoss, M. *Phys. Rev. Lett.* **1997**, *78*, 578–581.

(4) Miller, W. H. *J. Phys. Chem. A* **2009**, *113*, 1405–1415.

(5) Kim, H.; Nassimi, A.; Kapral, R. *J. Chem. Phys.* **2008**, *129*, 084102.

(6) Nassimi, A.; Bonella, S.; Kapral, R. *J. Chem. Phys.* **2010**, *133*, 134115.

(7) Kelly, A.; van Zon, R.; Schofield, J.; Kapral, R. *J. Chem. Phys.* **2012**, *136*, 084101.

(8) Rekik, N.; Hsieh, C.-Y.; Freedman, H.; Hanna, G. *J. Chem. Phys.* **2013**, *138*, 144106.

(9) Kim, H. W.; Rhee, Y. M. *J. Chem. Phys.* **2014**, *140*, 184106.

(10) Martínez, T. J.; Ben-Nun, M.; Levine, R. D. *J. Phys. Chem.* **1996**, *100*, 7884–7895.

(11) Ben-Nun, M.; Martínez, T. J. *J. Chem. Phys.* **2000**, *112*, 6113.

(12) Yang, S.; Coe, J. D.; Kaduk, B.; Martínez, T. J. *J. Chem. Phys.* **2009**, *130*, 134113.

(13) Tully, J. C. *J. Chem. Phys.* **1990**, *93*, 1061.

(14) Herman, M. F. *J. Chem. Phys.* **1982**, *76*, 2949–2958.

(15) Herman, M. F. *J. Chem. Phys.* **1983**, *79*, 2771–2778.

(16) Herman, M. F.; Kluk, E. *Chem. Phys.* **1984**, *91*, 27–34.

(17) Herman, M. F. *J. Chem. Phys.* **1984**, *81*, 754–763.

(18) Herman, M. F. *J. Chem. Phys.* **1984**, *81*, 764–774.

(19) Herman, M. F. *J. Chem. Phys.* **1987**, *87*, 4779–4793.

(20) Subotnik, J. E.; Ouyang, W.; Landry, B. R. *J. Chem. Phys.* **2013**, *139*, 214107.

(21) Engel, G. S.; Calhoun, T. R.; Read, E. L.; Ahn, T.-K.; Mančal, T.; Cheng, Y.-C.; Blankenship, R. E.; Fleming, G. R. *Nature* **2007**, *446*, 782–6.

(22) Collini, E.; Scholes, G. D. *Science* **2009**, *323*, 369–73.

(23) Webster, F.; Rossky, P.; Friesner, R. *Comput. Phys. Commun.* **1991**, *63*, 494–522.

(24) Webster, F.; Wang, E. T.; Rossky, P. J.; Friesner, R. A. *J. Chem. Phys.* **1994**, *100*, 4835.

(25) Schwartz, B. J.; Bittner, E. R.; Prezhdo, O. V.; Rossky, P. J. *J. Chem. Phys.* **1996**, *104*, 5942.

(26) Prezhdo, O. V.; Rossky, P. J. *J. Chem. Phys.* **1997**, *107*, 825.

(27) Fang, J.-Y.; Hammes-Schiffer, S. *J. Chem. Phys.* **1999**, *110*, 11166.

(28) Fang, J.-Y.; Hammes-Schiffer, S. *J. Phys. Chem. A* **1999**, *103*, 9399–9407.

(29) Volobuev, Y. L.; Hack, M. D.; Topaler, M. S.; Truhlar, D. G. *J. Chem. Phys.* **2000**, *112*, 9716.

(30) Hack, M. D.; Truhlar, D. G. *J. Chem. Phys.* **2001**, *114*, 2894.

(31) Jasper, A. W.; Hack, M. D.; Truhlar, D. G. *J. Chem. Phys.* **2001**, *115*, 1804.

(32) Wong, K. F.; Rossky, P. J. *J. Chem. Phys.* **2002**, *116*, 8418.

(33) Wong, K. F.; Rossky, P. J. *J. Chem. Phys.* **2002**, *116*, 8429.

(34) Zhu, C.; Nangia, S.; Jasper, A. W.; Truhlar, D. G. *J. Chem. Phys.* **2004**, *121*, 7658–70.

(35) Zhu, C.; Jasper, A. W.; Truhlar, D. G. *J. Chem. Phys.* **2004**, *120*, 5543–57.

(36) Jasper, A. W.; Truhlar, D. G. *J. Chem. Phys.* **2005**, *123*, 64103.

(37) Shenvi, N.; Subotnik, J. E.; Yang, W. *J. Chem. Phys.* **2011**, *134*, 144102.

(38) Jaeger, H. M.; Fischer, S.; Prezhdo, O. V. *J. Chem. Phys.* **2012**, *137*, 22A545.

(39) Subotnik, J. E.; Shenvi, N. *J. Chem. Phys.* **2011**, *134*, 024105.

(40) Landry, B. R.; Subotnik, J. E. *J. Chem. Phys.* **2012**, *137*, 22A513.

(41) Preston, R. K. *J. Chem. Phys.* **1976**, *65*, 1589.

(42) Dou, W.; Nitzan, A.; Subotnik, J. E. *J. Chem. Phys.* **2015**, *142*, 084110.

(43) Shenvi, N.; Schmidt, J.; Edwards, S.; Tully, J. *Phys. Rev. A* **2008**, *78*, 022502.

(44) Shenvi, N.; Roy, S.; Tully, J. C. *J. Chem. Phys.* **2009**, *130*, 174107.

(45) Shenvi, N.; Roy, S.; Tully, J. C. *Science* **2009**, *326*, 829–832.

(46) Dou, W.; Nitzan, A.; Subotnik, J. E. *J. Chem. Phys.* **2015**, *143*, 054103.

(47) Dou, W.; Nitzan, A.; Subotnik, J. E. *J. Chem. Phys.* **2015**, *142*, 084110.

(48) Galperin, M.; Ratner, M. A.; Nitzan, A. *J. Chem. Phys.* **2004**, *121*, 11965.

(49) Galperin, M.; Ratner, M. A.; Nitzan, A. *J. Phys. Condens. Matter* **2007**, *19*, 103201.

(50) Mii, T.; Tikhodeev, S. G.; Ueba, H. *Phys. Rev. B* **2003**, *68*, 205406.

(51) White, A. J.; Galperin, M. *Phys. Chem. Chem. Phys.* **2012**, *14*, 13809.

(52) Thoss, M.; Kondov, I.; Wang, H. *Chem. Phys.* **2004**, *304*, 169–181.

(53) Kondov, I.; Thoss, M.; Wang, H. *J. Phys. Chem. A* **2006**, *110*, 1364–1374.

(54) Thoss, M.; Kondov, I.; Wang, H. *Phys. Rev. B* **2007**, *76*, 153313.

(55) Li, J.; Kondov, I.; Wang, H.; Thoss, M. *J. Phys. Condens. Matter* **2015**, *27*, 134202.

(56) Chen, J.; Su, J.; Wang, W.; Reed, M. *Phys. E Low-dimensional Syst. Nanostructures* **2003**, *16*, 17–23.

(57) Schull, T. L.; Kushmerick, J. G.; Patterson, C. H.; George, C.; Moore, M. H.; Pollack, S. K.; Shashidhar, R. *J. Am. Chem. Soc.* **2003**, *125*, 3202–3203.

(58) Li, C.; Zhang, D.; Liu, X.; Han, S.; Tang, T.; Zhou, C.; Fan, W.; Koehne, J.; Han, J.; Meyyappan, M.; Rawlett, A. M.; Price, D. W.; Tour, J. M. *Appl. Phys. Lett.* **2003**, *82*, 645.

(59) Galperin, M.; Ratner, M. A.; Nitzan, A. *Nano Lett.* **2005**, *5*, 125–130.

(60) Dou, W.; Subotnik, J. E. *J. Chem. Phys.* **2016**, *144*, 024116.

(61) Dou, W.; Subotnik, J. E. *J. Chem. Phys.* **2017**, *146*, 092304.

(62) McQuarrie, D. A. *Statistical Mechanics*, 1st ed.; University Science Books, 2000.

(63) Tolman, R. C. *The Principles of Statistical Mechanics*, new edition ed.; Dover Publications, 2010.

(64) Barbatti, M.; Lan, Z.; Crespo-Otero, R.; Szymczak, J. J.; Lischka, H.; Thiel, W. *J. Chem. Phys.* **2012**, *137*, 22A503.

(65) Ruf, H. et al. *J. Chem. Phys.* **2012**, *137*, 224303.

(66) Wang, L.; Beljonne, D. *J. Chem. Phys.* **2013**, *139*, 064316.

(67) Madjet, M. E.-A.; Li, Z.; Vendrell, O. *J. Chem. Phys.* **2013**, *138*, 094311.

(68) Mai, S.; Marquetand, P.; Richter, M.; González-Vázquez, J.; González, L. *Chemphyschem* **2013**, *14*, 2920–31.

(69) Akimov, A. V.; Prezhdo, O. V. *J. Chem. Theory Comput.* **2013**, *9*, 4959–4972.

(70) Nelson, T.; Fernandez-Alberti, S.; Roitberg, A. E.; Tretiak, S. *J. Chem. Phys.* **2013**, *138*, 224111.

(71) Parandekar, P. V.; Tully, J. C. *J. Chem. Phys.* **2005**, *122*, 094102.

(72) Schmidt, J. R.; Parandekar, P. V.; Tully, J. C. *J. Chem. Phys.* **2008**, *129*, 044104.

(73) Landry, B. R.; Falk, M. J.; Subotnik, J. E. *J. Chem. Phys.* **2013**, *139*, 211101.

(74) Balescu, R.; Zhang, W. Y. *J. Plasma Phys.* **1988**, *40*, 215.

(75) Boucher, W.; Traschen, J. *Phys. Rev. D* **1988**, *37*, 3522–3532.

(76) Zhang, W. Y.; Balescu, R. *J. Plasma Phys.* **1988**, *40*, 199.

(77) Anderson, A. *Phys. Rev. Lett.* **1995**, *74*, 621–625.

(78) Martens, C. C.; Fang, J.-Y. *J. Chem. Phys.* **1997**, *106*, 4918.

(79) Prezhdo, O.; Kisil, V. *Phys. Rev. A* **1997**, *56*, 162–175.

(80) Donoso, A.; Martens, C. C. *J. Phys. Chem. A* **1998**, *102*, 4291–4300.

(81) Kapral, R.; Ciccotti, G. *J. Chem. Phys.* **1999**, *110*, 8919.

(82) Nielsen, S.; Kapral, R.; Ciccotti, G. *J. Chem. Phys.* **2000**, *112*, 6543.

(83) Micha, D. A.; Thorndyke, B. *Int. J. Quantum Chem.* **2002**, *90*, 759–771.

(84) Mukamel, S. *J. Chem. Phys.* **1982**, *77*, 173.

(85) Wehrle, M.; Šulc, M.; Vaníček, J. *Chim. Int. J. Chem.* **2011**, *65*, 334–338.

(86) Zambrano, E.; Ozorio de Almeida, A. M. *Phys. Rev. E* **2011**, *84*, 045201.

(87) Šulc, M.; Hernández, H.; Martínez, T. J.; Vaníček, J. *J. Chem. Phys.* **2013**, *139*, 034112.

(88) Włodarz, J. *Int. J. Theor. Phys.* **2003**, *42*, 1075–1084.

(89) SHANNON, C. E. *BELL Syst. Tech. J.* **1948**, *27*, 379–423.

(90) Sadeghi, P.; Khademi, S.; Darooneh, A. H. *Phys. Rev. A* **2012**, *86*, 012119.

(91) Manfredi, G.; Feix, M. *Phys. Rev. E* **2000**, *62*, 4665–4674.

(92) Bedard-Hearn, M. J.; Larsen, R. E.; Schwartz, B. J. *J. Chem. Phys.* **2005**, *123*, 234106.

(93) Larsen, R. E.; Bedard-Hearn, M. J.; Schwartz, B. J. *J. Phys. Chem. B* **2006**, *110*, 20055–66.

(94) Subotnik, J. E.; Shenvi, N. *J. Chem. Phys.* **2011**, *134*, 244114.

(95) Landry, B. R.; Subotnik, J. E. *J. Chem. Phys.* **2011**, *135*, 191101.

(96) Ballentine, L. E. *Quantum Mechanics: A Modern Development*; Wspc, 1998.

(97) Hanna, G.; Kapral, R. *J. Chem. Phys.* **2005**, *122*, 244505.

(98) Kernan, D. M.; Ciccotti, G.; Kapral, R. *J. Phys. Chem. B* **2008**, *112*, 424–32.

(99) Huo, P.; Coker, D. F. *J. Chem. Phys.* **2011**, *135*, 201101.

(100) Miller, W. H. *J. Chem. Phys.* **1970**, *52*, 3563.

(101) Ogawa, T.; Ohno, K. *J. Phys. Chem. A* **1999**, *103*, 9925–9930.

(102) Ogawa, T.; Ohno, K. *J. Chem. Phys.* **1999**, *110*, 3773.

(103) Imura, K.; Kishimoto, N.; Ohno, K. *J. Phys. Chem. A* **2002**, *106*, 3759–3765.

(104) Falcinelli, S.; Candori, P.; Bettoni, M.; Pirani, F.; Vecchiocattivi, F. *J. Phys. Chem. A* **2014**, *118*, 6501–6.

(105) Cederbaum, L. S.; Zobeley, J.; Tarantelli, F. *Phys. Rev. Lett.* **1997**, *79*, 4778–4781.

(106) Marburger, S.; Kugeler, O.; Hergenhahn, U.; Möller, T. *Phys. Rev. Lett.* **2003**, *90*, 203401.

(107) Jahnke, T.; Czasch, A.; Schöffler, M.; Schössler, S.; Knapp, A.; Käsz, M.; Titze, J.; Wimmer, C.; Kreidi, K.; Grisenti, R.; Staudte, A.; Jagutzki, O.;

Hergenhahn, U.; Schmidt-Böcking, H.; Dörner, R. *Phys. Rev. Lett.* **2004**, *93*, 163401.

(108) Sisourat, N. *J. Chem. Phys.* **2013**, *139*, 074111.

(109) Miteva, T.; Chiang, Y.-C.; Kolorenč, P.; Kuleff, A. I.; Gokhberg, K.; Cederbaum, L. S. *J. Chem. Phys.* **2014**, *141*, 064307.

(110) Berry, R. S. *Radiat. Res.* **1974**, *59*, 367.

(111) Jailaubekov, A. E.; Willard, A. P.; Tritsch, J. R.; Chan, W.-L.; Sai, N.; Gearba, R.; Kaake, L. G.; Williams, K. J.; Leung, K.; Rossky, P. J.; Zhu, X.-Y. *Nat. Mater.* **2013**, *12*, 66–73.

(112) Albers, A.; Demeshko, S.; Dechert, S.; Saouma, C. T.; Mayer, J. M.; Meyer, F. *J. Am. Chem. Soc.* **2014**, *136*, 3946–54.

(113) Fischer, S. A.; Lingerfelt, D. B.; May, J. W.; Li, X. *Phys. Chem. Chem. Phys.* **2014**, *16*, 17507–14.

(114) Landry, B. R.; Subotnik, J. E. *J. Chem. Theory Comput.* **2014**, *10*, 4253–4263.

(115) Long, R.; Prezhdo, O. V. *J. Am. Chem. Soc.* **2014**, *136*, 4343–54.

(116) Nelson, T.; Fernandez-Alberti, S.; Roitberg, A. E.; Tretiak, S. *Acc. Chem. Res.* **2014**, *47*, 1155–64.

(117) Liu, J.; Neukirch, A. J.; Prezhdo, O. V. *J. Phys. Chem. C* **2014**, *118*, 20702–20709.

(118) Schwerdtfeger, C. A.; Soudackov, A. V.; Hammes-Schiffer, S. *J. Chem. Phys.* **2014**, *140*, 034113.

(119) Freed, J. H. *J. Chem. Phys.* **1968**, *49*, 376.

(120) Borovkov, V. I.; Beregovaya, I. V.; Shchegoleva, L. N.; Potashov, P. A.; Bagryansky, V. A.; Molin, Y. N. *J. Chem. Phys.* **2012**, *137*, 104305.

(121) De Almeida, N.; Goward, G. *J. Power Sources* **2014**, *268*, 853–860.

(122) Rantaharju, J.; Mareš, J.; Vaara, J. *J. Chem. Phys.* **2014**, *141*, 014109.

(123) Reufer, M.; Walter, M. J.; Lagoudakis, P. G.; Hummel, A. B.; Kolb, J. S.; Roskos, H. G.; Scherf, U.; Lupton, J. M. *Nat. Mater.* **2005**, *4*, 340–6.

(124) Cannizzo, A.; Blanco-Rodríguez, A. M.; El Nahhas, A.; Sebera, J.; Zális, S.; Vlcek, A.; Chergui, M. *J. Am. Chem. Soc.* **2008**, *130*, 8967–74.

(125) Losa, A. M.; Galvan, I. F.; Sanchez, M. L.; Martín, M. E.; Aguilar, M. A. *J. Phys. Chem. B* **2008**, *112*, 877–84.

(126) Sergentu, D.-C.; Maurice, R.; Havenith, R. W. A.; Broer, R.; Roca-Sanjuán, D. *Phys. Chem. Chem. Phys.* **2014**, *16*, 25393–403.

(127) Mai, S.; Marquetand, P.; González, L. *J. Chem. Phys.* **2014**, *140*, 204302.

(128) Tully, J. C.; Preston, R. K. *J. Chem. Phys.* **1971**, *55*, 562.

(129) Shenvi, N.; Subotnik, J. E.; Yang, W. *J. Chem. Phys.* **2011**, *135*, 024101.

(130) Nelson, T.; Fernandez-Alberti, S.; Chernyak, V.; Roitberg, A. E.; Tretiak, S. *J. Chem. Phys.* **2012**, *136*, 054108.

(131) Wang, L.; Prezhdo, O. V. *J. Phys. Chem. Lett.* **2014**, *5*, 713–719.

(132) Granucci, G.; Persico, M.; Toniolo, A. *J. Chem. Phys.* **2001**, *114*, 10608.

(133) Meek, G. A.; Levine, B. G. *J. Phys. Chem. Lett.* **2014**, *5*, 2351–2356.

(134) Fischer, S. A.; Chapman, C. T.; Li, X. *J. Chem. Phys.* **2011**, *135*, 144102.

(135) Nakanishi, H.; Bishop, K. J. M.; Kowalczyk, B.; Nitzan, A.; Weiss, E. A.; Tretiakov, K. V.; Apodaca, M. M.; Klajn, R.; Stoddart, J. F.; Grzybowski, B. A. *Nature* **2009**, *460*, 371–5.

(136) García Rey, N.; Arnolds, H. *J. Chem. Phys.* **2011**, *135*, 224708.

(137) Petek, H. *J. Chem. Phys.* **2012**, *137*, 091704.

(138) Shenvi, N.; Yang, W. *J. Chem. Phys.* **2012**, *137*, 22A528.

(139) Floß, G.; Granucci, G.; Saalfrank, P. *J. Chem. Phys.* **2012**, *137*, 234701.

(140) Bard, A. J. *Electrochemical methods: fundamentals and applications*, 2nd ed.; Wiley: New York, 2001.

(141) Willard, A. P.; Reed, S. K.; Madden, P. A.; Chandler, D. *Faraday Discuss.* **2009**, *141*, 423–441.

(142) Nitzan, A. *Chemical dynamics in condensed phases : relaxation, transfer and reactions in condensed molecular systems*, 1st ed.; Oxford University Press: New York, 2006; p 719.

(143) Elste, F.; Weick, G.; Timm, C.; von Oppen, F. *Appl. Phys. A Mater. Sci. Process.* **2008**, *93*, 345–354.

(144) Palla, P. L.; Pierleoni, C.; Ciccotti, G. *Phys. Rev. E* **2008**, *78*, 021204.

(145) Mugnai, M. L.; Caprara, S.; Ciccotti, G.; Pierleoni, C.; Mareschal, M. *J. Chem. Phys.* **2009**, *131*, 064106.

(146) Petersen, M. K.; Kumar, R.; White, H. S.; Voth, G. A. *J. Phys. Chem. C* **2012**, *116*, 4903–4912.

(147) Cao, Z.; Peng, Y.; Voth, G. A. *J. Phys. Chem. B* **2015**, *119*, 7516–7521.

(148) Griffiths, D. J. *Introduction to electrodynamics*, 2nd ed.; Prentice Hall: Englewood Cliffs, N.J., 1989; p 154.

(149) Yeh, I.-C.; Berkowitz, M. L. *J. Chem. Phys.* **1999**, *111*, 3155–3162.

(150) Arnold, A.; De Joannis, J.; Holm, C. *J. Chem. Phys.* **2002**, *117*, 2496–2502.

(151) De Joannis, J.; Arnold, A.; Holm, C. *J. Chem. Phys.* **2002**, *117*, 2503–2512.

(152) Ballenegger, V.; Arnold, A.; Cerdà, J. J. *J. Chem. Phys.* **2009**, *131*, 094107.

(153) Allen, M.; Tildesley, D. *Computer simulation of liquids*, 1st ed.; Oxford University Press: New York, 1987; p 385.

(154) Nosé, S. *J. Chem. Phys.* **1984**, *81*, 511–519.

(155) Swope, W. C.; Andersen, H. C.; Berens, P. H.; Wilson, K. R. *J. Chem. Phys.* **1982**, *76*, 637–649.

(156) Frenkel, D.; Smit, B. *Understanding molecular simulation : from algorithms to applications*, 2nd ed.; Academic Press: San Diego, 2001; p 664.

(157) Alder, B. J.; Wainwright, T. E. *Phys. Rev. A* **1970**, *1*, 18–21.

(158) Levesque, D.; Ashurst, W. T. *Phys. Rev. Lett.* **1974**, *33*, 277–280.

(159) Blondel, C.; Delsart, C.; Goldfarb, F. *J. Phys. B At. Mol. Opt. Phys.* **2001**, *34*, L281–L288.

(160) Cannes, C.; Cachet, H.; Debiemme-Chouvy, C.; Deslouis, C.; de Sanoit, J.; Le Naour, C.; Zinovyeva, V. a. *J. Phys. Chem. C* **2013**, *117*, 22915–22925.

(161) Sha, M.; Dou, Q.; Luo, F.; Zhu, G.; Wu, G. *ACS Appl. Mater. Interfaces* **2014**, *6*, 12556–12565.

(162) Cheng, J.; Sprik, M. *J. Phys. Condens. Matter* **2014**, *26*, 244108.

(163) Hughes, Z. E.; Walsh, T. R. *J. Colloid Interface Sci.* **2014**, *436*, 99–110.

(164) Sugimoto, Y.; Kitazumi, Y.; Tsujimura, S.; Shirai, O.; Yamamoto, M.; Kano, K. *Biosens. Bioelectron.* **2015**, *63*, 138–144.

(165) Jänsch, T.; Wallauer, J.; Roling, B. *J. Phys. Chem. C* **2015**, *119*, 4620–4626.

(166) Ma, K.; Forsman, J.; Woodward, C. E. *J. Chem. Phys.* **2015**, *142*, 174704.

(167) Gileadi, E. *Physical Electrochemistry*, 1st ed.; Wiley-VCH, 2011.

(168) Leggett, A. J.; Chakravarty, S.; Dorsey, A. T.; Fisher, M. P. A.; Garg, A.; Zwerger, W. *Rev. Mod. Phys.* **1987**, *59*, 1–85.

(169) Nitzan, A. *Annu. Rev. Phys. Chem.* **2001**, *52*, 681–750.

(170) Marcus, R. A. *J. Chem. Phys.* **1956**, *24*, 966.

(171) Zusman, L. *Chem. Phys.* **1980**, *49*, 295–304.

(172) Straub, J. E.; Berne, B. J. *J. Chem. Phys.* **1987**, *87*, 6111.

(173) Hänggi, P.; Talkner, P.; Borkovec, M. *Rev. Mod. Phys.* **1990**, *62*, 251–341.

(174) Mohr, J. H.; Schmickler, W. *Phys. Rev. Lett.* **2000**, *84*, 1051–4.

(175) Mohr, J.; Schmickler, W.; Badiali, J. *Chem. Phys.* **2006**, *324*, 140–147.

(176) Mishra, A. K.; Waldeck, D. H. *J. Phys. Chem. C* **2009**, *113*, 17904–17914.

(177) Mishra, A. K.; Waldeck, D. H. *J. Phys. Chem. C* **2011**, *115*, 20662–20673.

(178) Wilner, E. Y.; Wang, H.; Cohen, G.; Thoss, M.; Rabani, E. *Phys. Rev. B* **2013**, *88*, 045137.

(179) Wilner, E. Y.; Wang, H.; Thoss, M.; Rabani, E. *Phys. Rev. B* **2014**, *89*, 205129.

(180) Head-Gordon, M.; Tully, J. C. *J. Chem. Phys.* **1995**, *103*, 10137.

(181) Bode, N.; Kusminskiy, S. V.; Egger, R.; von Oppen, F. *Beilstein J. Nanotechnol.* **2012**, *3*, 144–162.

(182) Adelman, S. A. *J. Chem. Phys.* **1976**, *64*, 2375.

(183) Tully, J. C. *J. Chem. Phys.* **1980**, *73*, 1975.

(184) Head-Gordon, M.; Tully, J. C. *J. Chem. Phys.* **1992**, *96*, 3939.

(185) Brandbyge, M.; Hedegård, P.; Heinz, T. F.; Misewich, J. A.; Newns, D. M. *Phys. Rev. B* **1995**, *52*, 6042–6056.

(186) Mozyrsky, D.; Hastings, M. B.; Martin, I. *Phys. Rev. B* **2006**, *73*, 035104.

(187) Thomas, M.; Karzig, T.; Kusminskiy, S. V.; Zaránd, G.; von Oppen, F. *Phys. Rev. B* **2012**, *86*, 195419.

(188) Dou, W.; Nitzan, A.; Subotnik, J. E. *J. Chem. Phys.* **2015**, *142*, 234106.

(189) Galperin, M.; Nitzan, A. *J. Phys. Chem. Lett.* **2015**, *6*, 4898–4903.

(190) Schmickler, W.; Mohr, J. *J. Chem. Phys.* **2002**, *117*, 2867.

(191) Prezhdo, O. V.; Rossky, P. J. *J. Chem. Phys.* **1997**, *107*, 825.

(192) Hack, M. D.; Truhlar, D. G. *J. Chem. Phys.* **2001**, *114*, 9305.

(193) Hynes, J. T. *J. Phys. Chem.* **1986**, *90*, 3701–3706.

(194) Morillo, M.; Cukier, R. I. *J. Chem. Phys.* **1988**, *89*, 6736.

(195) Huo, P.; Miller, T. F.; Coker, D. F. *J. Chem. Phys.* **2013**, *139*, 151103.

(196) Jain, A.; Subotnik, J. E. *J. Chem. Phys.* **2015**, *143*, 134107.

(197) Morgan, J. D.; Wolynes, P. G. *J. Phys. Chem.* **1987**, *91*, 874–883.

(198) Ulstrup, J. *Charge transfer processes in condensed media*; Lecture notes in chemistry; Springer-Verlag, 1979; p 419.

(199) Levich, V. G. *Adv. Electrochem. Eng.* **1956**, *4*, 249.

(200) Schenk, O.; Gärtner, K. *Futur. Gener. Comput. Syst.* **2004**, *20*, 475–487.